

# **Polyoxometalates as Cathode Materials of Lithium Battery and Its Reaction Mechanism**

(ポリオキソメタレートを用いたリチウム電池特性とその反応  
機構)

By

Erfu Ni

January, 2014

Department of Materials Science and Engineering

Nagoya Institute of Technology

Japan



# Contents

<b>Chapter 1 Introduction.....</b>	<b>1</b>
1.1 An Overview of Rechargeable (Secondary) Batteries.....	1
1.1.1 Lead-acid Battery.....	1
1.1.2 Nickel-Cadmium (Ni-Cd) Battery.....	2
1.1.3 Nickel-Metal Hydride (Ni-MH) Battery.....	3
1.1.4 Lithium Batteries.....	3
1.2 Cathode Materials for Lithium Batteries.....	6
1.2.1 Materials with Layered Rock-Salt Structure.....	6
1.2.2 Material with Spinel Structure.....	12
1.2.3 Material with Olivine Structure.....	14
1.2.4 Organic Materials.....	15
1.2.5 Metal Complex and Cluster Ion Materials.....	17
1.2.6 Polyoxometalates (POMs) Materials.....	19
1.3 Purposes of this study.....	25
References.....	27
<b>Chapter 2 Synthesis and Electrochemical Properties of Polyoxovanadate <math>K_7[NiV_{13}O_{38}]</math>.....</b>	<b>37</b>
2.1 Introduction.....	37
2.2 Experimental.....	39
2.2.1 Synthesis of Materials.....	39
2.2.2 Characterization.....	40
2.2.3 Electrochemical Measurements.....	41
2.3 Results and Discussion.....	42
2.3.1 Crystal and Molecular Structures.....	42
2.3.2 Thermal Stability.....	43
2.3.3 Crystal Morphologies.....	44
2.3.4 Electrochemical Properties.....	45
2.3.5 Discharge-Charge Reaction Mechanism.....	56
2.4 Conclusions.....	59
References.....	60
<b>Chapter 3 Synthesis and Electrochemical Properties of Polyoxovanadate <math>K_7[MnV_{13}O_{38}]</math>.....</b>	<b>63</b>
3.1 Introduction.....	63
3.2 Experimental.....	64
3.2.1 Synthesis of Materials.....	64
3.2.2 Characterization.....	65
3.2.3 Electrochemical Measurements.....	65
3.3 Results and Discussion.....	66
3.3.1 Crystal and Molecular Structures.....	66
3.3.2 Crystal Morphology.....	68
3.3.3 Electrochemical properties.....	69
3.3.4 Discharge-Charge Reaction Mechanism.....	85
3.4 Conclusions.....	89
References.....	90

<b>Chapter 4 Synthesis and Electrochemical Properties of Polyoxomolybdate (NH<sub>4</sub>)<sub>6</sub>[NiMo<sub>9</sub>O<sub>32</sub>]</b>	<b>93</b>
4.1 Introduction .....	93
4.2 Experimental .....	94
4.2.1 Synthesis of Materials .....	94
4.2.2 Characterization .....	95
4.2.3 Electrochemical Measurements .....	96
4.3 Results and Discussion .....	97
4.3.1 Crystal and Molecular Structures .....	97
4.3.2 Thermal Stability .....	99
4.3.3 Crystal Morphology .....	100
4.3.4 Electrochemical Properties .....	102
4.3.5 Discharge-Charge Reaction Mechanism .....	111
4.4 Conclusions .....	112
References .....	114
<b>Chapter 5 Synthesis and Electrochemical Properties of Polyoxomolybdate (NH<sub>4</sub>)<sub>6</sub>[MnMo<sub>9</sub>O<sub>32</sub>]</b>	<b>115</b>
5.1 Introduction .....	115
5.2 Experimental .....	115
5.2.1 Synthesis of Materials .....	115
5.2.2 Electrochemical Measurements .....	116
5.3 Results and Discussion .....	117
5.3.1 Crystal and Molecular Structures .....	117
5.3.2 Thermal Stability .....	119
5.3.3 Crystal Morphology .....	119
5.3.4 Electrochemical Properties .....	120
5.4 Conclusions .....	123
<b>Chapter 6 Synthesis and Electrochemical Properties of Anderson Type Polyoxomolybdate Na<sub>3</sub>[AlMo<sub>6</sub>O<sub>24</sub>H<sub>6</sub>]</b>	<b>125</b>
6.1 Introduction .....	125
6.2 Experimental .....	126
6.2.1 Synthesis of Materials .....	126
6.2.2 Characterization .....	127
6.2.3 Electrochemical Measurements .....	128
6.3 Results and Discussion .....	129
6.3.1 Crystal and Molecular Structures .....	129
6.3.2 Crystal Morphology .....	132
6.3.3 Electrochemical Properties .....	133
6.4 Discharge-Charge Reaction Mechanism .....	142
6.5 Conclusions .....	146
References .....	148
<b>Chapter 7 Synthesis and Electrochemical Properties of Keggin Type Polyoxomolybdate K<sub>4</sub>[SiMo<sub>12</sub>O<sub>40</sub>]</b>	<b>149</b>
7.1 Introduction .....	149

7.2 Experimental .....	149
7.2.1 Synthesis of Materials .....	149
7.2.2 Characterization .....	150
7.2.3 Electrochemical Measurements.....	151
7.3 Results and Discussion.....	152
7.3.1 Crystal Structure.....	152
7.3.2 Thermal Stability.....	153
7.3.3 Electrochemical Performance .....	154
7.3.4 Analysis for the Influence of Annealing Treatment on the Electrochemical Properties .....	160
7.4. Conclusions.....	163
References.....	164
<b>Chapter 8 Summary.....</b>	<b>165</b>
References.....	168
<b>List of Publications.....</b>	<b>169</b>
<b>Acknowledgements.....</b>	<b>171</b>



# Chapter 1

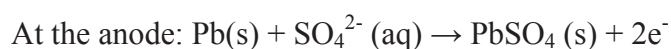
## Introduction

### 1.1 An Overview of Rechargeable (Secondary) Batteries

Chemical batteries are an important power source and have been used in a wide variety of consumer and industrial applications. Rechargeable batteries can be recharged by applying a current in the reverse direction of discharge with the reversible electrode reaction. The original active materials at the cathode and anode electrodes can be chemically and structurally reconstituted by applying electrical potential on the electrodes to “inject” energy. These batteries can be discharged and recharged many times. An overview of the development of rechargeable batteries are shown as follows [1, 2].

#### 1.1.1 Lead-acid Battery

The earliest commercialized rechargeable battery system is known as the lead-acid battery, which was invented in 1859 by Raymond Gaston Planté. The lead-acid cell uses lead as the anode and lead dioxide as the cathode, with acid electrolyte. The following half-cell reactions take place inside the cell during discharge process:



The reversed reactions proceed at the each electrode during the charging process.

There are unavoidable limitations of lead-acid battery, as service life is shortened by (i) corrosion on the positive plate caused by operating the battery at high temperature or by leaving the battery uncharged, (ii) irreversible sulfation on the negative plate occurring when the battery is left unused for a period of time. The product of the discharge reaction, lead sulfate ( $\text{PbSO}_4$ ), will irreversibly recrystallize to larger particles. Once the battery is covered with the non-conductive lead sulfate particles, the battery is inactivated and will not respond to recharging.

Although the lead acid battery is the most used battery in the world, it can be a source of environmental pollution. Some lead compounds are extremely toxic. Long-term exposed to even tiny amounts of these compounds can cause brain and kidney damage, hearing impairment, and learning problems for children.

### **1.1.2 Nickel-Cadmium (Ni-Cd) Battery**

In 1899, Waldmar Junger invented the nickel-cadmium battery, which was successfully commercialized in 1910 as a pocket-plate battery. Nickel hydroxide mixed with graphite acts as the cathode, while cadmium hydroxide or cadmium oxide mixed with iron or iron compounds acts as the anode; potassium hydroxide solution is used as the electrolyte. The following half-cell reactions take place inside the cell during discharge process:



The drawback of Ni-Cd rechargeable battery is that full discharge process is

necessary before the charging process to obtain maximum cell voltage. Otherwise, upon charging the voltage at which discharge ceased will be attained, instead of the maximum voltage possible. This deficiency is referred to as the “memory effect”, which is more pronounced as the increase of charge-discharge cycles. The most serious problem for Ni-Cd battery is the use of toxic Cd, and the usage for small packaged cell was exchanged to Nickel-Metal Hydride battery.

### 1.1.3 Nickel-Metal Hydride (Ni-MH) Battery

The first Ni-MH battery is commercialized in 1989. The cathode in a Ni-MH cell is identical to the one in a Ni-Cd cell, while the anode is a compound of alloys expressed as  $AB_5$  where  $A$  is comprised of an alloy of rare earths: La, Ce, Nd, and Pr while  $B$  is an alloy of Ni, Co, Mn, and Al. The electrolyte is an alkaline solution as in a Ni-Cd cell. The electrochemical reactions during the discharge process are:



In general, Ni-MH battery is less durable than Ni-Cd battery and suffers from high self-discharge, poor cycling ability, and lower shelf-life at higher ambient temperatures. These disadvantages were much improved and currently used as a small package cell. It is also used as the large battery system in hybrid vehicle for its high capacity. Ni-MH also shows the memory effect.

### 1.1.4 Lithium Batteries

The demands for advanced energy storage devices have increased significantly year

by year. Although the above mentioned several rechargeable batteries are widely used in many fields, one of the disadvantages in its low energy density has become a limiting factor for its further large-scale application, particularly, the hybrid electric vehicles (HEV) and electric vehicles (EV), in which the energy demand is much higher. Due to its low electrochemical equivalent weight and high standard potential ( $-3.04$  V vs standard hydrogen electrode), lithium metal has very high specific capacity and high theoretical energy density in comparison with the others base metals and transition metals. Therefore, the research of rechargeable lithium ion battery as the energy storage device has intensified in the past several decades.

The first commercial lithium ion battery was manufactured by Exxon Company (USA) in the 1970s with a  $\text{LiTiS}_2$  cathode. In 1980, Moli Energy (Canada, now E-One Moly Energy Ltd.) commercialized Li batteries with a  $\text{LiMoS}_2$  cathode, while a few years later Taridan (Israel) used a  $\text{Li}_{0.3}\text{MnO}_2$  cathode. These cells used a Li foil as the anode and various liquid organic electrolytes. The Nippon Telegraph and Telephone Corporation (NTT), commercialized a Li battery with a  $\text{LiV}_2\text{O}_5$  cathode and a Li-Al alloy anode that is used until today. The most efficient rechargeable lithium ion battery was commercially introduced by Sony in 1991 after pioneering research by Goodenough et al. This cell consists of a  $\text{LiCoO}_2$  cathode, a carbon anode, and a nonaqueous liquid organic electrolyte (1 M lithium hexafluorophosphate ( $\text{LiPF}_6$ ) in 1:1 weight mixture of EC:DEC (ethylene carbonate:diethyl carbonate)). The energy density (Wh/kg) of these rechargeable lithium batteries vary from 50 Wh/kg to 200 Wh/kg, which are much higher than those of Lead-acid, Ni-Cd, and

Ni-MH batteries, as shown in Figure 1.1.

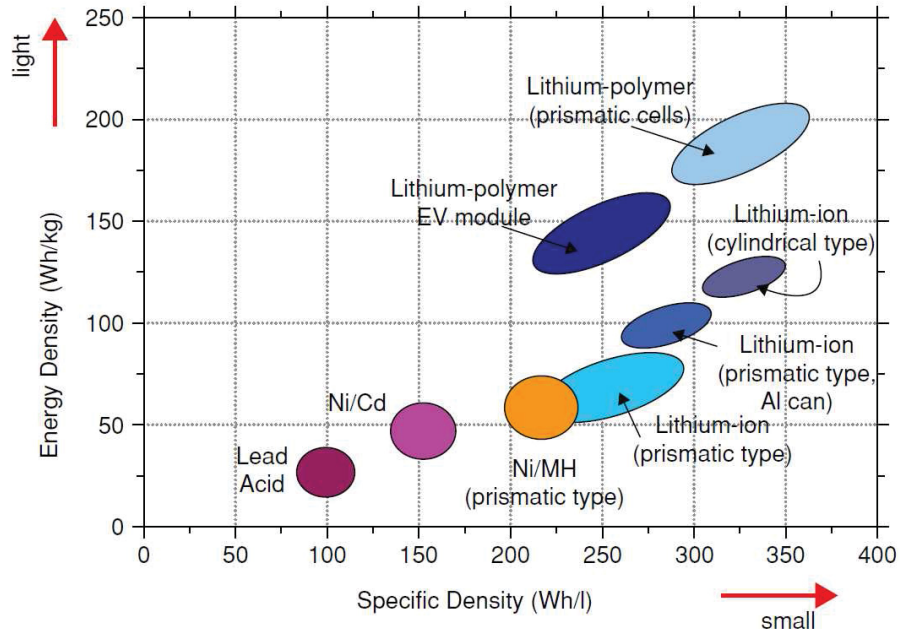
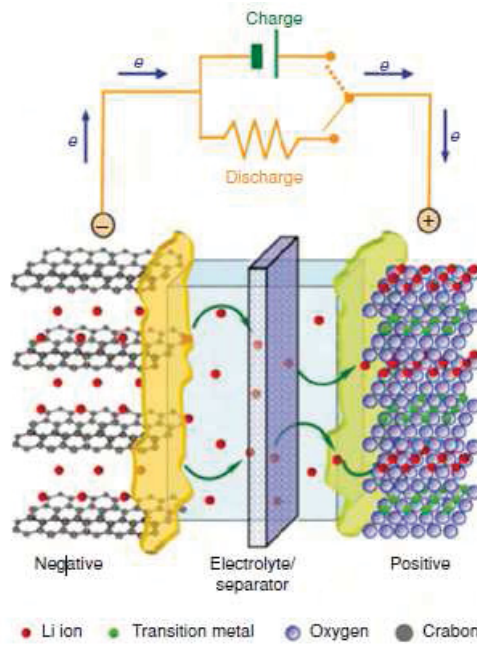


Figure 1.1 Energy density (Wh/kg) vs. specific density (Wh/L) for a series of batteries [3].

Figure 1.2 shows the charge-discharge process involved in the most conventional configuration of transition metal oxide (e.g.  $\text{LiCoO}_2$ ) battery cell. During the charge, lithium ions are removed from the  $\text{LiCoO}_2$  positive electrode and they are intercalated into the graphite framework. To compensate for the transfer of the ionic charges, electrons are also exchanged between the two electrodes. This process is able to be reversed during discharge process.



**Figure 1.2** Illustration of the charge-discharge process involved in the most conventional configuration of transition metal oxide (e.g.  $\text{LiCoO}_2$ ) battery cell [3].

## 1.2 Cathode Materials for Lithium Batteries

### 1.2.1 Materials with Layered Rock-Salt Structure

#### (1) *Lithium Cobalt Oxide ( $\text{LiCoO}_2$ )*

Mizushima et al firstly reported that the lithium could be removed electrochemically in  $\text{LiCoO}_2$ , thus making it a viable cathode material [4].  $\text{LiCoO}_2$  has the layered rock-salt  $\alpha\text{-NaFeO}_2$  structure. This structure is based on a close-packed network of oxygen atoms with the  $\text{Li}^+$  and  $\text{Co}^{3+}$  ions ordering on alternating (111) planes of the cubic rock-salt structure. This (111) ordering introduces a slight distortion to the host and it transits to hexagonal symmetry. Hence  $\text{LiCoO}_2$  crystallizes in the space group  $R\bar{3}m$  with cell constants  $a=2.816 \text{ \AA}$  and  $c=14.08 \text{ \AA}$ . Figure 1.3

shows the ...ABCABC...type stacking of the ...O-Li-O-Co-O-Li-O... triangular sheets [5].

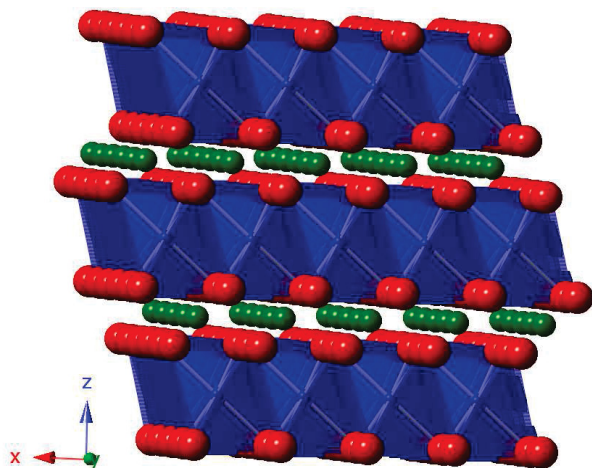


**Figure 1.3** Illustration of the crystal structure of  $\text{LiCoO}_2$  (red: O; blue: Co; green: Li).

Ohzuku *et al* show the following reaction mechanism of  $\text{Li}_{1-x}\text{CoO}_2$  [6].

- (i) In the region  $0 < x < 1/4$ , coexistence of two hexagonal phases was observed. The reaction in this region is inevitably a topotactic two-phase reaction.
- (ii) In the region  $1/4 < x < 3/4$ , a change in the lattice parameters was observed. The reaction in this region is a single-phase reaction as a whole. A monoclinic phase is observed at about  $x=0.45$ .
- (iii) In the region  $3/4 < x < 1$ , a two-phase reaction was indicated.

$\text{LiCoO}_2$  has the theoretical capacity as high as  $274 \text{ mAh g}^{-1}$  due to its low molecular weight. The high energy density brought by this high capacity and high operating voltage around 4 V made this material most commonly used cathode material for lithium battery. However, once more than 50% of the lithium ions are

extracted from between the layers, the structure tends to collapse due to a significant electrostatic repulsion between the transition metal polyhedra such that the reversible capacity is typically limited to about 150 mAh g<sup>-1</sup> [4-7]. In addition, the high cost, toxicity, and low safety concerns associated with LiCoO<sub>2</sub> prevent its use for large-scale energy storage applications, such as transportation and stationary storage applications. To overcome these problems, extensive researches have been made to explore the alternatives to LiCoO<sub>2</sub>. This has led to explore the following compounds based on LiCoO<sub>2</sub> structure by partially or totally substituting the Co with Ni or Mn so as to support the structure against decomposition at the high potential, such as, LiNiO<sub>2</sub>, LiMnO<sub>2</sub>, LiNi<sub>0.5</sub>Mn<sub>0.5</sub>O<sub>2</sub>, LiCo<sub>1/3</sub>Ni<sub>1/3</sub>Mn<sub>1/3</sub>O<sub>2</sub> and Li-rich layered oxide  $x\text{LiMnO}_3 \cdot (1-x)\text{LiMn}_{0.5}\text{Ni}_{0.5}\text{O}_2$ .

## *(2) Lithium Nickel Oxide (LiNiO<sub>2</sub>)*

Lithium nickel oxide LiNiO<sub>2</sub> [8], which is isostructural with LiCoO<sub>2</sub>, is considered as an alternative to LiCoO<sub>2</sub> because of its lower cost, higher reversible capacity and better environmental compatibility. However, it is difficult to synthesize stoichiometric LiNiO<sub>2</sub>. The Li<sub>1-x</sub>Ni<sub>1+x</sub>O<sub>2</sub> phase is usually formed because the instability of the Ni<sup>3+</sup> oxide favors conversion to 2x Ni<sup>2+</sup> and (1-x) Ni<sup>3+</sup> with concomitant loss of x Li [9]. In turn, this gives rise to cation site disorder, since the occupation of Ni<sup>2+</sup> is more favorable in the “interlayer” Li 3b site than Ni<sup>3+</sup> because of the similar size of Ni<sup>2+</sup> and Li<sup>+</sup>. The cation disorder has significant influences on Li<sup>+</sup> diffusion. The presence of Ni<sup>2+</sup> in the interlayer Li<sup>+</sup> sites induces local reduction of

spacing between the transition metal layers because the  $\text{Ni}^{2+}$  is oxidized into the smaller  $\text{Ni}^{3+}$  cation during charge. This results in block of  $\text{Li}^+$  diffusion and irreversible capacity loss in the first cycle [10]. In addition, the position of  $\text{Ni}^{3+}/\text{Ni}^{4+}$  couple in  $\text{LiNiO}_2$  can result in preferential oxidation of the lattice oxide ions and hence evolution of  $\text{O}_2$  in the charge process, leading to the safety issues [11]. The modification of this material by replacing a part of the nickel by other elements such as cobalt and aluminum was carried out.  $\text{LiCo}_{0.3}\text{Ni}_{0.7}\text{O}_2$  shows a lower irreversible capacity due to the lower  $\text{Ni}^{2+} \leftrightarrow \text{Li}^+$  site exchange [12-14], and better structural stability at high temperature [15].  $\text{Li}[\text{Ni}_{1-y-x}\text{Co}_y\text{Al}_x]\text{O}_2$  shows further improved structural stability [11, 16], which is prime candidate for the cathode of advanced lithium battery for hybrid electric vehicles.

The phase transformations of  $\text{Li}_x\text{NiO}_2$  in the charge-discharge process are summarized as follows [17, 18]:

H1 ( $0 < x < 0.15$ )  $\leftrightarrow$  H1+M ( $0.15 < x < 0.25$ )  $\leftrightarrow$  M ( $0.25 < x < 0.5$ )  $\leftrightarrow$  M+H2 ( $0.5 < x < 0.57$ )  
 $\leftrightarrow$  H2 ( $0.57 < x < 0.68$ )  $\leftrightarrow$  H2+H3 ( $0.68 < x$ ) (H: hexagonal, M: monoclinic phase)

### (3) *Lithium Manganese Oxide (LiMnO<sub>2</sub>)*

Layered  $\text{LiMnO}_2$  has been attracted much interest for it can provide not only a low-cost but also an environmentally benign. However, its thermodynamically stable form is a poorly electrochemically active orthorhombic structure that is different from the  $R3-m$  phase [19].  $\text{LiMnO}_2$  shows a small monoclinic ( $C2/m$ ) deformation of the ideal rhombohedral structure because of the Jahn-Teller distortion of  $\text{Mn}^{3+}$ . The

$\text{Li}_{0.5}\text{MnO}_2$  transformed into the spinel  $\text{LiMn}_2\text{O}_4$  structure because the later structure is more stable in the charge-discharge process, resulting in poor electrochemical properties and a spinel-like drop in the voltage profile [20, 21]. In order to suppress the transformation, partial substitution of Mn with Ni ( $\text{Li}_{2/3}[\text{Ni}_{1/3}\text{Mn}_{2/3}]\text{O}_2$ ) [22] and Co ( $\text{Li}_{2/3}[\text{Mn}_{0.85}\text{Co}_{0.15}]\text{O}_2$ ) [23] shows improvement in the electrochemical performance.

#### (4) *Lithium Manganese-Nickel Oxide ( $\text{LiMn}_{0.5}\text{Ni}_{0.5}\text{O}_2$ )*

$\text{LiMn}_{0.5}\text{Ni}_{0.5}\text{O}_2$  with the classic  $\alpha\text{-NaFeO}_2$  (*R3-m*) structure has been demonstrated to show greatly improved electrochemical performance [24, 25]. Initial discharge capacity  $\sim 200 \text{ mAh g}^{-1}$  and high capacity retention after 30 cycles in  $\text{LiMn}_{0.5}\text{Ni}_{0.5}\text{O}_2$  were reported [26].  $\text{LiMn}_{0.5}\text{Ni}_{0.5}\text{O}_2$  shows lower thermal runaway, better structural thermal stability than  $\text{LiCoO}_2$  or  $\text{LiNiO}_2$ , and greater suppression to reaction with electrolyte in the charge state [26-28]. However, 8-10% cation disorder between *3a* and *3b* sites due to the similar size of  $\text{Ni}^{2+}$  and  $\text{Li}^+$  still exists in  $\text{LiMn}_{0.5}\text{Ni}_{0.5}\text{O}_2$ , impeding the Li diffusion. Several groups have carried out the research to reduce the cation disorder in  $\text{LiMn}_{0.5}\text{Ni}_{0.5}\text{O}_2$ . Kang et al. reported that the amount of cation disorder was decreased to 4.3% by preparing the material via ion exchange from  $\text{NaMn}_{0.5}\text{Ni}_{0.5}\text{O}_2$  [29]. This material shows improved rate performance, capacity of  $183 \text{ mAh g}^{-1}$  was obtained at the 6C rate ( $1\text{C} = 280 \text{ mA g}^{-1}$ ). Schougaard et al. reduced the cation disorder by reducing the nickel content in the lithium layer to 5.6%, resulting in a capacity of  $110 \text{ mAh g}^{-1}$  at 4C. Ceder et al. showed that Ni migrates from the Li layer to transition metal sites by electrochemical induction [30, 31]. The cation

disorder was reduced by charging to high voltage (5.3 V vs Li/Li<sup>+</sup>), resulting in better electrochemical performance in the following charge-discharge process [32].

*(5) Lithium Cobalt-Nickel-Manganese Oxide (LiCo<sub>1/3</sub>Ni<sub>1/3</sub>Mn<sub>1/3</sub>O<sub>2</sub>)*

LiCo<sub>1/3</sub>Ni<sub>1/3</sub>Mn<sub>1/3</sub>O<sub>2</sub> has shown particularly promising electrochemical performance for lithium battery [33]. LiCo<sub>1/3</sub>Ni<sub>1/3</sub>Mn<sub>1/3</sub>O<sub>2</sub> is isostructural to LiCoO<sub>2</sub> with Ni, Co, and Mn adopting valence states of 2+, 3+, and 4+, respectively [34, 35]. The structure of was proposed to be a [ $\sqrt{3} \times \sqrt{3}$ ] R30°-type superlattice structure with long-range ordering [33, 34]. It can be considered as a 1:1:1 solid solution of LiCoO<sub>2</sub>, LiNiO<sub>2</sub>, and LiMnO<sub>2</sub> or a 1:2 solid solution between LiCoO<sub>2</sub> and LiMn<sub>0.5</sub>Ni<sub>0.5</sub>O<sub>2</sub> [36, 37]. Li<sub>1-x</sub>Co<sub>1/3</sub>Ni<sub>1/3</sub>Mn<sub>1/3</sub>O<sub>2</sub> not only shows less degree in cation disorder than that of LiMn<sub>0.5</sub>Ni<sub>0.5</sub>O<sub>2</sub> [38-43], but also a small volume change (1-2%) in the range of 0 < x < 0.7 [38, 41, 44, 45]. LiCo<sub>1/3</sub>Ni<sub>1/3</sub>Mn<sub>1/3</sub>O<sub>2</sub> shows good rate performance with capacities of 200 and 150 mAh g<sup>-1</sup> at the current densities of 18.3 and 1600 mA g<sup>-1</sup>, respectively. The excellent electrochemical performance is ascribed to the low amount of cation disorder and the small volume change. In addition, LiCo<sub>1/3</sub>Ni<sub>1/3</sub>Mn<sub>1/3</sub>O<sub>2</sub> is safe at the high stage of charge, compared to LiCoO<sub>2</sub> and LiNiO<sub>2</sub> [46, 47].

*(6) Lithium-Rich Mixed-Metal Oxide (xLi<sub>2</sub>MnO<sub>3</sub>·(1-x)LiMO<sub>2</sub>)*

Excess lithium can be incorporated into the layered structure compound including a solid solution of Li<sub>2</sub>MnO<sub>3</sub> and LiMO<sub>2</sub> (M=Cr, Mn, Fe, Ni, Co) (xLi<sub>2</sub>MnO<sub>3</sub>·(1-x)LiMO<sub>2</sub>) [48-52]. Li<sub>2</sub>MnO<sub>3</sub> with a layered monoclinic C2/m structure can be represented in the normal notation as Li[Li<sub>1/3</sub>Mn<sub>2/3</sub>]O<sub>2</sub>. The LiMO<sub>2</sub> can

comprise  $\text{LiMn}_2\text{O}_4$  (spinel),  $\text{LiMn}_{0.5}\text{Ni}_{0.5}\text{O}_2$  or  $\text{LiCo}_{1/3}\text{Ni}_{1/3}\text{Mn}_{1/3}$ . Figure 1.4 shows the integrated structure of layered  $\text{Li}_2\text{MnO}_3$  ((001) fringes) and spinel  $\text{Li}_4\text{Mn}_5\text{O}_{12}$  ((111) fringes) in nanosize domains [52]. Addition of extra lithium will tend to push the Mn away from  $3+$  to  $4+$ , thus minimizing the impact of any Jahn-Teller distortion originated in  $\text{Mn}^{3+}$ . This material provides an initial capacity over  $250 \text{ mAh g}^{-1}$  when discharged between 5 and 2.0 V vs.  $\text{Li}^+$  and a rechargeable capacity up to  $250 \text{ mAh g}^{-1}$  between the same potential window [48].

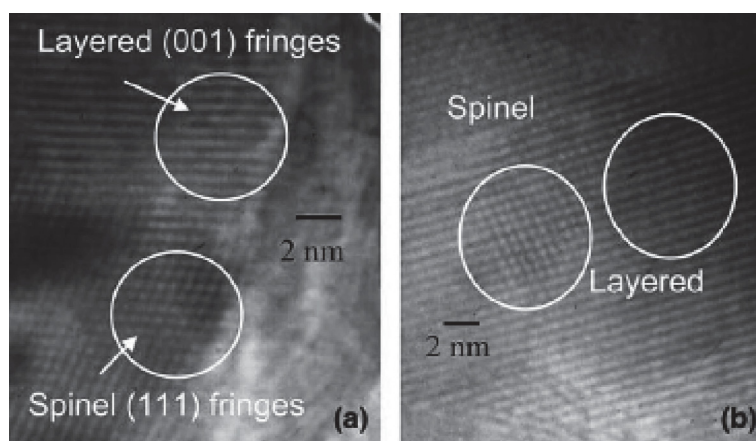


**Figure 1.4** (a ,b) High-resolution TEM images of  $0.7\text{Li}_2\text{MnO}_3 \cdot 0.3\text{Li}_4\text{Mn}_5\text{O}_{12}$  showing the structural compatibility of layered ( $\text{Li}_2\text{MnO}_3$ ) and spinel ( $\text{Li}_4\text{Mn}_5\text{O}_{12}$ ) domains [52].

### 1.2.2 Material with Spinel Structure

$\text{LiMn}_2\text{O}_4$  with spinel structure is an appealing alternative to  $\text{LiCoO}_2$  due to the more chemically stable  $\text{Mn}^{3+}/\text{Mn}^{4+}$  couple offering excellent safety and high power capability [53-60].  $\text{LiMn}_2\text{O}_4$  is considered to be the suitable candidate as the cathode material of a high-power lithium battery for hybrid electric vehicles. Furthermore, Mn is inexpensive and environmentally benign. The structure of  $\text{LiMn}_2\text{O}_4$  is shown in Figure 1.5. The  $\text{Li}^+$  occupies the tetrahedral  $8a$  site in the cubic-closed packed  $\text{O}^{2-}$

lattice, and  $\text{Mn}^{3+}$  resides in the  $16d$  octahedral site.

$\text{LiMn}_2\text{O}_4$  shows capacity loss at the elevated temperatures ( $>50$  °C). Several mechanisms for the capacity loss are summarized as follows.

- (i) Jahn-Teller distortion of  $\text{Mn}^{3+}$  [61].
- (ii)  $\text{Mn}^{2+}$  dissolution into the electrolyte [62].
- (iii) Loss of crystallinity [63].
- (iv) Development of microstrain due to lattice mismatch between two distinct cubic phase forming on cycling [64].
- (v) Increase in oxygen deficiencies or oxygen loss upon cycling [65].

Among these mechanisms, dissolution of  $\text{LiMn}_2\text{O}_4$  by the disproportionation of surface  $\text{Mn}^{3+}$  via the reaction  $2\text{Mn}^{3+} \rightarrow \text{Mn}^{2+} + \text{Mn}^{4+}$  is considered to be the predominant reason [66], because the  $\text{Mn}^{2+}$  is soluble in the acidic electrolyte. Once the  $\text{Mn}^{2+}$  diffuses to the anode and be reduced there to Mn metal, it would use up the lithium and causing the capacity loss of the cell.

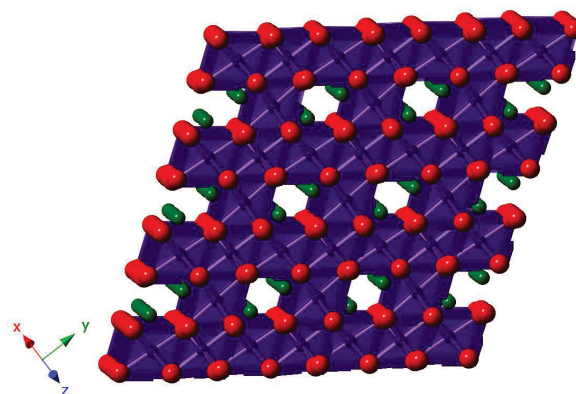


**Figure 1.5** Illustration of the crystal structure of  $\text{LiMn}_2\text{O}_4$  (red: O; purple: Mn; green: Li).

Several approaches to suppress the dissolution of  $\text{LiMn}_2\text{O}_4$  are summarized as

follows. The dissolution of  $\text{LiMn}_2\text{O}_4$  was stabilized by using fluorine or layered metal oxides as proton within the layered oxide lattice [67]. By fluorine substitution for oxygen, spinel  $\text{LiAl}_x\text{Mn}_{2-x}\text{O}_{4-z}\text{F}_z$ , was fabricated, which exhibits enhanced stability at elevated temperature [68, 69]. The partially substituted spinels  $\text{LiM}_y\text{Mn}_{2-y}\text{O}_4$  ( $M = \text{Co}, \text{Cr}, \text{Ni}, \text{Al}, y = 1/12, 1/9, 1/6, 1/3$ ) ( $Fd-3m$ ) showed better cycle performance than the parent  $\text{LiMn}_2\text{O}_4$  [70]. The improvement in cycle performance seems to be attributed to the stabilization in the spinel structure by the doped metal cations.

### 1.2.3 Material with Olivine Structure

The olivine  $\text{LiFePO}_4$  proposed by J. B. Goodenough et al as a new class of cathode material in 1997 [71], has been attracted much attention to enable the production of large-scale lithium batteries due to the following several reasons:

- (i) Low cost, low environmental impact and high safety
- (ii) The very flat discharge plateau around 3.5 V vs  $\text{Li/Li}^+$
- (iii) The capacity of  $170 \text{ mAh g}^{-1}$  is higher than that of  $\text{LiCoO}_2$ , and the cycle performance is very stable.

However,  $\text{LiFePO}_4$  has inherent shortcoming of low electric conductivity ( $10^{-9} \text{ S/cm}$ ), low ionic conductivity due to the one-dimensional lithium ion diffusion transport (Figure 1.6) and a two-phase redox reaction that together limit the mobility of the phase boundary [72-76]. Several approaches have been carried out to improve the electric conductivity. Carbon coating has shown significant improvement in the electric conductivity [77-80]. The electric conductivity of  $\text{LiFePO}_4$  was improved to

around  $10^{-5}$ – $10^{-6}$  [78]. The material coated with carbon-gel during synthesis step shows very stable cycle performance with capacity around  $120 \text{ mAh g}^{-1}$  at high rates [79].  $\text{LiFePO}_4$  doped with polyvalent metals (e.g. Zr, Nb) showed very excellent electrochemical performance, which the electric conductivity was increased 8 orders of magnitude [80, 81]. Preparation of nanocrystallites is also a key to improve the electric conductivity [82, 83]. The particle size with  $\sim 140 \text{ nm}$  shows  $147 \text{ mAh g}^{-1}$  at 5C rate and without significant capacity loss after 400 cycles [82].

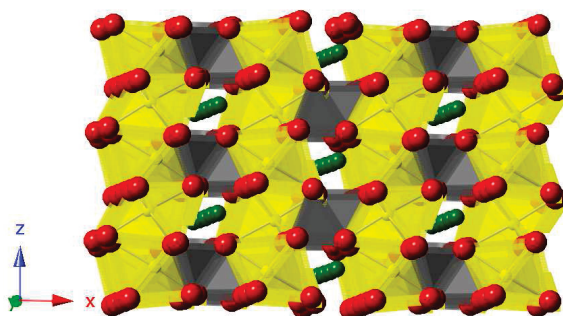


**Figure 1.6** Illustration of the crystal structure of  $\text{LiFePO}_4$  (red: O; yellow: Fe; gray: P; green: Li).

#### 1.2.4 Organic Materials

As an alternative, the electroactive organic compounds or polymers involving reversible redox reactions have attracted interest in recent years due to their higher theoretical capacity. Since the discovery of conducting polymer in 1977 [84], scientists found that they can achieve not only the electronic conductivity that corresponds to those of semiconductors or even metals, but also the redox activity of electrode materials. Thus there are lots of researches on conducting polymers [85-93], organodisulfides [94-103], thioethers [104-107], nitroxyl radical polymers [108], etc. as the alternatives to conventional intercalation materials.

For inorganics, the redox reaction is related to the valence change of the transition-metal or elemental substance, while for organics, the redox reaction is based on change in the electric structure change of the electroactive organic group or moiety. Figure 1.7 illustrates the discharge process of an organic cell.  $A^-$  transports between the cathode and electrolyte, while  $Li^+$  transports between the anode and the electrolyte.

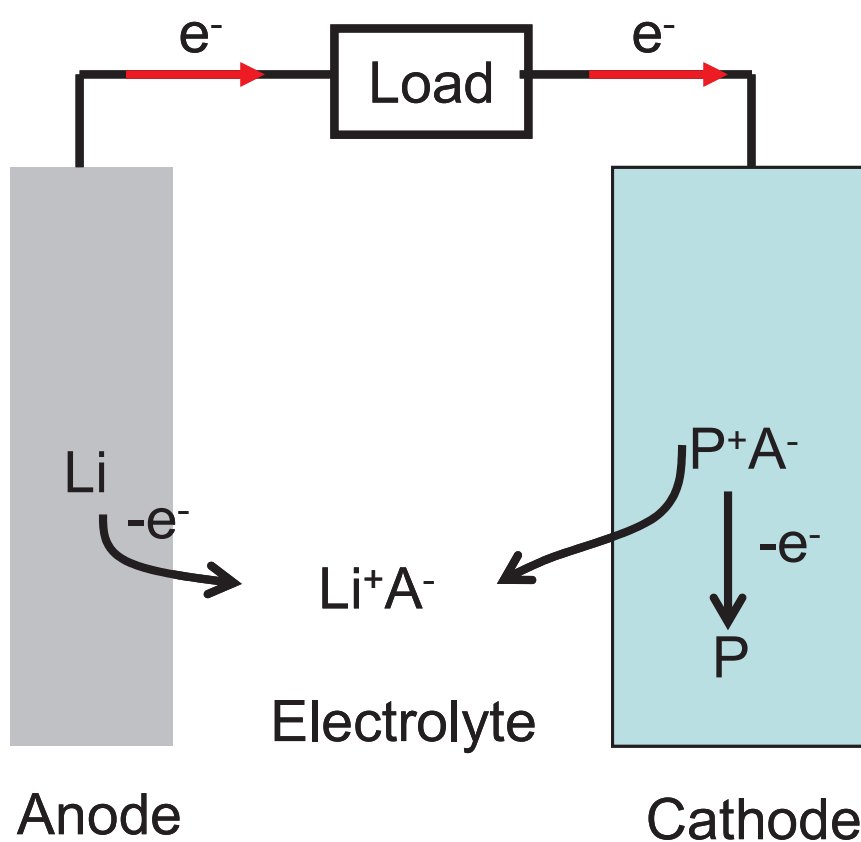


**Figure 1.7** The cell configuration and charge transfer process of organic cathode during the discharge process ( $P^+$  for a polymer in its oxidation state,  $A^-$  for an anion).

Although organic cathode materials show high discharge capacity, the unavoidable dissolution of active materials in the electrolyte is a major problem over a long-term

cycling.

### 1.2.5 Metal Complex and Cluster Ion Materials

The metal complexes have been investigated as the cathode materials of lithium battery, because the metal complexes have characteristics of both transition metal ion and organic compounds and therefore are expected to show unique electrochemical property. Yamaki *et al.* reported that the organo-metallic compounds based on  $\beta$ -phthalocyanine (Pc), such as  $\text{Li}_2\text{Pc}$ ,  $\text{FePc}$ , and  $\text{MnPc}$ , as the cathode materials of lithium ion battery [109, 110]. These materials show lithium intercalation activity with high capacity. Imanishi *et al.* also reported the lithium intercalation into the ferrocyanide  $\text{Fe}_4[\text{Fe}(\text{CN})_6]_3$  [111, 112]. The crystal structures of these complexes (Figure 1.8a and b) are rather like metal oxide and did not show much different property from the oxide materials.

The cluster ion electrodes are also expected to show the intermediate property between the lithium intercalation electrodes and the organic compound electrodes. Usually, cluster ions consist of several or several tens of metal ions in a unit. It behaves as a single molecule under the dissolved condition in solvents. In the solidification process, cluster ions form ionic crystals with some counter ions. These cluster ion materials are expected to show redox activity as an individual molecular cluster, not as a continuum. Therefore, capacity and cycle stability of the cluster ion materials are independent from the stability or recoverability of its crystal structure. This independence of properties from the crystal structure will enable deep

discharge-charge and high capacity. Recently, charge–discharge ability of cluster ion complex was reported by Yoshikawa et al [113] used  $[\text{Mn}_{12}\text{O}_{12}(\text{CH}_3\text{COO})_{16}(\text{H}_2\text{O})_4]$  (Figure 1.8c) as a cathode material. This cluster complex shows the initial discharge capacity of over  $200 \text{ mAh g}^{-1}$ . After the secondary discharge,  $[\text{Mn}_{12}\text{O}_{12}(\text{CH}_3\text{COO})_{16}(\text{H}_2\text{O})_4]$  showed reversible charge–discharge performance with the capacity around  $100 \text{ mAh g}^{-1}$ . They also reported that this cluster complex cannot stand under the highly polarized condition because it contains many organic legends (acetic acid ion) for cluster ion formation. This result demonstrates that organo-metallic cluster ion can not stand for long-term cycling.

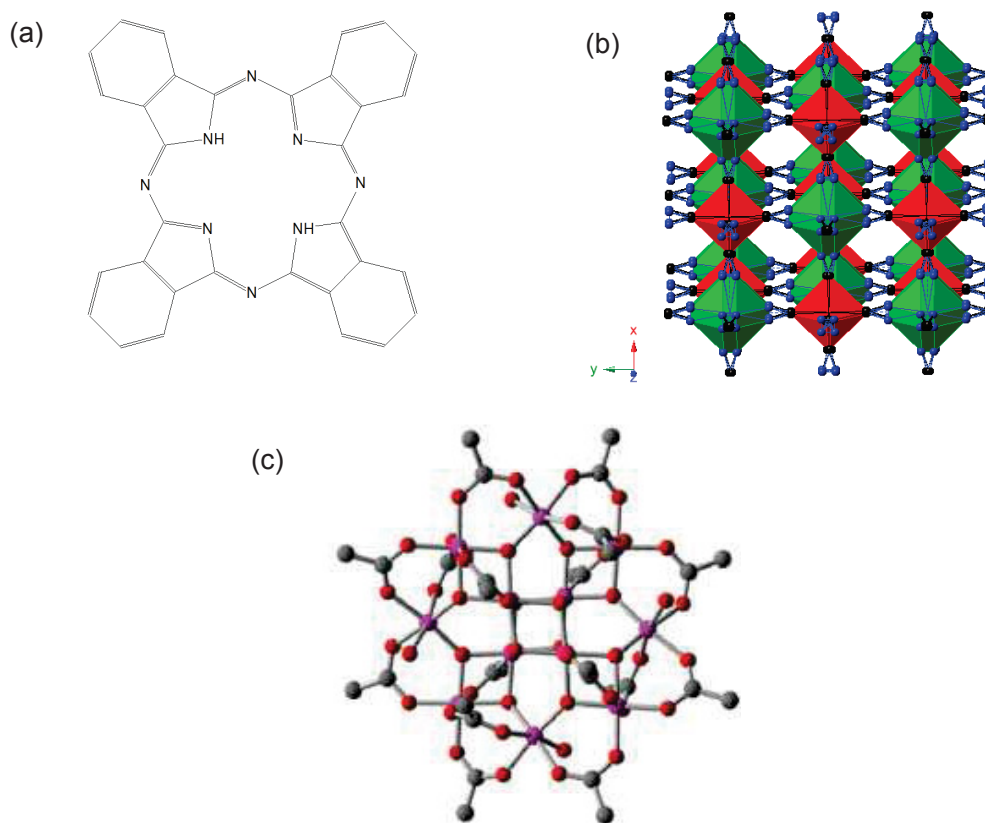


**Figure 1.8** (a) The  $\beta$ -metal free phthalocyanine structure, (b) crystal structure of  $\text{Fe}_4[\text{Fe}(\text{CN})_6]_3$  (Black: C, blue: N, red:  $\text{Fe}^{2+}$ , green:  $\text{Fe}^{3+}$ ) and (c) molecular structure of  $[\text{Mn}_{12}\text{O}_{12}(\text{CH}_3\text{COO})_{16}(\text{H}_2\text{O})_4]$

### 1.2.6 Polyoxometalates (POMs) Materials

At present, the cathode materials widely used for lithium batteries are based on lithium intercalation compounds, e.g.  $\text{LiCoO}_2$ ,  $\text{LiMn}_2\text{O}_4$ , summarized in above sections (1.2.1, 1.2.2, and 1.2.3). The charge-discharge process of these materials depends on the extraction-insertion of the lithium ion located in the lattice structure. Capacity and cycle stability of these lithium intercalation compounds are mainly determined by the recoverability of its crystal structure during the extraction-insertion of lithium ion. Once the lithium ion extracted or inserted over the ratio of recoverability of the crystal structure, these cathode materials would lose cycle stability and battery performance deteriorates seriously.

At present, the achievable specific capacity of the conventional lithium intercalation materials is usually lower than  $200 \text{ mAh g}^{-1}$ , which is insufficient for meeting the increasing energy demand for large-scale applications, such as hybrid electric vehicles (HEVs) and electric vehicles (EVs). Therefore, we have focused on polyoxometalates (POMs), the typical molecular cluster ion materials, as a more suitable alternative for overcoming the intrinsic limitation of the conventional lithium intercalation materials and achieving high capacity. POMs are cluster ion of inorganic oxyanion, not containing any organic ligand, and they are “stable molecules”. Lithium ion can react with these molecular cluster ion units that are independent from the recoverability of crystal structure. Furthermore, multiple electron redox can proceed by the transition metal with high valence number like vanadium and molybdenum in the molecular unit, so high capacity with deep discharge is expected to be obtained in

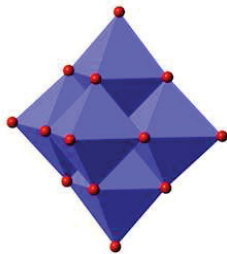
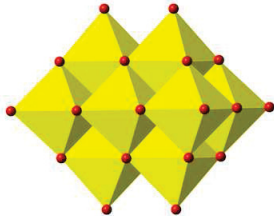
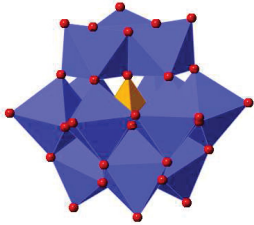
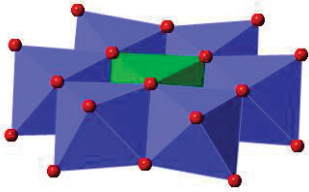
POMs.

*(1) Structures of POMs*

A polyoxometalate is a polyatomic ion, usually an anion, that consists of three or more transition metal (V, Nb, Ta, Cr, Mo, and W) called addenda atoms linked together by sharing oxygen atoms to form a large, closed 3-dimensional framework. The framework of transition metal oxyanions may enclose one or more certain p-block elements (B, Si, Ge, P, As, Sb, Te, I, Al, and Ga) called hetero atoms, themselves sharing neighboring oxygen atoms with the framework [114, 115].

POMs are usually categorized into two parts, one is the iso POMs, another is the hetero POMs. Some representative structures of POMs are shown in Table 1.1

**Table 1.1** Some representation structures for POMs.

Iso POMs	 <p data-bbox="576 1503 794 1536">Lindqvist <math>\text{Mo}_6\text{O}_{19}^{2-}</math></p>	 <p data-bbox="1007 1503 1259 1536">Decavanadate <math>\text{V}_{10}\text{O}_{28}^{6-}</math></p>
Hetero POMs	 <p data-bbox="528 1832 836 1865">Keggin structure <math>\text{PMo}_{12}\text{O}_{40}^{3-}</math></p>	 <p data-bbox="963 1816 1302 1850">Anderson structure <math>\text{AlMo}_6\text{O}_{24}^{3-}</math></p>

*(2) General Properties of POMs*

Several general properties of POMs are summarized as follows [114, 115]:

(i) Water- and air-stable species of large size (6–25 Å) and high ionic weight (*ca.* 1000–10,000).

(ii) High acidity in aqueous solution, POMs are strong acid and POMs are subject to decomposition by hydroxide, e.g.,



Owing to this high acidity of oxide ion, POMs catalyze many organic reactions.

(iii) Some POMs are extremely soluble in water or other polar solvents.

(iv) Crystalline POMs are frequently highly hydrated, with up to 50 molecules of water per anion.

(v) Many polyanions are powerful oxidizing agents and undergo multiple reversible one or two-electron reductions leading to intensely colored mixed valence species known as heteropoly blues. Polyanions are known which can accept as many as 32 electrons without major structural change.

### *(3) Applications of POMs*

The main applications of POMs are summarized as follows [114, 115]:

#### *(i) Catalysis*

POMs have been widely used as heterogeneous catalysts for a broad variety of reactions for its high acidity. For example, oxidation of propylene and isobutylene to acrylic and methacrylic acids, and ammoxidation of acrylonitrile.

#### *(ii) Analysis*

The formation and subsequent precipitation or reduction of  $[\text{XM}_{12}\text{O}_{40}]^{n-}$  anions

form the basis of gravimetric or colorimetric analytic methods for P, As, Si or Ge.

(iii) Biochemical Applications

Phosphotungstic acids have for decades been used as precipitants for proteins, and as analytical reagents for proteins, alkaloids and purines. The use of  $[\text{SiMo}_{12}\text{O}_{40}]^{4-}$  and  $[\text{SiW}_{12}\text{O}_{40}]^{4-}$  as electron acceptors in studies of photosynthesis and photophosphorylation has received attention.

(4) Merits of POMs as Cathode Materials of Lithium Battery

(i) High specific capacity

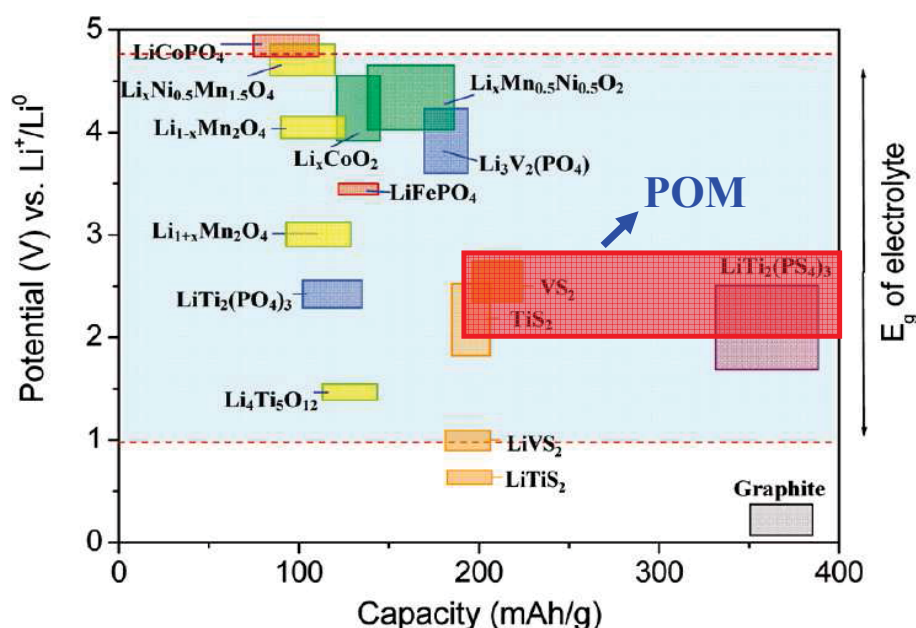


**Figure 1.9** The comparison of POMs as cathode materials with others conventional lithium intercalation materials [116].

Figure 1.9 shows the dependence of potential versus capacity of several electrode materials. It is found that the relatively lower redox potential of POMs cathode can be compensated by their much higher theoretical capacity, thus it is still possible for

them to obtain high energy density. For example,  $K_3[PMo_{12}O_{40}]$  (KPM) with Keggin type structure [117] and  $(KH)_9[PV_{14}O_{42}]$  (KPV) with bi-capped Keggin type structure [118] show initial discharge capacities over  $200 \text{ mAh g}^{-1}$  due to the multi-electron reductions of the transition metals Mo and V.

#### *(ii) Structural diversity*

Although there have been tremendous researches on the conventional lithium intercalation materials, most of them focus on a few materials. At present, it becomes more and more difficult to find new types of lithium intercalation materials and make a breakthrough in battery performance. But for POMs materials, there are huge possibilities in both the structures and properties. Besides the structures listed in Table 1.1, there are still many other structures can be utilized as the cathode materials.

#### *(iii) Low energy and cost in preparation*

Most of POM can be synthesized self-assembly only by adjusting pH value at low temperature, usually lower than  $100 \text{ }^\circ\text{C}$ , and without special expensive equipments, while conventional lithium intercalation materials usually need high temperature synthesis. For example,  $LiCoO_2$  is synthesized at  $>600 \text{ }^\circ\text{C}$  over 20 h [4, 6],  $LiFePO_4$  is synthesized at  $550 \text{ }^\circ\text{C}$  for 6 h [119, 120].

### *(5) Challenges of POMs as Cathode Materials of Lithium Battery*

#### *(i) Structural Stability of Molecular Cluster Ion*

In the previous studies, we have tested electrochemical properties of some Keggin type POMs [117, 118]. With the increase of cycle number, the capacity of

$K_3[PMo_{12}O_{40}]$  (KPM) fades dramatically, which should be due to the unstable structure of molecular cluster ion  $[PMo_{12}O_{40}]^{3-}$  in the electrochemically reduced state (Figure 1.10) [117]. On the other hand,  $(KH)_9[PV_{14}O_{42}]$  (KPV) [118] with stable structure of molecular cluster ion  $[PV_{14}O_{42}]^{9-}$  exhibits excellent cycle stability with capacity retention of 95% after 50 cycles (Figure 1.10). In light of these results, it is suggested that the molecular cluster ion with stable structure during discharge-charge process is very important for preserving the cycle stability of POMs as cathode materials.

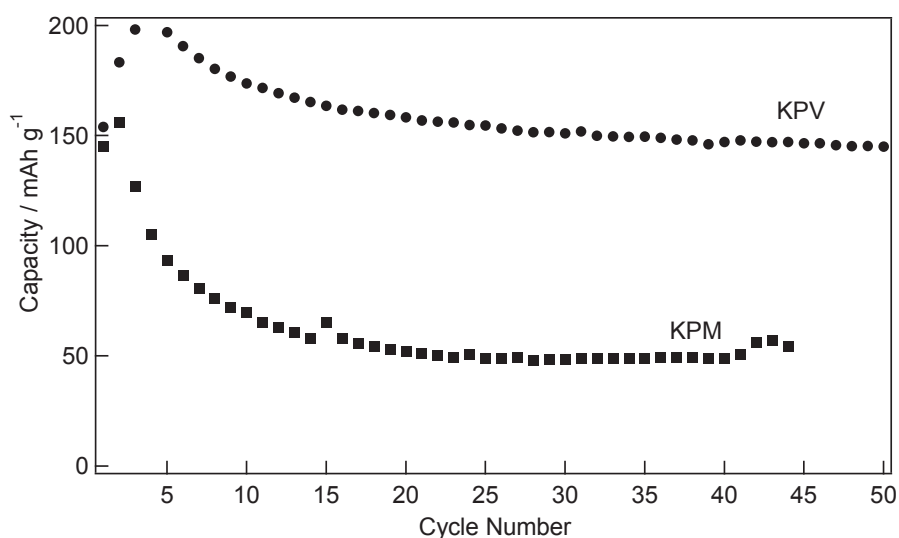


**Figure 1.10** Comparison of cycle performance for KPM and KPV [117, 118].

*(ii) Low Electric Conductivity*

POMs usually tend to show low electric conductivity due to as-prepared crystals are bulk particle in microsize, which suppresses the electrochemical performance of the cathode. The materials with low electric conductivity utilized as cathode materials for lithium ion battery represented by polyanion-based compounds like  $LiFePO_4$ . To improve lithium ion diffusion and charge transfer in the cathode, one of the feasible

ways is to decrease its particle size to nanoscale [79-81], another way is to add conductive additive with higher electric conductivity like the ketjen black (KB) [121-123].

### 1.3 Purposes of this study

To fulfill the demand of high energy for storage devices, this study is to utilize the POMs as cathode materials of lithium battery. To obtain high capacity and stable cycle performance in POMs, the purposes of this study are summarized as follows.

(i) Exploring POMs with stable molecular cluster ion structure as cathode materials of lithium batteries.

The molecular cluster ions in the POMs consisting of the transition metal ions, which are connected with each other by edge-sharing, are expected to be stable during the discharge-charge process due to the strong covalent bonding. In this study, I have explored the POMs with high electrochemical property and structural stability. I selected hetero POMs with edge-sharing connection. I explain each result: the polyoxovanadates:  $K_7[NiV_{13}O_{38}]$  (Chapter 2) and  $K_7[MnV_{13}O_{38}]$  (Chapter 3), polyoxomolybdates:  $(NH_4)_6[NiMo_9O_{32}]$  (Chapter 4),  $(NH_4)_6[MnMo_9O_{32}]$  (Chapter 5), and  $Na_3[AlMo_6O_{24}H_6]$  (Chapter 6).

(ii) Downsizing the crystal particle to improve the electrochemical property.

Most of POMs are water-soluble, and can re-precipitated from the solution by changing the water solvent polarity with organic solvent. In this way, the nanosize particles of POMs can be prepared easily. The particle size of the above POMs was

downsized to nanometer order and the effect of downsizing was discussed in each chapter.

(iii) Investigating the effect of type of conductive additive on the electrochemical property of POMs.

Due to the multistep electron redox can proceed in POMs, the conductive additives with different electric conductivity would give rise to different electrochemical property. From Chapter 2 to Chapter 6, two type of conductive additives, acetylene black (AB) and ketjen black (KB) with different electric conductivities are selected to investigate the influence on the electrochemical performance of these POMs.

(iv) Analyzing the discharge-charge reaction mechanism.

In the investigation of POMs as cathode materials of lithium battery, the reaction mechanism during discharge-charge process is very important, because POMs have intermediate property of the intercalation materials and molecular materials [117, 118], and its properties will depend on the reaction mechanism. To investigate the discharge-charge reaction mechanism, the changes of crystal structures during the electrochemical reaction were probed by the *ex situ* XRD measurements (Chapter 2, Chapter 3, Chapter 4 and Chapter 6). The change of molecular cluster ion structure in the discharge-charge process was investigate by *ex situ* FT-IR (Chapter 2 and Chapter 3) or *ex situ* Raman measurements (Chapter 6). I have discussed the reaction mechanism of POM on the basis of the results of these measurements and mentioned the characteristics of POM as a cathode material of lithium battery.

## References

- [1] D. Linden, T. B. Reddy, *Handbook of Batteries: Third Edition*, McGraw-Hill, 2001.
- [2] K. E. Aifantis, S. A. Hackney, R. V. Kumar, *High Energy Density Lithium Batteries: Materials, Engineering, Applications*, Wiley-VCH, 2010.
- [3] K. M. Abraham, W. A. V. Schalkwijk, J. Hassoun, *Lithium Batteries: Advanced Technologies and Applications*, John Wiley & Sons, Inc., 2013.
- [4] K. Mizushima, P. C. Jones, P. J. Wiseman, J. B. Goodenough, *Mater. Res. Bull.*, 1980, 15, 783–789.
- [5] J. N. Reimers, J. R. Dahn, *J. Electrochem. Soc.*, 1992, 139, 2091–2097.
- [6] T. Ohzuku, A. Ueda, *J. Electrochem. Soc.*, 1994, 141, 2972–2977.
- [7] B. C. Melot, J.-M. Tarascon, *Acc. Chem. Res.*, 2013, 46, 1226–1238.
- [8] J. R. Dahn, U. V. Sacken, C. A. Michal, *Solid State Ionics*, 1990, 44, 87–97.
- [9] A. Rougier, P. Gravereau, C. Delmas, *J. Electrochem. Soc.*, 1996, 143, 1168–1175.
- [10] C. Poullierie, L. Croguennec, Ph. Biensan, P. Willmann, C. Delmas, *J. Electrochem. Soc.*, 2000, 147, 2061–2069.
- [11] B. L. Ellis, K. T. Lee, L. F. Nazar, *Chem. Mater.*, 2010, 22, 691–714.
- [12] I. Saadoun, C. Delmas, *Journal of Materials Chemistry*, 1996, 6, 193–199.
- [13] A. Rougier, I. Saadoun, P. Gravereau, P. Willmann, C. Delmas, *Solid State Ionics*, 1996, 90, 83–90.
- [14] E. Zhecheva, R. Stoyanova, *Solid State Ionics*, 1993, 66, 143–149.
- [15] R. V. Chebiam, F. Prado, A. Manthiram, *J. Electrochem. Soc.*, 2001, 148, A49–A53.

- [16] M. S. Whittingham, *Chem. Rev.*, 2004, 104, 4271–4301.
- [17] T. Ohzuku, A. Ueda, M. Nagayama, *J. Electrochem. Soc.*, 1993, 140, 1862–1870.
- [18] W. Li, J. N. Reimers, J. R. Dahn, *Solid State Ionics*, 1993, 67, 123–130.
- [19] S. K. Mishra, G. Ceder, *Physical Review B: Condensed Matter and Materials Physics* 1999, 59, 6120–6130.
- [20] G. Vitins, K. West, *J. Electrochem. Soc.*, 1997, 144, 2587–2592.
- [21] G. Ceder, A. V. D. Ven, *Electrochim. Acta*, 1999, 45, 131–150.
- [22] J. M. Paulsen, C. L. Thomas, J. R. Dahn, *J. Electrochem. Soc.*, 2000, 147, 861–868.
- [23] J. M. Paulsen, C. L. Thomas, J. R. Dahn, *J. Electrochem. Soc.*, 1999, 146, 3560–3565.
- [24] T. Ohzuku, Y. Makimura, *Chemistry Letters*, 2001, 8, 744–745.
- [25] Z. H. Lu, D. D. MacNeil, J. R. Dahn, *Electrochem. Solid-State Lett.*, 2001, 4, A191–A194.
- [26] Y. Makimura, T. Ohzuku, *J. Power Sources*, 2003, 119–121, 156–160.
- [27] F. Zhou, X. M. Zhao, Z. H. Lu, J. W. Jiang, J. R. Dahn, *Electrochem. Solid-State Lett.*, 2008, 11, A155–A157.
- [28] N. Yabuuchi, Y. T. Kim, H. H. Li, Y. Shao-Horn, *Chem. Mater.*, 2008, 20, 4936–4951.
- [29] K. S. Kang, Y. S. Meng, J. Breger, C. P. Grey, G. Ceder, *Science*, 2006, 311, 977–980.
- [30] J. Breger, Y. S. Meng, Y. Hinuma, S. Kumar, K. Kang, Y. Shao-Horn, G. Ceder, C. P. Grey, *Chem. Mater.*, 2006, 18, 4768–4781.
- [31] C. P. Grey, W. S. Yoon, J. Reed, G. Ceder, *Electrochem. Solid-State Lett.*, 2004, 7, A290–A293.
- [32] N. Yabuuchi, S. Kumar, H. H. Li, Y. T. Kim, Y. Shao-Horn, *J. Electrochem. Soc.*, 2007, 154, A566–A578.

- [33] T. Ohzuku, Y. Makimura, *Chemistry Letters*, 2001, 30, 642–643.
- [34] Y. Koyama, I. Tanaka, H. Adachi, Y. Makimura, T. Ohzuku, *J. Power Sources*, 2003, 191–121, 644–648.
- [35] B. J. Hwang, Y. W. Tsai, D. Carlier, G. Ceder, *Chem. Mater.*, 2003, 15, 3676–3682.
- [36] Y. Koyama, Y. Makimura, I. Tanaka, H. Adachi, T. Ohzuku, *J. Electrochem. Soc.*, 2004, 151, A1499–A1506.
- [37] Z. H. Lu, D. D. MacNeil, J. R. Dahn, *Electrochem. Solid-State Lett.*, 2001, 4, A200–A203.
- [38] S.-C. Yin, Y.-H. Rho, I. Swainson, L. F. Nazar, *Chem. Mater.*, 2006, 18, 1901–1910.
- [39] H. Kobayashi, Y. Arachi, S. Emura, H. Kageyama, K. Tatsumi, T. Kamiyama, *J. Power Sources*, 2005, 146, 640–644.
- [40] P. S. Whitfield, I. J. Davidson, L. M. D. Cranswick, I. P. Swainson, P. W. Stephens, *Solid State Ionics*, 2005, 176, 463–471.
- [41] J. M. Kim, H. T. Chung, *Electrochim. Acta*, 2004, 49, 937–944.
- [42] P. Reale, D. Privitera, S. Panero, B. Scrosati, *Solid State Ionics*, 2007, 178, 1390–1397.
- [43] L. S. Cahill, S.-C. Yin, A. Samoson, I. Heinmaa, L. F. Nazar, G. R. Goward, *Chem. Mater.*, 2005, 17, 6560–6566.
- [44] N. Yabuuchi, Y. Makimura, T. Ohzuku, *J. Electrochem. Soc.*, 2007, 154, A314–A321.
- [45] J. Choi, A. Manthiram, *J. Electrochem. Soc.*, 2005, 152, A1714–A1718.
- [46] N. Yabuuchi, T. Ohzuku, *J. Power Sources*, 2003, 119–121, 171–174.
- [47] Y. D. Wang, J. W. Jiang, J. R. Dahn, *Electrochemistry Communications*, 2007, 9, 2534–2540.
- [48] M. M. Thackeray, C. S. Johnson, J. T. Vaughey, N. Li, S. A. Hackney, *J. Mater. Chem.*, 2005, 15, 2257–2267.

- [49] C. S. Johnson, N. C. Li, C. Lefief, J. T. Vaughey, M. M. Thackeray, *Chem. Mater.*, 2008, 20, 6095–6106.
- [50] C. S. Johnson, J. S. Kim, C. Lefief, N. Li, J. T. Vaughey, M. M. Thackeray, *Electrochemistry Communications*, 2004, 6, 1085–1091.
- [51] M. M. Thackeray, S. H. Kang, C. S. Johnson, J. T. Vaughey, S. A. Hackney, *Electrochemistry Communications*, 2006, 8, 1531–1538.
- [52] C. S. Johnson, N. Li, J. T. Vaughey, S. A. Hackney, M. M. Thackeray, *Electrochemistry Communications*, 2005, 7, 528–536.
- [53] M. M. Thackeray, W. I. F. David, P. G. Bruce, J. B. Goodenough, *Materials Research Bulletin*, 1983, 18, 461–472.
- [54] J.-M. Tarascon, D. Guyomard, *Solid State Ionics*, 1994, 69, 222–237.
- [55] J. M. Tarascon, W. R. McKinnon, F. Coowar, T. N. Bowmer, G. Amatucci, D. Guyomard, *J. Electrochem. Soc.*, 1994, 141, 1421–1431.
- [56] J. M. Tarascon, E. Wang, F. K. Shokoohi, W. R. McKinnon, S. Colson, *J. Electrochem. Soc.*, 1991, 138, 2859–2864.
- [57] M. M. Thackeray, *Progress in Solid State Chemistry*, 1997, 25, 1–71.
- [58] G. Amatucci, J. M. Tarascon, *J. Electrochem. Soc.*, 2002, 149, K31–K46.
- [59] J. M. Tarascon, D. Guyomard, G. L. Baker, *J. Power Sources*, 1993, 44, 689–700.
- [60] J. M. Tarascon, D. Guyomard, *Electrochim. Acta*, 1993, 38, 1221–1231.
- [61] M. M. Thackeray, Y. Shao-Horn, A. J. Kahaian, K. D. Kepler, J. T. Vaughey, S. A. Hackney, *Electrochem. Solid-State Lett.*, 1998, 1, 7–9.
- [62] D. H. Jang, Y. J. Shin, S. M. Oh, *J. Electrochem. Soc.*, 1996, 143, 2204–2211.

- [63] H. Huang, C. A. Vincent, P. G. Bruce, *J. Electrochem. Soc.*, 1999, 146, 3649–3654.
- [64] Y. J. Shin, A. Manthiram, *J. Electrochem. Soc.*, 2004, 151, A204–A208.
- [65] B. H. Deng, H. Nakamura, M. Yoshio, *J. Power Sources*, 2008, 180, 864–868.
- [66] R. Benedek, M. M. Thackeray, *Electrochem. Solid-State Lett.*, 2006, 9, A265–A267.
- [67] A. Manthiram, W. Choi, *Electrochem. Solid-State Lett.*, 2007, 10, A228–A231.
- [68] G. G. Amatucci, N. Pereira, T. Zheng, J.-M. Tarascon, *J. Electrochem. Soc.*, 2001, 148, A171–A182.
- [69] G. G. Amatucci, N. Pereira, T. Zheng, I. Plitz, J. M. Tarascon, *J. Power Sources*, 1998, 81–82, 39–43.
- [70] M. Wakihara, *Electrochemistry*, 2005, 73, 328–335.
- [71] A. K. Padhi, K. S. Nanjundaswamy, J. B. Goodenough, *J. Electrochem. Soc.*, 1997, 144, 1188–1194.
- [72] B. L. Ellis, W. R. Makahnouk, Y. Makimura, K. Toghill, L. F. Nazar, *Nature Materials*, 2007, 6, 749–753.
- [73] A. Yamada, H. Koizumi, S. Nishimura, N. Sonoyama, R. Kanno, M. Yonemura, T. Nakamura, Y. Kobayashi, *Nature Materials*, 2006, 5, 357–360.
- [74] C. Delacourt, P. Poizot, J. M. Tarascon, C. Masquelier, *Nature Materials*, 2005, 4, 254–260.
- [75] T. Maxisch, F. Zhou, G. Ceder, *Phys. Rev. B*, 2006, 73, 104301.
- [76] B. Ellis, L. K. Perry, D. H. Ryan, L. F. Nazar, *J. Am. Chem. Soc.*, 2006, 128, 11416–11422.
- [77] S. Yang, Y. Song, P. Y. Zavalij, M. S. Whittingham, *Electrochemistry Communications*, 2002, 4, 239–244.
- [78] S. Yang, Y. Song, K. Ngala, P. Y. Zavalij, M. S. Whittingham, *J. Power Sources*, 2003,

119–121, 239–246.

[79] H. Huang, S.-C. Yin, L. F. Nazar, *Electrochem. Solid-State Lett.*, 2001, 4, A170–A172.

[80] S.-Y. Chung, J. T. Bloking, Y.-M. Chiang, *Nature Materials*, 2002, 1, 123–128.

[81] P. S. Herle, B. Ellis, N. Coombs, L. F. Nazar, *Nature Materials*, 2004, 3, 147–152.

[82] C. Delacourt, P. Poizot, S. Levasseur, C. Masquelier, *Electrochem. Solid-State Lett.*, 2006, 9, A352–A355.

[83] N. Meethong, H.-Y. S. Huang, W. C. Carter, Y.-M. Chiang, *Electrochem. Solid-State Lett.*, 2007, 10, A134–A138.

[84] H. Shirakawa, E. J. Louis, A. G. MacDiarmid, C. K. Chiang, A. J. Heeger, *J. Chem. Soc., Chem. Commun.*, 1977, 578–580.

[85] P. J. Nigrey, D. MacInnes, Jr, D. P. Nairns, A. G. MacDiarmid, A. J. Heeger, *J. Electrochem. Soc.*, 1981, 128, 1651–1654.

[86] K. Kaneto, K. Yoshino, Y. Inuishi, *Jpn. J. Appl. Phys.*, 1983, 22, L567.

[87] L. W. Shacklette, J. E. Toth, N. S. Murthy, R. H. Baughman, *J. Electrochem. Soc.*, 1985, 132, 1529–1535.

[88] N. Mermilliod, J. Tanguy, *J. Electrochem. Soc.*, 1986, 133, 1073–1079.

[89] A. G. MacDiarmid, S. K. Manohar, J. G. Masters, Y. Sun, H. Weiss, A. J. Epstein, *Synth. Met.*, 1991, 41, 621–626.

[90] N. Gospodinova, L. Terlemezyan, *Prog. Polym. Sci.*, 1998, 23, 1443–1484.

[91] M. Zhou, J. Qian, X. Ai, H. Yang, *Adv. Mater.*, 2011, 23, 4913.

[92] L. Liu, F. Tian, X. Wang, Z. Yang, M. Zhou, X. Wang, *React. Funct. Polym.*, 2012, 72, 45–49.

- [93] L. M. Zhu, A. W. Lei, Y. L. Cao, X. P. Ai, H. X. Yang, *Chem. Commun.*, 2013, 49, 567–569.
- [94] S. J. Visco, L. C. DeJonghe, *J. Electrochem. Soc.*, 1988, 135, 2905–2909.
- [95] M. Liu, S. J. Visco, L. C. D. Jonghe, *J. Electrochem. Soc.*, 1990, 137, 750–759.
- [96] M. Liu, S. J. Visco, L. C. D. Jonghe, *J. Electrochem. Soc.*, 1991, 138, 1891–1895.
- [97] M. Liu, S. J. Visco, L. C. D. Jonghe, *J. Electrochem. Soc.*, 1991, 138, 1896–1901.
- [98] T. Sotomura, H. Uemachi, K. Takeyama, K. Naoi, N. Oyama, *Electrochim. Acta*, 1992, 37, 1851–1854.
- [99] N. Oyama, T. Tatsuma, T. Sato, T. Sotomura, *Nature*, 1995, 374, 196.
- [100] N. Oyama, J. M. Pope, T. Sotomura, *J. Electrochem. Soc.*, 1997, 144, L47–L51.
- [101] N. Oyama, O. Hatozaki, *Macromol. Symp.*, 2000, 156, 171–178.
- [102] N. Oyama, *Macromol. Symp.*, 2000, 159, 221–228.
- [103] J. E. Park, S. Kim, S. Mihashi, O. Hatozaki, N. Oyama, *Macromol. Symp.*, 2002, 186, 35–40.
- [104] J. Y. Zhang, L. B. Kong, L. Z. Zhan, J. Tang, H. Zhan, Y. H. Zhou, C. M. Zhan, *J. Power Sources*, 2007, 168, 278–281.
- [105] J. Tang, Z.-P. Song, N. Shan, L.-Z. Zhan, J.-Y. Zhang, H. Zhan, Y.-H. Zhou, C.-M. Zhan, *J. Power Sources*, 2008, 185, 1434–1438.
- [106] L. Zhan, Z. Song, J. Zhang, J. Tang, H. Zhan, Y. Zhou, C. Zhan, *Electrochim. Acta*, 2008, 53, 8319–8323.
- [107] L. Zhan, Z. Song, N. Shan, J. Zhang, J. Tang, H. Zhan, Y. Zhou, Z. Li, C. Zhan, *J. Power Sources*, 2009, 193, 859–863.
- [108] K. Nakahara, S. Iwasa, M. Satoh, Y. Morioka, J. Iriyama, M. Suguro, E. Hasegawa, *Chem.*

- Phys. Lett.*, 2002, 359, 351–354.
- [109] J. Yamaki, A. Yamaji, *J. Electrochem. Soc.*, 1982, 129, 5–9.
- [110] S. Okada, J. Yamaki, T. Okada, *J. Electrochem. Soc.*, 1989, 136, 340–344.
- [111] N. Imanishi, T. Morikawa, J. Kondo, Y. Takeda, O. Yamamoto, N. Kinugasa, T. Yamagishi, *J. Power Sources*, 1999, 79, 215–219.
- [112] N. Imanishi, T. Morikawa, J. Kondo, R. Yamane, Y. Takeda, O. Yamamoto, H. Sakaebe, M. Tabuchi, *J. Power Sources*, 1999, 81-82, 530–534.
- [113] H. Yoshikawa, C. Kazama, K. Awaga, M. Satoh, J. Wada, *Chem. Commun.*, 2007, 30, 3169–3170.
- [114] M. T. Pope, Y. Jeannin, M. Fournier, *Heteropoly and Isopoly Oxometalates*. Springer-Verlag: Berlin Heidelberg New York Tokyo, 1983.
- [115] J. J. Borrás-Almenar, E. Coronado, A. Müller, M. Pope, *Polyoxometalate Molecular Science*, Kluwer Academic Publishers: The Netherlands, 2003.
- [116] J. B. Goodenough, Y. Kim, *Chem. Mater.*, 2010, 22, 587–603.
- [117] N. Sonoyama, Y. Suganuma, T. Kume, Z. Quan, *J. Power Sources*, 2011, 196, 6822–6827.
- [118] S. Uematsu, Z. Quan, Y. Suganuma, N. Sonoyama, *J. Power Sources*, 2012, 217, 13–20.
- [119] A. Yamada, H. Koizumi, S. Nishimura, N. Sonoyama, R. Kanno, M. Yonemura, T. Nakamura, Y. Kobayashi, *Nature Materials*, 2006, 5, 357–360.
- [120] S. Nishimura, G. Kobayashi, K. Ohoyama, R. Kanno, M. Yashima, A. Yamada, *Nature Materials*, 2008, 7, 707–711.
- [121] P. P. Prosini, M. Lisi, D. Zane, M. Pasquali, *Solid State Ionics*, 2002, 148, 41–51.
- [122] Z. Bakenov, I. Taniguchi, *J. Power Sources*, 2010, 195, 7445–7451.

[123] S. Kurodaa, N. Taboria, M. Sakurabab, Y. Sato, *J. Power Sources*, 2003, 119–121, 924–928.



# Chapter 2

## Synthesis and Electrochemical Properties of Polyoxovanadate



### 2.1 Introduction

In this chapter, polyoxovanadate  $\text{K}_7[\text{NiV}_{13}\text{O}_{38}]$  (KNV), has been studied as cathode material for lithium battery. Figure 2.1 shows the structure of molecular cluster anion  $[\text{NiV}_{13}\text{O}_{38}]^{7-}$  and crystal structure of KNV [1]. The molecular cluster ion  $[\text{NiV}_{13}\text{O}_{38}]^{7-}$  consists of eleven  $\text{VO}_6$  octahedra which share edges with the central  $\text{NiO}_6$  octahedron, while the other two  $\text{VO}_6$  octahedra located at the terminal of the structure share only one oxygen atom with the central  $\text{NiO}_6$  octahedron, and all of the  $\text{VO}_6$  octahedra share edges with each other. This molecular structure is expected to be stable for the high covalent bonding of the octahedra sharing their edges with each other. Thus, KNV could be a promising candidate of POMs as cathode material of lithium battery due to its potential structural stability.

To improve lithium ion diffusion and electron transfer in KNV electrode, one of the feasible ways is to decrease the particle size to nanoscale, another way is to add conductive additive with higher electric conductivity like ketjen black (KB). Most of POMs are soluble in aqueous or organic solvents as an individual ion and can crystallize again by the change of the solvents polarity [2-4]. In light of this

characteristic, the simple re-precipitation method was used to prepare the nanosize particles of KNV. The influences of KB and acetylene black (AB) as conductive additives on the electrochemical property of KNV electrode were investigated.

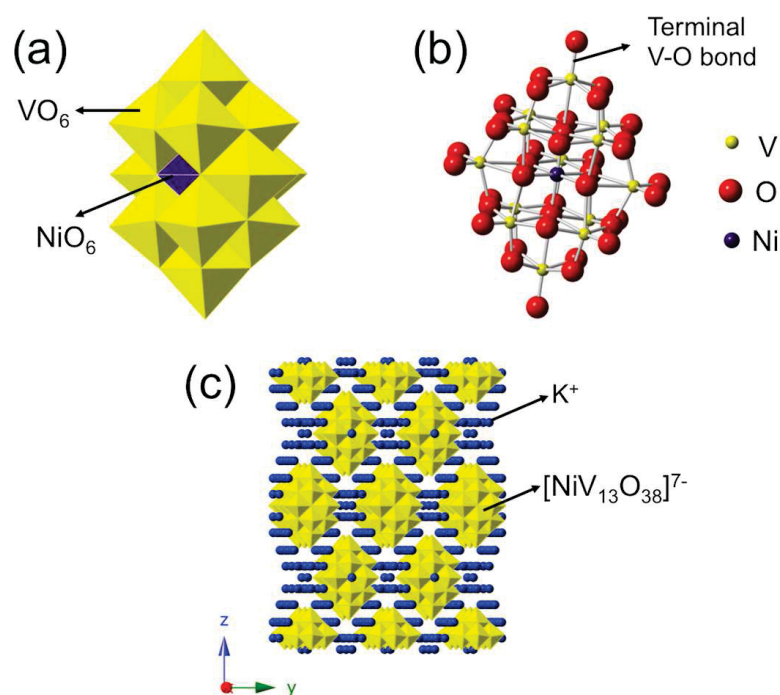


**Figure 2.1** (a) Polyhedral representation for structure of molecular cluster ion  $[\text{NiV}_{13}\text{O}_{38}]^{7-}$ , (b) ball-and-stick representation for structure of molecular cluster ion  $[\text{NiV}_{13}\text{O}_{38}]^{7-}$  and (c) crystal structure of KNV.

Furthermore, there are considerable micropores with diameter  $< 2$  nm (Figure 2.2a) and mesopores with 2-20 nm diameter (Figure 2.2b) within the KB particle agglomerate [5]. If the dissolved KNV as the precursor solution was impregnated into these micropores or mesopores, nanocomposite would be obtained by the *in situ* re-precipitation method. The nanocomposite is expected to show higher capacity and rate performance due to the shorter lithium ion diffusion path and higher contact

surface area with the conductive additive. The changes of crystal structure and the stability of molecular cluster ion  $[\text{NiV}_{13}\text{O}_{38}]^{7-}$  during the discharge-charge process were investigated by *ex situ* XRD and *ex situ* FT-IR measurements, respectively.

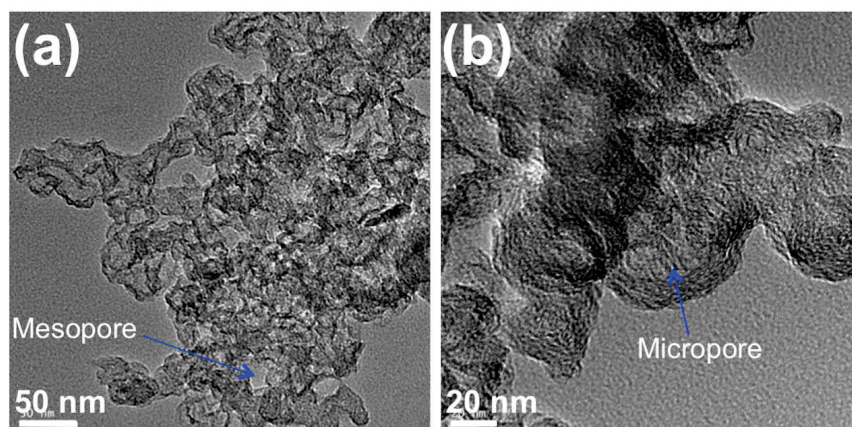


**Figure 2.2** (a) TEM image of KB and (b) magnification of image a.

## 2.2 Experimental

### 2.2.1 Synthesis of Materials

#### *(1) Synthesis of KNV*

The synthesis of KNV was carried out by a modification of the reported method [1]. A solution of 7.18 g of  $\text{KVO}_3$  in 180 ml of hot distilled water was treated with 4 ml 1 M nitric acid, 4 ml of 1 M nickel sulfate, and 2.16 g of potassium peroxydisulfate, in that order. The mixture was kept at 80 °C and stirred and evaporated the solution and controlled the solution volume at 60 ml after 5 h, then filtered the hot solution as fast as possible. The filtrate was treated with 8 ml 1 M potassium acetate. After stirring overnight, the precipitate was filtered and washed with a little 0.5 M potassium acetate–0.5 M acetic acid, then washed with 4/1 (v/v) acetone/water. To remove the

water contained in powder, obtained powders were dried at 120 °C under air for 1h.

### *(2) Synthesis of Nanosize Particles*

The synthesis of nanosize KNV particles was carried out as follows: 0.2 g of as-prepared KNV powder was dissolved in 10 ml distilled water. The precipitate of re-crystallized KNV was immediately obtained by adding 50 ml acetone to the solution. The re-precipitated particles were centrifuged, washed with acetone.

### *(3) Synthesis of nanocomposite KNV/KB*

For the synthesis of nanocomposite KNV/KB (KNV *in situ* re-precipitated in the micropores or mesopores of KB matrix), 0.6 g KB powders were added to the 20 ml solution containing 0.322 g (to obtain the weight ratio of KNV /KB=2/1 for electrode fabrication, the water loss of 7.24% for KNV after drying treatment is calculated) dissolved as-prepared KNV powders, followed with ultrasonic dispersion for 30 min, then added 100 ml acetone to the mixture, filtered and washed the product with acetone.

## **2.2.2 Characterization**

The crystal structure was identified by X-ray diffraction (XRD) measurement using a powder X-ray diffractometer (Rigaku RAD-C) with Cu K $\alpha$  radiation. The diffraction data were collected from 10° to 90° in  $2\theta$ . Thermal stability study was carried out by thermogravimetric analysis (TG) and differential thermal analysis (DTA) (Rigaku TG8101D). The TG/DTA experiment was performed at a heating rate of 10 °C/min up to 700 °C under air. Morphological analysis of samples was obtained with a

scanning electron microscopy (SEM) (HITACHI S-4800). FT-IR spectra were collected with a JASCO-410 spectrometer in the range of 400–1100  $\text{cm}^{-1}$ . Pellets for FT-IR measurement were prepared by grinding and pressing samples with dried KBr powder. *Ex situ* XRD measurements were carried out under Ar atmosphere by enclosing the cathode sample in lab made cell equipped with Mylar film window. *Ex situ* FT-IR measurements were performed with the transmission method. The cathode samples were grinded with dried KBr powder and pressed in IR cell enclosed with KBr windows under Ar atmosphere.

### **2.2.3 Electrochemical Measurements**

The cathode consisted of KNV active material, AB or KB conductive additive and PTFE binder in the weight ratio of 32:64:4, otherwise noted. The electrochemical properties of KNV electrode were tested at 25 °C by using CR-2032 coin cells, which were assembled in an argon filled glovebox using metallic lithium (Honjyo metal) as anode, and 1 M  $\text{LiPF}_6$  in mixture of ethylene carbonate (EC) and diethyl carbonate (DEC) (3:7, v/v: Kishida battery grade) as the electrolyte solution. The discharge-charge properties of the cells were recorded on a battery tester (Interface model OZO-A19) between 1.5 and 4.2 V (vs.  $\text{Li/Li}^+$ ) at the current densities from 17 to 1500  $\text{mA g}^{-1}$ . The cyclic voltammetry (CV) data were obtained with a potentiostat (Solarton 1280) with scan rate of 0.05  $\text{mV s}^{-1}$  between 1.5 and 4.2 V.

## 2.3 Results and Discussion

### 2.3.1 Crystal and Molecular Structures

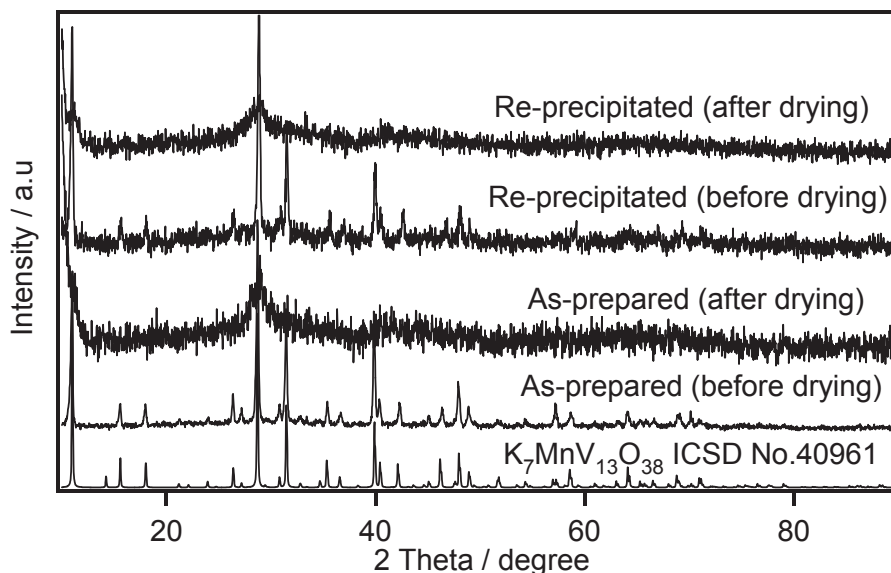


**Figure 2.3** XRD patterns for as-prepared and re-precipitated KNV before and after drying treatment.

The XRD pattern of as-prepared (before drying) KNV is shown in Figure 2.3. All the reflections of the as-prepared KNV (before drying) agree with those of the isomorphous  $K_7MnV_{13}O_{38}$  in ICSD No.40961. The XRD pattern of the re-precipitated product (before drying) agrees with the above mentioned as-prepared KNV, indicating that the crystal structure was well maintained by re-precipitation. Almost all of reflections for the as-prepared and re-precipitated KNV after drying except for the main reflection at  $29^\circ$  disappeared. This indicates that KNV crystal becomes amorphous by drying treatment. Some of polyoxometalates are known to be difficult to crystallize without the aid of crystal water, and become amorphous by removing

crystal water [6].

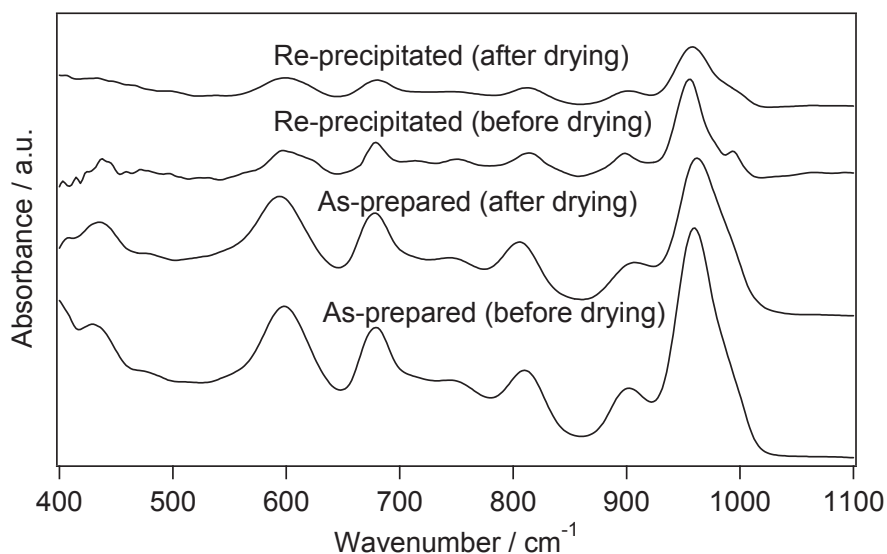


**Figure 2.4** FT-IR spectra for as-prepared and re-precipitated KNiV before and after drying treatment.

To confirm the stability of molecular structure of the  $[\text{NiV}_{13}\text{O}_{38}]^{7-}$  anion as redox active unit after drying, FT-IR spectra were measured, as shown in Figure 2.4. It is clear that the FT-IR spectra of the dried samples are consistent with those of samples before drying. The similar characteristic absorption bands of the hetero-polyanion at 400–1100  $\text{cm}^{-1}$  were observed for the samples with and without drying treatment, demonstrating that the molecular structure of the  $[\text{NiV}_{13}\text{O}_{38}]^{7-}$  anion was still maintained after drying treatment.

### 2.3.2 Thermal Stability

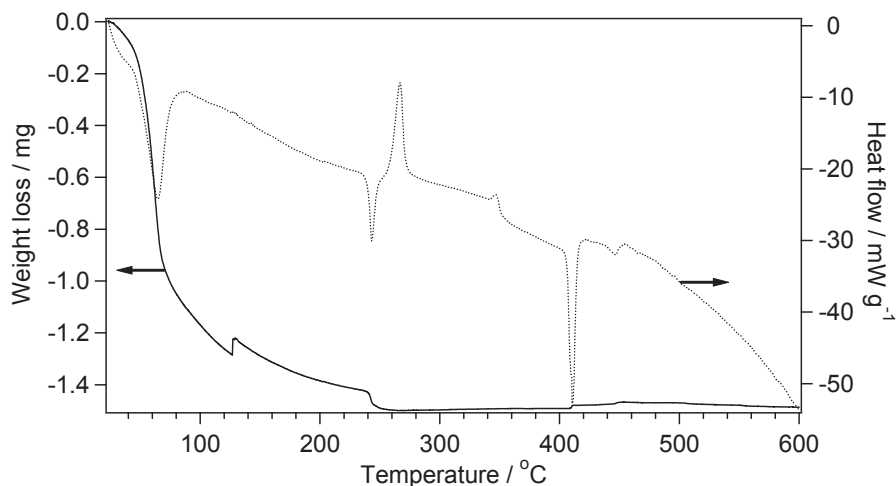


**Figure 2.5** TG-DTA curves of KNV

Figure 2.5 shows TG-DTA analysis of the as-prepared KNV. The significant water loss associated with endothermic peak exhibited around 80 °C. The obvious exothermal peak appeared at 280 °C indicates the decomposition of KNV.

### 2.3.3 Crystal Morphologies

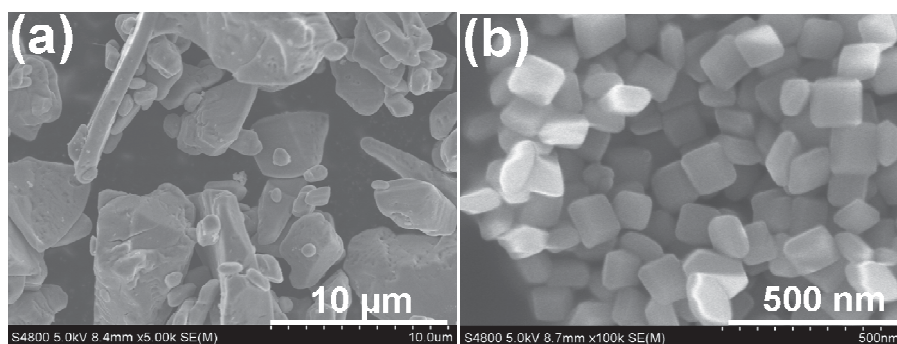


**Figure 2.6** SEM images of (a) as-prepared KNV and (b) re-precipitated KNV.

The morphologies of as-prepared and re-precipitated crystals are shown in Figure 2.6. It is found that the morphology of the as-prepared particles (Figure 2.6a) is very different from those of the re-precipitated particles (Figure 2.6b). The as-prepared

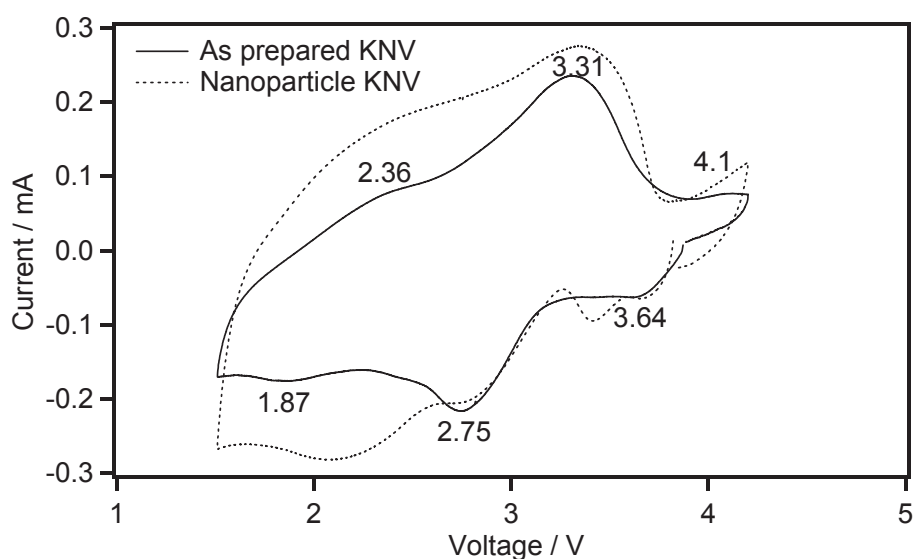
KNV shows micro-sized particles with rather inhomogeneous size distribution, whereas the re-precipitated KNV forms nano-sized particles with regular geometric shape. The following analysis is shown for explaining the formation of nanoparticles. The as-prepared KNV powder is soluble in water and acetone is the water-soluble organic solvent, the polarity of the water solvent can be easily changed by addition of acetone. In this way, the solubility of KNV in the water solution will be affected by polarity variation of the solvent, so once the KNV in the solution reached the oversaturation state, it can precipitate again from the solution. In order to shorten the time of crystal growth to suppress the formation of large size crystal, the acetone was quickly added to the solution to change the polarity of solvent rapidly. Additional continuous stirring accompanied with the addition of acetone can promote the homogeneous nucleation in the solution. As a result, the fine nano-sized grain can be obtained easily.

### **2.3.4 Electrochemical Properties**

#### *(1) CV Curves*

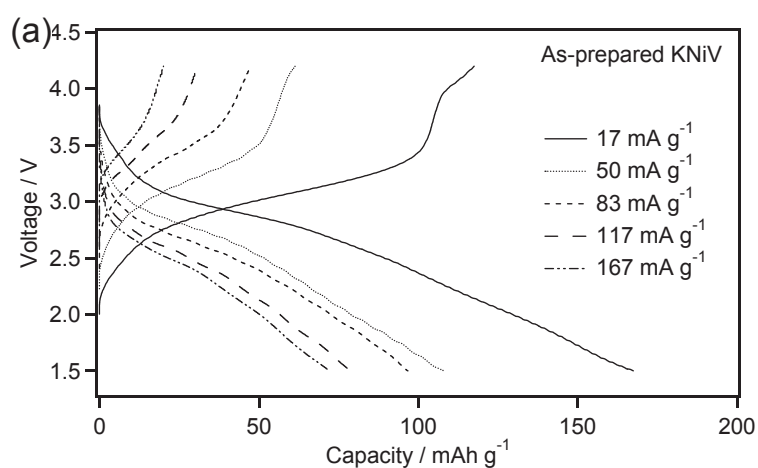
Figure 2.7 shows the CV curves of the as-prepared and nanoparticle KNV. Both the electrodes have three pairs of broad redox peaks between 1.5 and 4.2 V. However, the positions and intensities of the cathodic and anodic peaks for the as-prepared KNV are somewhat different from those of the nanoparticle KNV. Three cathodic peaks around 3.64, 2.75 and 1.87 V and three corresponding anodic peaks around 4.1, 3.31 and 2.36 V are observed for the as-prepared KNV. On the other hand, the nanoparticle

KNV exhibits broader cathodic and anodic peaks around the corresponding voltages. The CV measurements for the KNV cathode demonstrate the reversible reaction with  $\text{Li}^+$  in the electrode accompanying the multi-electron redox, which will enable KNV cathode to fulfill high specific capacity.



**Figure 2.7** CV curves of as-prepared KNV and nanoparticle KNV.

(2) *Effects of AB Conductive Additive on the Discharge-Charge Performance*



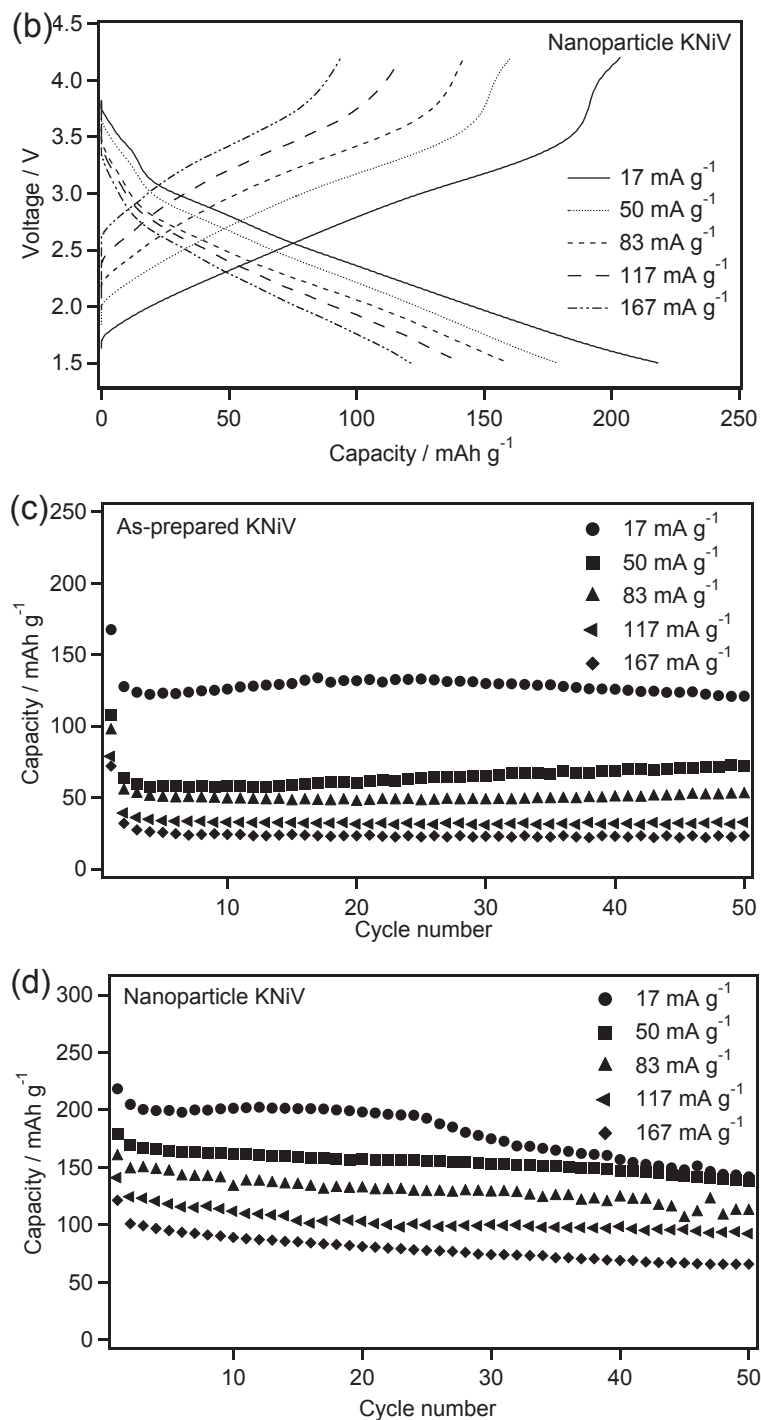


**Figure 2.8** The first discharge-charge curves of (a) as-prepared KNV and (b) nanoparticle KNV at various current densities; cycling performance of (c) as-prepared KNV and (d) nanoparticle KNV at various current densities.

Figure 2.8a and b show the initial discharge-charge curves of the as-prepared and

nanoparticle KNV at various current densities: 17, 50, 83, 117 and 167 mA g<sup>-1</sup>, respectively. One well-defined and two obscure plateaus are observed on both the initial discharge and charge curves for both the as-prepared and nanoparticle KNV at low current density of 17 mA g<sup>-1</sup>, in close agreement with the CV curves. The steep drop and rise in voltage at the beginning of discharge process and the end of charge process would be due to the large polarization caused by the low electric conductivity of KNV. A large irreversible capacity of as-prepared KNV would also be induced by the large polarization. The gradual decrease in the initial discharge capacity with increasing current density for the as-prepared KNV also suggests the low conductivity of KNV. It is known that the downsizing of the particle to nanoscale and homogeneous mixing with the conductive aid can improve the electrochemical property of the materials with low electric conductivity represented by LiFePO<sub>4</sub> [7, 8].

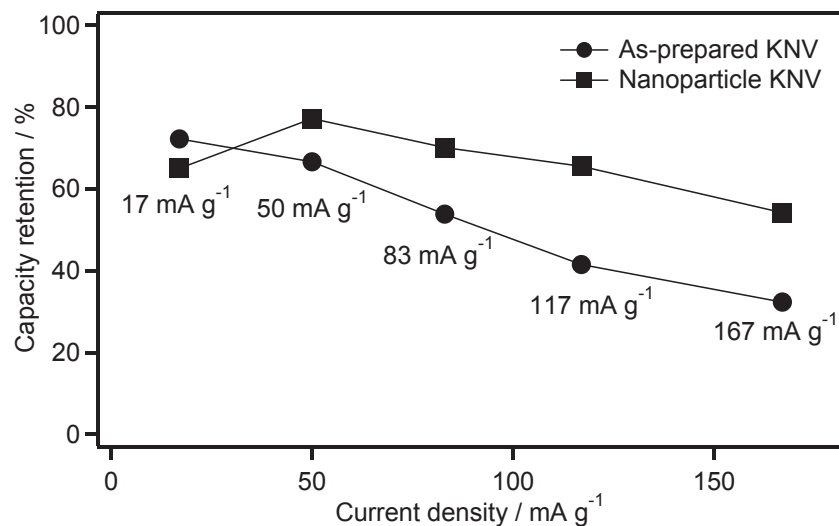
The particles of the molecular cluster ions, which dissolve into the solvent, can be easily downsized by simple re-precipitation. Actually, KNV is downsized to nanoparticle by re-precipitation. The initial discharge capacity of KNV is improved to over 200 mAh g<sup>-1</sup> at the current density of 17 mA g<sup>-1</sup> and irreversible capacity also decreased by nanosizing, as shown in Figure 2.8b. The initial discharge capacities of as-prepared KNV at current densities of 17, 50, 83, 117 and 167 mA g<sup>-1</sup> are 167.5, 107.5, 96.8, 78.8 and 71.9 mAh g<sup>-1</sup>, respectively, while that of the nanoparticle KNV increase to 218.2, 178.8, 159.5, 141 and 121.3 mAh g<sup>-1</sup>, respectively. This improvement in the rate capability performance would also be caused by downsizing of KNV. It should be also noted that on the first discharge-charge cycle the

as-prepared KNV shows the high irreversibility in capacity, while the nanoparticles can provide a marked improvement in the reversible capacity. Each of the as-prepared samples in Figure 2.8a has a coulombic efficiency of 70.1%, 56.8%, 49%, 39.1% and 27.8% at the current densities of 17, 50, 83, 117 and 167 mA g<sup>-1</sup>, respectively. On the other hand, those of the nanoparticle samples in Figure 2.8b exhibit 93.2%, 89.8%, 89.2%, 83.2% and 77.5%, respectively. This drastic improvement in the coulombic efficiencies is evidently caused by the downsizing of KNV to nanoscale.

Cycling performance of the as-prepared and nanoparticle KNV is compared at various current densities from 17 to 167 mA g<sup>-1</sup> after 50 cycles, as shown in Figure 2.8c and d, respectively. It can be seen that the as-prepared KNV exhibits a steep capacity fade on the second cycle. It is worthwhile to highlight that the as-prepared KNV shows somewhat different cycling performance at current densities from 17 to 167 mA g<sup>-1</sup>. The electrodes exhibit good cycling performance at the current densities from 83 to 167 mA g<sup>-1</sup> after the first 5 cycles; however, after 50 cycles, very low discharge capacities of 52.1, 32.7 and 23.2 mAh g<sup>-1</sup> are obtained at 83, 117 and 167 mA g<sup>-1</sup>, respectively. At the current density of 50 mA g<sup>-1</sup>, the discharge capacity gradually increases with cycling after the first 10 cycles. The phenomenon of capacity increase with cycling was also reported for the NH<sub>4</sub>V<sub>3</sub>O<sub>8</sub> nanorod as cathode material [9], which might be caused by the polarization of electrode due to the large particles for lithium ion diffusion. Although a similar increase in discharge capacity with cycling during the cycles 5–25, which is also observed at the lowest current density of 17 mA g<sup>-1</sup>, the electrode shows gradual capacity fade with cycling after the 25th cycle.

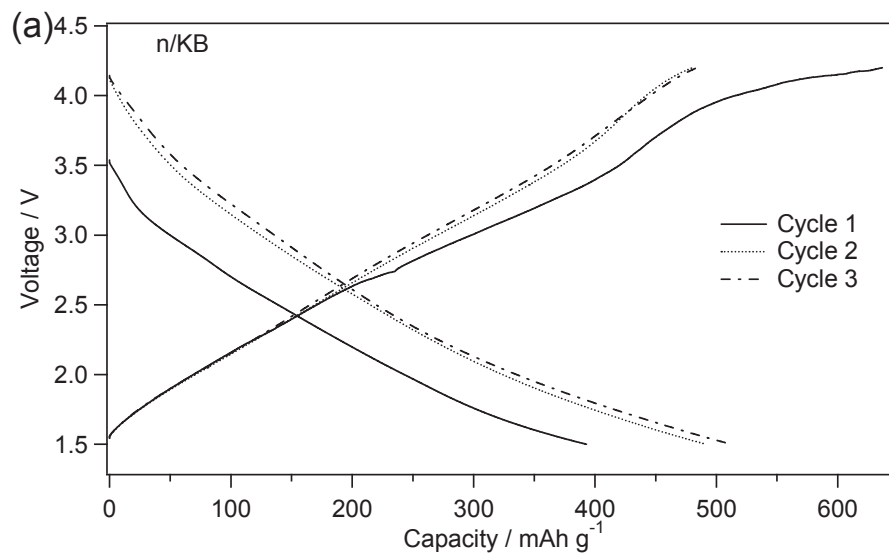
After 50 cycles, capacities of 121 and 71.9 mAh g<sup>-1</sup> are observed at the current densities of 17 and 50 mA g<sup>-1</sup>, respectively.

The nanoparticle KNV almost shows the similar cycling performance at various current densities from 50 to 167 mA g<sup>-1</sup>, except at the low current density of 17 mA g<sup>-1</sup>. Slight capacity fading with the cycle number is observed after the first cycle; however, it is important to note that the nanoparticle KNV shows considerable improvement in the discharge capacity for long-term cycling, in comparison with the as-prepared KNV. After 50 cycles, the nanoparticle KNV deliver discharge capacities of 138, 111.8, 92.4 and 65.7 mAh g<sup>-1</sup> at 50, 83, 117 and 167 mA g<sup>-1</sup>, respectively. At the low current density of 17 mA g<sup>-1</sup>, the nanoparticles show relatively stable cycling performance with a reversible capacity of ~200 mAh g<sup>-1</sup> during cycles 2–24 and thereafter, the capacity rapidly decreases with cycling, which is more unstable than that of the as-prepared KNV at the same current density. Although the capacity slightly decreases with cycle number for the nanoparticle KNV, the capacity retention after the 50 cycles is better than that of the as prepared KNV, as shown in Figure 2.9. It should be noted that nanoparticle KNV shows much higher capacity retention than that of the as-prepared KNV at relatively higher current densities. After 50 cycles, 65.5% and 54.2% capacity retention are observed for the nanoparticle KNV at 117 and 167 mA g<sup>-1</sup>, respectively, while those of the as-prepared KNV are 41.5% and 32.3%, respectively. The high discharge capacity and capacity retention of the nanoparticle KNV compared to the as prepared micro-sized particle KNV would be due to the higher specific surface area and shorter diffusion length of Li ions.



**Figure 2.9** Capacity retention dependence of the current density after 50 cycles.

*(3) Effects of KB Conductive Additive on the Discharge-Charge Performance*



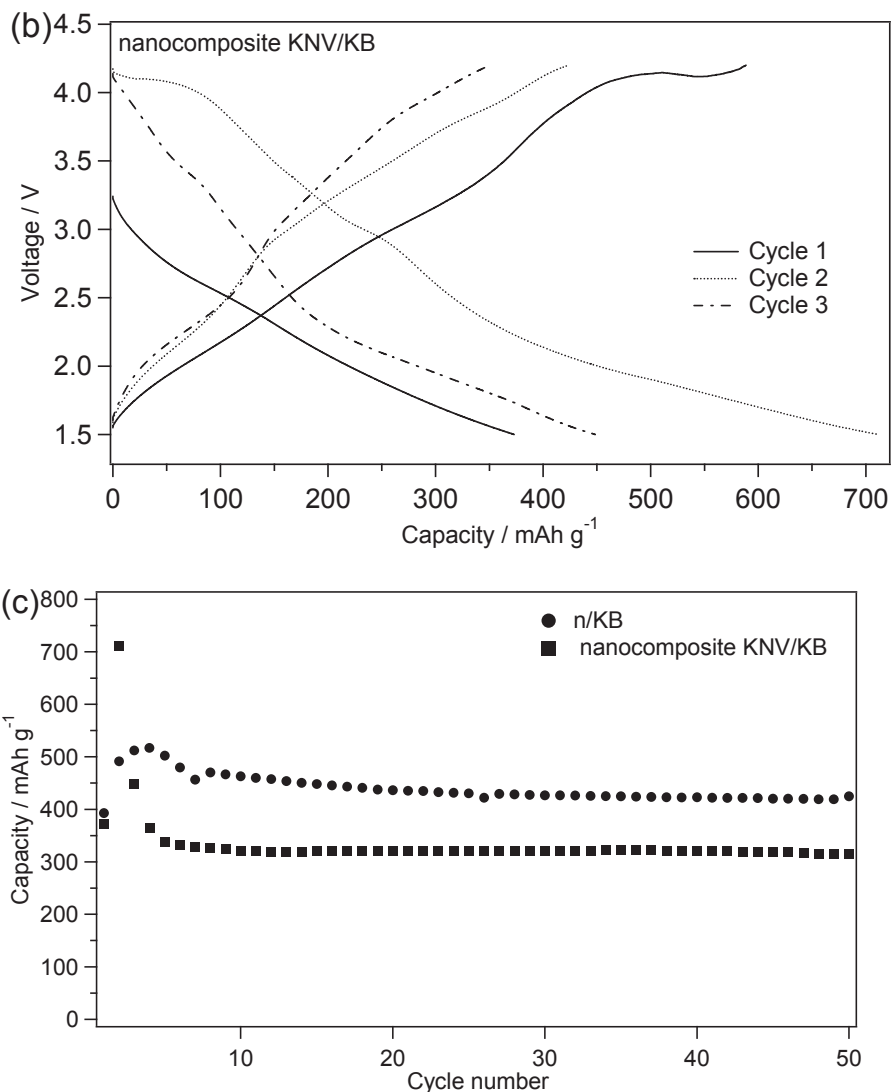


**Figure 2.10** First three discharge-charge curves of (a) nanoparticle KNV mixed with KB (n/KB) and (b) KNV *in situ* re-precipitated in pores of KB matrix (nanocomposite KNV/KB), (c) cycle performance of n/KB and nanocomposite KNV/KB at the low current density of 17 mA g<sup>-1</sup>.

Due to the multi-electron redox that becomes possible in the discharge-charge process by using POMs as cathode materials [6, 10], much higher discharge capacity of KNV is expected to be obtained by mixing nanosize particles with the conductive additive with higher electric conductivity in comparison with the AB conductive additive. Hence, the KB with larger specific surface area was chosen as conductive

additive because it has higher electric conductivity and larger surface area than that of AB [11]. As expected, initial discharge capacity of  $393 \text{ mAh g}^{-1}$  (Figure 2.10a), which is much higher than that of nanosize particles mixed with AB, is obtained. KNV *in situ* re-precipitated in the pores of KB matrix (nanocomposite KNV/KB) also show initial discharge capacity of  $373 \text{ mAh g}^{-1}$ , which is lower than that of n/KB. After 50 cycles, capacity of  $425 \text{ mAh g}^{-1}$  is obtained for n/KB, while capacity of  $315 \text{ mAh g}^{-1}$  is obtained for nanocomposite KNV/KB.

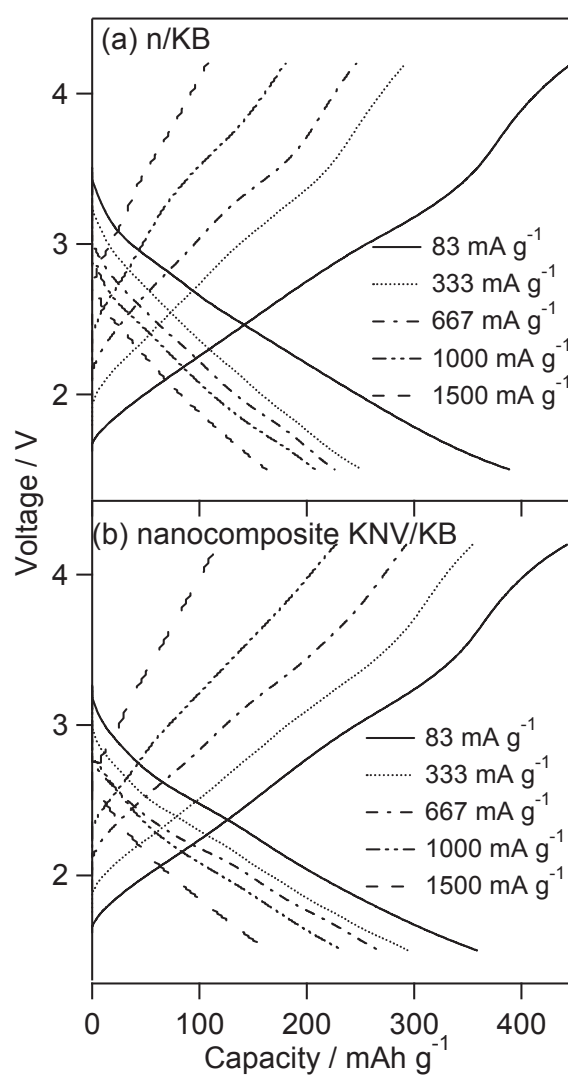


**Figure 2.11** First discharge-charge curves of (a) n/KB and (b) nanocomposite KNV/KB at various current densities.

Figure 2.11 shows the first discharge-charge curves for n/KB and nanocomposite KNV/KB at higher various current densities. With the increase of current density, the initial discharge capacity decreases due to increase of polarization.

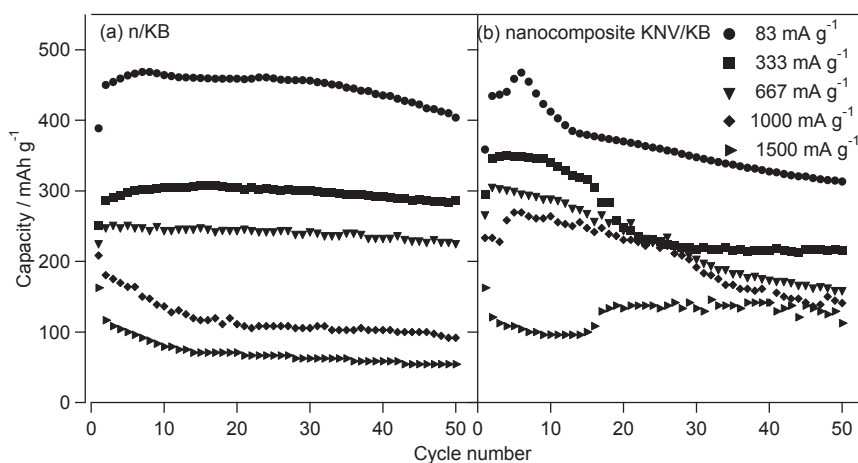


**Figure 2.12** Cycle performance of (a) n/KB and (b) nanocomposite KNV/KB at various current densities.

Figure 2.12 shows the cycle performance for n/KB and n/KB composite at various current densities. n/KB shows the stable cycle performance at the current densities from 83 to 667 mA g<sup>-1</sup>. The capacity fades at the current densities from 1000 to 1500 mA g<sup>-1</sup>. nanocomposite KNV/KB shows capacity loss at the current densities form 83 to 1000 mA g<sup>-1</sup>. It is noted that, with long-term cycling, nanocomposite KNV/KB shows higher capacity that than n/KB at the high rate (current densities from 1000 to 1500 mA g<sup>-1</sup>). The dramatic capacity loss of nanocomposite KNV/KB should be due to the dissolution of the much smaller nanosize KNV (< 20 nm) *in situ* re-crystallized in KB into the electrolyte, compared to the nanosize KNV (~150 nm). This would cause the loss of active material and the poor cycle performance at the low rate

because the longer contact time between the active material and electrolyte. On the other hand, when cycling at the high rate ( $> 1000 \text{ mA g}^{-1}$ ), the contact time between KNV and electrolyte would be shortened, in this case, nanocomposite n/KB would show the advantage in fast electronic and lithium ion diffusion due to the smaller particle size.

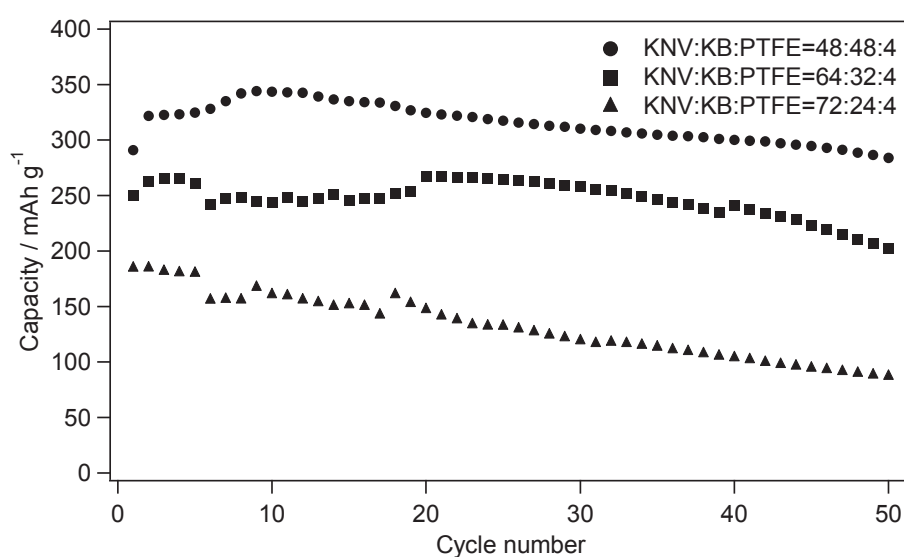


**Figure 2.13** Effect of the cathodes consisting of various weight ratios of KNV:KB:PTFE on the cycle performance of nanosize ( $\sim 150 \text{ nm}$ ) KNV.

The high carbon loading of the cathode decreases the energy density of cell. The relationship between the loading KB weight, that effectively improved the electrochemical property of KNV, and the cycle performance of KNV was investigated. The cycle performance of the cathodes consisting various weight ratios of KNV:KB:PTFE is shown in Figure 2.13. The discharge capacity of KNV decreased as the KB loading was decreased. This result indicates that low amount of the

conductive additive was insufficient to cover the surface of all KNV particles, leading to the low discharge capacity and poor cycle performance.

### 2.3.5 Discharge-Charge Reaction Mechanism

To investigate the discharge-charge reaction mechanism of KNV as cathode material of lithium ion battery, the change of crystal structure during discharge-charge process was studied by *ex situ* XRD measurement, as shown in Figure 2.14. The sample without drying was used, because KNV crystal easily changed to amorphous by drying treatment. It is clearly shown that all of the reflections disappeared when the cathode initially discharged to 3.0 V, indicating the structure of KNV became amorphous, and this amorphous state was maintained until the end of discharge at 1.5 V. In the following recharge to 4.2 V (after 1 cycle), the structure was irreversible and still in amorphous state. This state did not change after 5 cycles. It is suggested that the reaction with lithium ion continuously proceeded in amorphous KNV, which is independent from the recoverability of crystal structure.

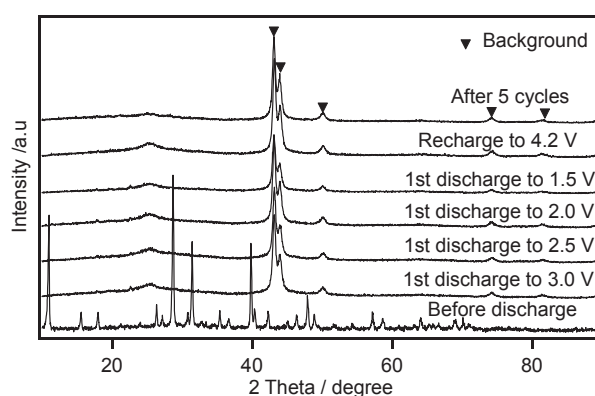


**Figure 2.14** *Ex situ* XRD patterns of KNV cathode recorded at different voltages in the first discharge, after 1 cycle and after 5 cycles.

To investigate the structural change of  $[\text{NiV}_{13}\text{O}_{38}]^{7-}$  molecular cluster ion during the discharge-charge process, *ex situ* FT-IR spectra of KNV cathode discharged and recharged to different voltages in the first cycle are plotted in Figure 2.15. The absorbance peak at wavenumber of  $958\text{ cm}^{-1}$  for the sample before discharge corresponds to the stretching vibration of terminal V-O bond (Figure 2.1b) in structure of  $[\text{NiV}_{13}\text{O}_{38}]^{7-}$  cluster ion [12]. In the initial discharge process, the absorbance peak gradually shifted to lower wavenumber with the insertion of lithium ion into the cathode. In the following recharge process, this absorbance peak gradually shifted back to higher wavenumber with the extraction of lithium ion from the cathode, and got back to the almost original position before discharge. The red shift of the V-O vibration would correspond to the reduction/oxidation of vanadium ion, because it is reasonable V-O stretching energy decreases with the reduction of vanadium (V) ion for the decrease in the electrostatic interaction between vanadium ion and oxide ion. The reversible shift of V-O bond indicates that the structure of  $[\text{NiV}_{13}\text{O}_{38}]^{7-}$  cluster ion was stable and reversible during the discharge-charge process.

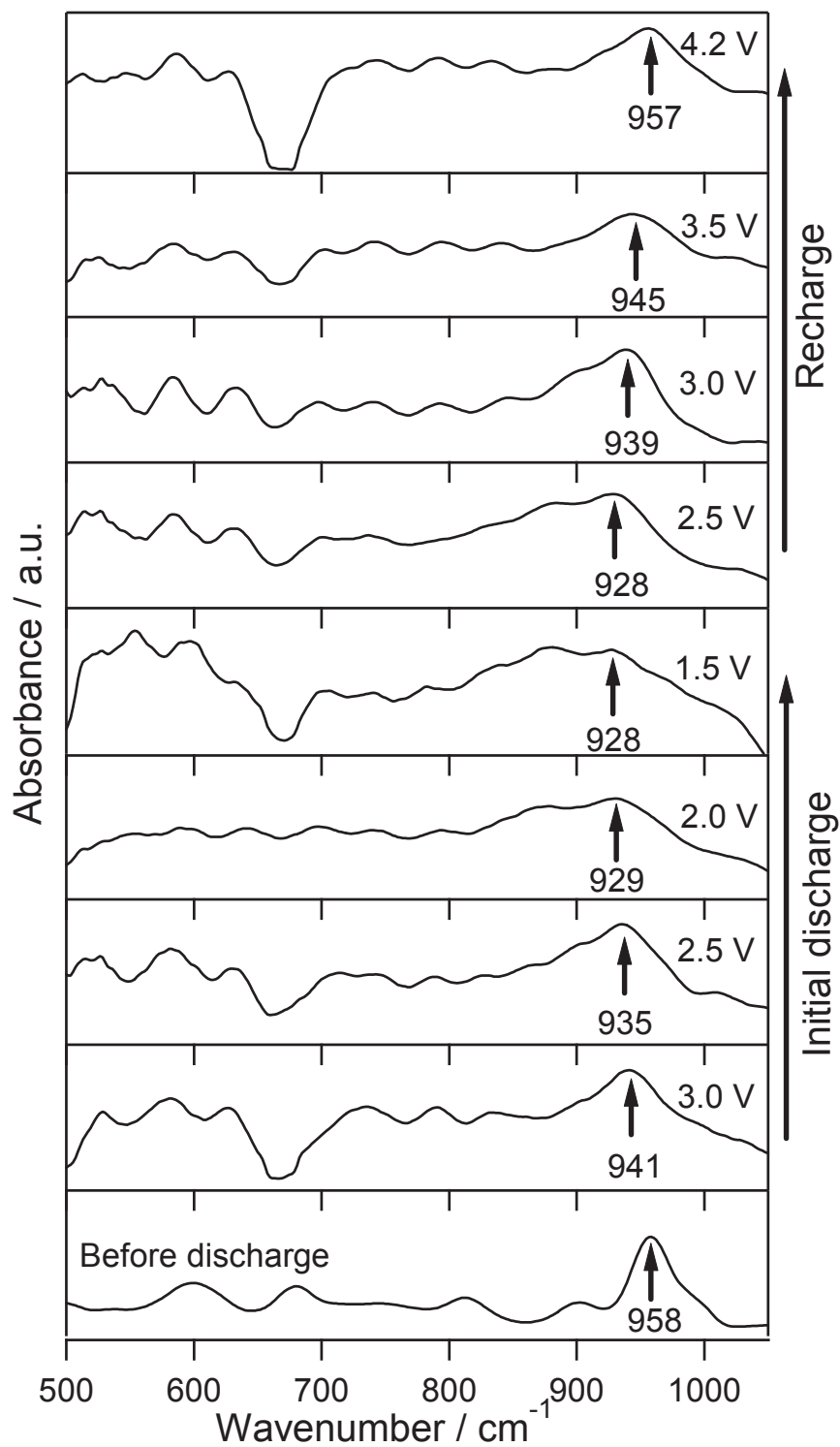


**Figure 2.15** *Ex situ* FT-IR spectra of KNV cathode recorded at different voltages in the first discharge and charge process.

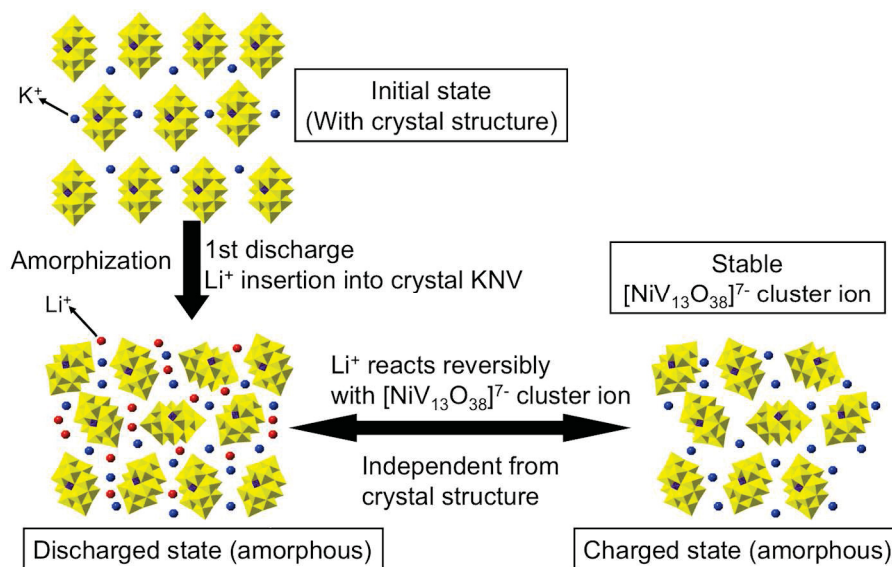


**Figure 2.16** Schematic illustration of the discharge-charge reaction mechanism for KNV cathode

On the basis of the results from *ex situ* XRD and *ex situ* FT-IR measurements, a schematic illustration for the discharge-charge reaction mechanism of KNV is shown in Figure 2.16. The crystal structure of KNV changes to amorphous accompanied with lithium ion inserts into the cathode in the initial discharge process. In the following recharge process, KNV is still in amorphous state, and the  $[\text{NiV}_{13}\text{O}_{38}]^{7-}$  molecular cluster ion reacts reversibly with lithium ion. The reaction with lithium ion can continuously proceed in amorphous KNV upon the discharge-charge cycle, which is independent from the recoverability of crystal structure.

## 2.4 Conclusions

To improve the electrochemical capacity and rate capability, the nanoparticle KNV was prepared, which shows improved electrochemical properties. Marked improvement in initial discharge capacity can be achieved by using the nanoparticle

KNV compared to the as-prepared micro-sized KNV. Furthermore, the discharge capacity was greatly improved by adding KB conductive additive with high electric conductivity. The discharge-charge process proceeds continuously with amorphous KNV, which is independent from the crystal structure. The molecular cluster ion  $[\text{NiV}_{13}\text{O}_{38}]^{7-}$  is stable and reacts reversibly with lithium ion in the discharge-charge process. It is demonstrated that the nanosize polyoxovanadate can be utilized as a novel cathode material for lithium battery, which exhibits comparable capacity and rate capability.

## References

- [1] C. M. Flynn Jr., M. T. Pope, *J. Am. Chem. Soc.*, 1970, 92, 85–90.
- [2] L. E. Briand, G. M. Valle, H. J. Thomas, *J. Mater. Chem.*, 2002, 12, 299–304.
- [3] S. Himeno, M. Hashimoto, T. Ueda, *Inorganica Chimica Acta*, 1999, 284, 237–245.
- [4] S. Himeno, T. Osakai, A. Saito, T. Hori, *Bull. Chem. Soc. Jpn.*, 1992, 65, 799–804.
- [5] T. Soboleva, X. Zhao, K. Malek, Z. Xie, T. Navessin, S. Holdcroft, *ACS Appl. Mater. Interfaces*, 2010, 2, 375–384.
- [6] S. Uematsu, Z. Quan, Y. Suganuma, N. Sonoyama, *J. Power Sources*, 2012, 217, 13–20.
- [7] S-T. Myung, S. Komaba, N. Hirosaki, H. Yashiro, N. Kumagai, *Electrochim. Acta*, 2004, 49, 4213–4222.
- [8] H. Liu, C. Li, H. P. Zhang, L. J. Fu, Y. P. Wu, H. Q. Wu, *J. Power Sources*, 2006, 159, 717–720.
- [9] H. Y. Wang, Y. Ren, W. J. Wang, X. B. Huang, K. L. Huang, Y. Wang, S. Q. Liu, *J. Power*

*Sources*, 2012, 199, 315–321.

[10] N. Sonoyama, Y. Suganuma, T. Kume, Z. Quan, *J. Power Sources*, 2011, 196, 6822–6827.

[11] S. Kurodaa, N. Taboria, M. Sakurabab, Y. Sato, *J. Power Sources*, 2003, 119–121, 924–928.

[12] A. Müller, J. Döring, M. I. Kham, V. Wittneben, *Angew. Chem. Int. Ed. Engl.*, 1991, 30, 210–212.



# Chapter 3

## Synthesis and Electrochemical Properties of Polyoxovanadate



### 3.1 Introduction

In this chapter, polyoxovanadate  $\text{K}_7[\text{MnV}_{13}\text{O}_{38}]$  (KMV), has been studied as cathode material of lithium battery. The structure of molecular cluster anion  $[\text{MnV}_{13}\text{O}_{38}]^{7-}$  and crystal structure of KMV are similar to that of KNV (Chapter 2) by substituting the central heteroatom Ni to Mn. Although nanosize particles show improvement in the discharge capacity, as discussed in Chapter 2, the cycle performance is not good for nanosize particles. This low cycle stability seems to be due to the dissolution of active material or decomposition of the electrolyte by the increased catalytic activity of POM at the high voltage range ( $>3.8$  V). In this Chapter, the electrochemical performance of KMV was investigated in detail and the effects of particle size and type of the conductive additive on the cycle performance of nanosize particles were analyzed. By using the mixture of nanosize particle and microsize particles as active material, the cycle performance of KMV was significantly improved. Electrochemical impedance spectroscopy (EIS) and *ex situ* transmission electron microscopy (TEM) measurement demonstrate that the formation of surface film on the cathode has important influence on the cycle performance of nanosize particles.

## 3.2 Experimental

### 3.2.1 Synthesis of Materials

#### *(1) Synthesis of KMV*

The synthesis of KMV was carried out as for the KNV shown in Chapter 2, substituting manganese sulfate for nickel sulfate. A solution of 7.18 g of  $\text{KVO}_3$  in 180 ml of hot distilled water was treated with 4 ml 1 M nitric acid, 4 ml of 1 M manganese sulfate, and 2.16 g of potassium peroxydisulfate, in that order. The mixture was kept at 80 °C and stirred and evaporated the solution and controlled the solution volume at 60 ml after 5 h, then filtered the hot solution as fast as possible. The filtrate was treated with 8 ml 1 M potassium acetate. After stirring overnight, the precipitate was filtered and washed with a little 0.5 M potassium acetate–0.5 M acetic acid, then washed with 4/1 (v/v) ethanol/water. To remove the water contained in powder, obtained powders were dried at 120 °C under air for 1h.

#### *(2) Synthesis of Nanosize Particles*

The preparation of nanosize KMV particles was also carried out as the preparation of nanosize KNV. The synthesis of nanosize KMV particles was carried out as follows: 0.2 g of as-prepared KMV powder was dissolved in 10 ml distilled water. The precipitate of re-crystallized KMV was immediately obtained by adding 50 ml ethanol to the solution. The re-crystallized particles were centrifuged, washed with acetone.

### 3.2.2 Characterization

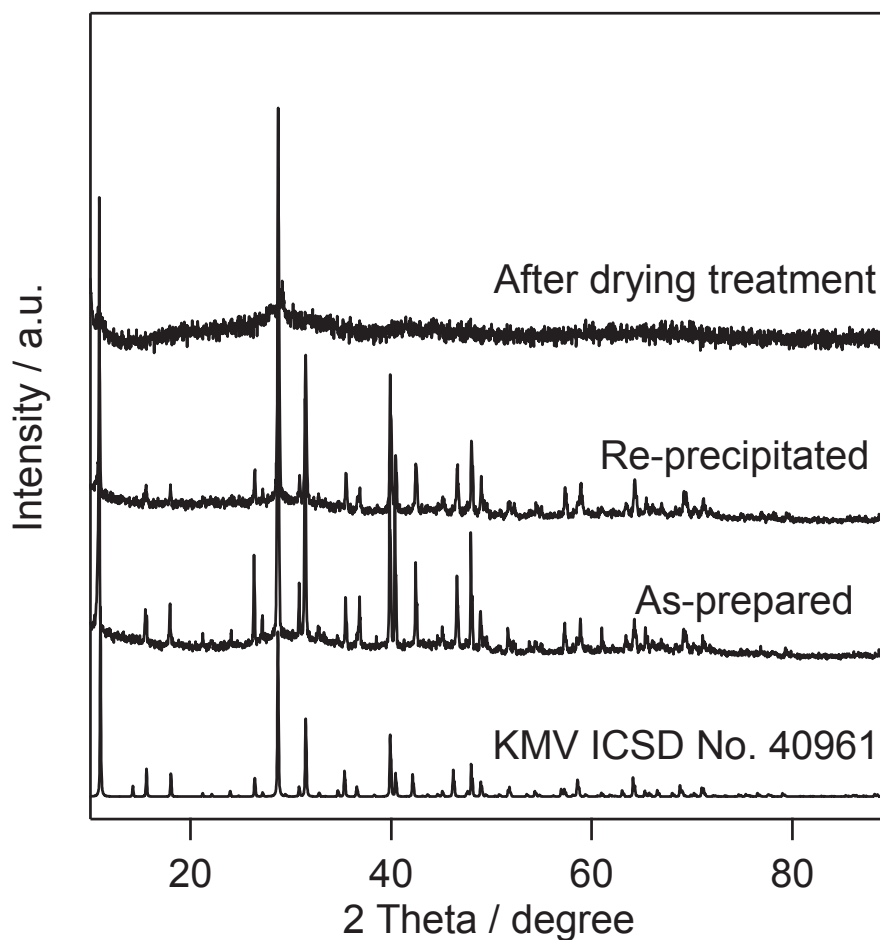
After discharge and charge of the cells, the cathode materials were removed from separable cells (Hosen HS cell) in Ar atmosphere glovebox, rinsed with dimethyl carbonate (Kishida battery grade) and dried in glovebox. A JEM-z2500 instrument operating at 200 kV accelerating voltage was used for *ex situ* transmission electron microscopy (TEM) analysis.

### 3.2.3 Electrochemical Measurements

The cathode consisted of KMV active material, AB or KB conductive additive and PTFE binder in the weight ratio of 48:48:4. The electrochemical properties of KMV electrode were tested at 25 °C by using CR-2032 coin cells, which were assembled in an argon filled glovebox using metallic lithium (Honjyo metal) as anode, and 1 M LiPF<sub>6</sub> in mixture of ethylene carbonate (EC) and diethyl carbonate (DEC) (3:7, v/v: Kishida battery grade) as the electrolyte solution. The discharge-charge properties of the cells were recorded on a battery tester (Interface model OZO-A19) between 1.5 and 4.2 V (vs. Li/Li<sup>+</sup>) at the current densities of 17 or 167 mA g<sup>-1</sup>. Solartron analytic instruments consisting of a frequency-response analyzer (Solartron 1255) and a potentiostat (Solartron 1280) were used to acquire electrochemical impedance spectroscopy (EIS) in the frequency range 10<sup>6</sup>–10<sup>-2</sup> Hz with an amplitude of 10 mV.

### 3.3 Results and Discussion

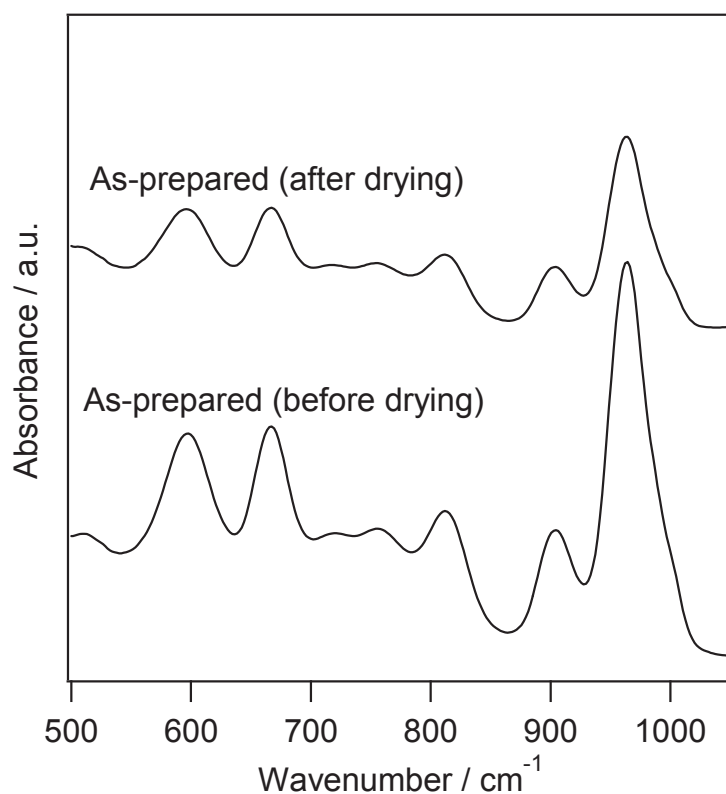
#### 3.3.1 Crystal and Molecular Structures



**Figure 3.1** XRD patterns of as-prepared KMV and re-precipitated KMV before drying and after drying.

The XRD patterns of as-prepared and re-precipitated KMV are shown in Figure 3.1. All of the reflections for as-prepared KMV agree well with those of KMV in ICSD No. 40961. The XRD pattern of re-precipitated KMV is consistent with that of as-prepared KMV, confirming the reappearance of KMV crystal structure by re-precipitation. Almost all of the reflections except the main peak at  $2\theta = 28.66^\circ$

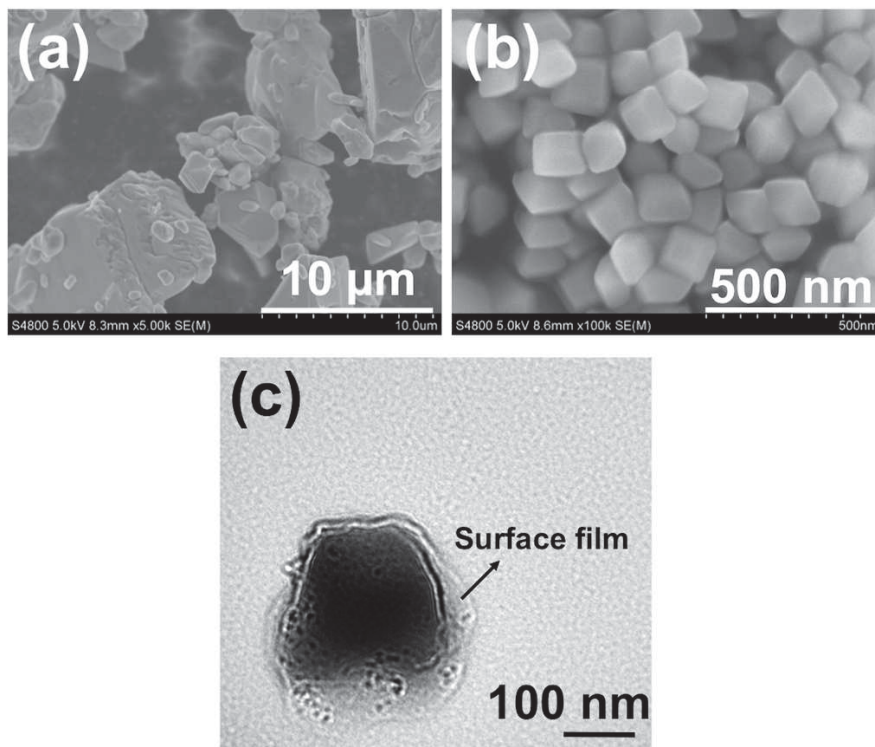
disappear after drying treatment, indicating that the crystal structure of KMV becomes amorphous, which should be caused by the removal of crystal water in KMV.



**Figure 3.2** FT-IR spectra of as-prepared KMV before drying and after drying.

FT-IR spectra were measured to confirm the structural stability of molecular cluster ion  $[\text{MnV}_{13}\text{O}_{38}]^{7-}$  after drying treatment, as shown in Figure 3.2. The characteristic absorbance peaks of dried KMV are consistent with those of KMV before drying in the wavenumber range between 500 and 1050  $\text{cm}^{-1}$ , demonstrating that the structure of molecular cluster ion  $[\text{MnV}_{13}\text{O}_{38}]^{7-}$  is maintained after drying treatment even the crystal structure changes to amorphous state.

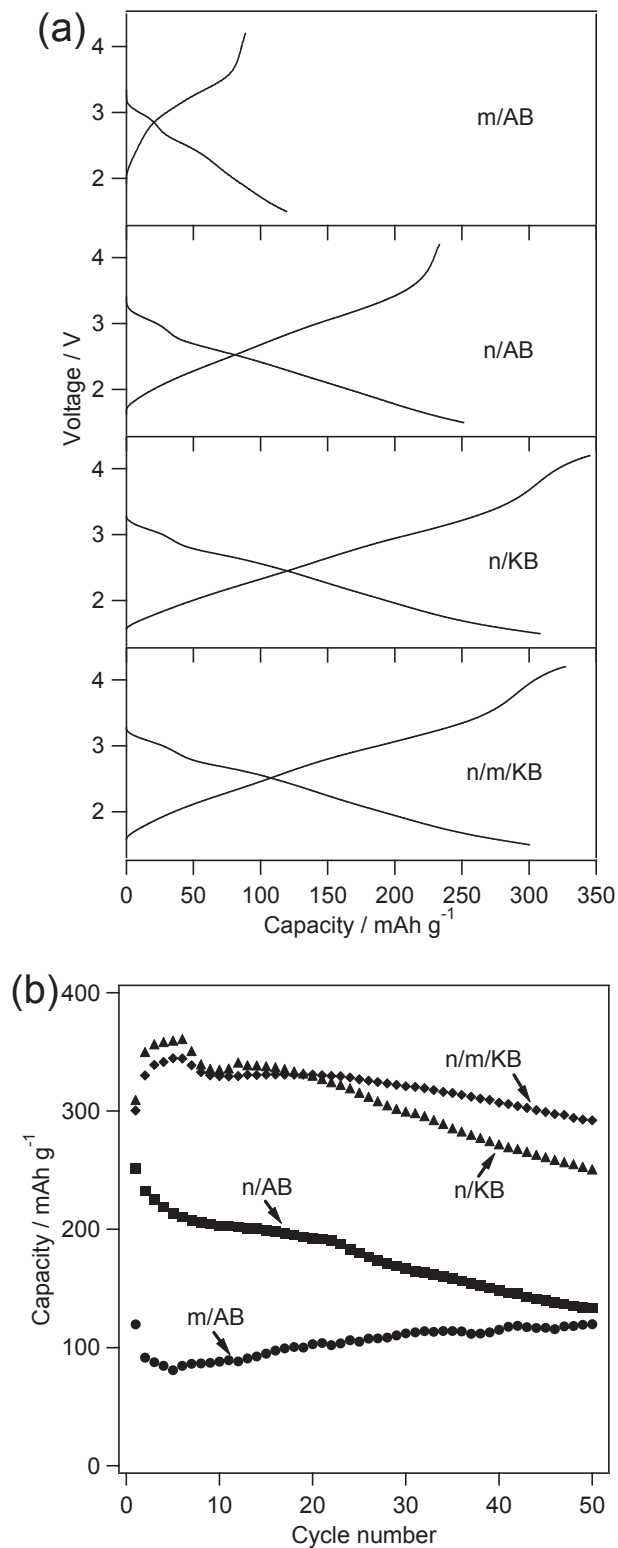
### 3.3.2 Crystal Morphology



**Figure 3.3** SEM images of (a) as-prepared KMV and (b) re-precipitated KMV, and (c) *ex situ* TEM image of n/KB after 20 cycles

The morphologies of as-prepared and re-precipitated crystals are shown in Figure 3.3a and b, respectively. It is clearly shown that the morphology of as-prepared crystal is very different from that of re-precipitated crystal. The as-prepared KMV is in large microsize particles, while the re-precipitated KMV shows cubic-like nanosize particles with regular geometric shape. The width and thickness of nanosize particles are as large as 150 nm, respectively.

### 3.3.3 Electrochemical properties



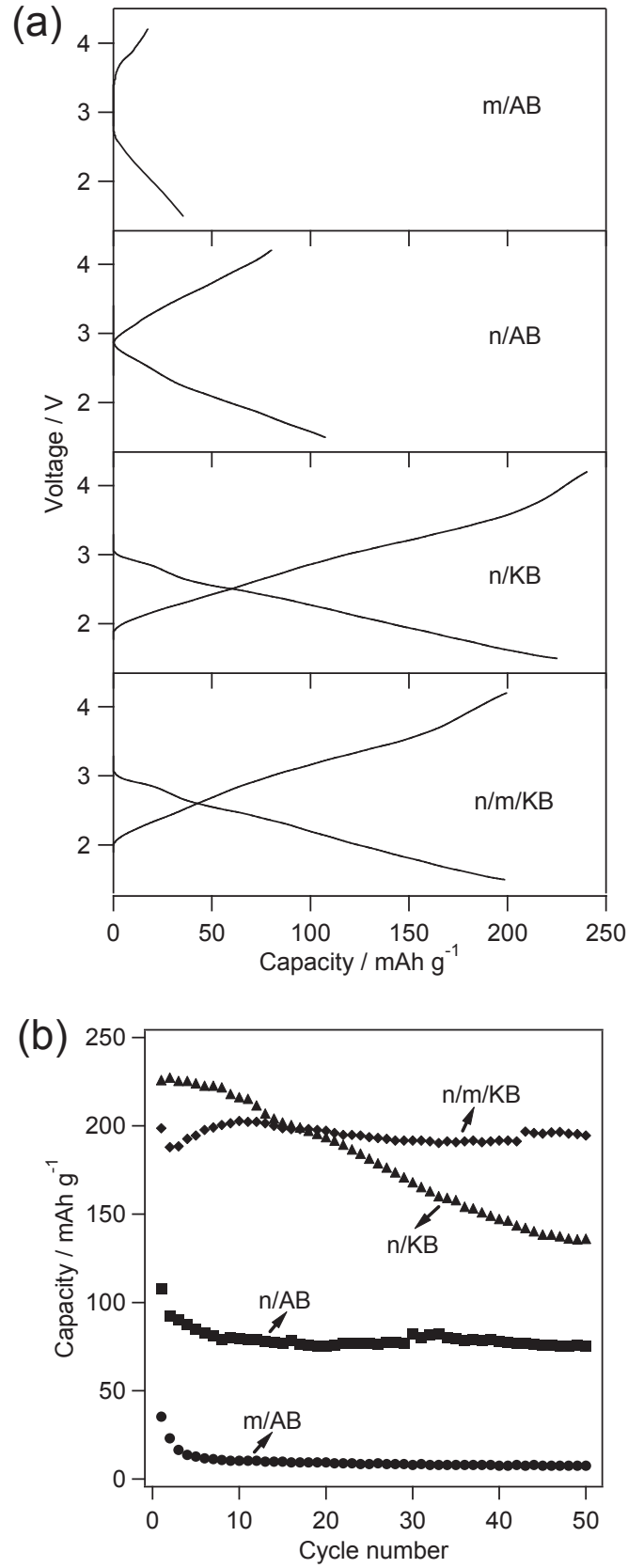
**Figure 3.4** (a) First discharge-charge curves and (b) cycle performance of KMV at the current density of 17 mA g<sup>-1</sup>.

Figure 3.4a shows the initial discharge-charge curves of KMV at the low current density of  $17 \text{ mA g}^{-1}$ . The microsize particles mixed with AB (m/AB) shows initial discharge capacity of  $120 \text{ mAh g}^{-1}$  and a very large polarization in the following charge process, resulting in an irreversible charge capacity of  $31 \text{ mAh g}^{-1}$ . Initial discharge capacity of KMV is improved to  $251 \text{ mAh g}^{-1}$  by mixing nanosize particles with AB (n/AB), which is more than two times as high as that of m/AB. It is noted that the polarization is also reduced in the following charge process and less irreversible charge capacity of  $18 \text{ mAh g}^{-1}$  is obtained for n/AB. The considerable improvement in the initial discharge capacity should be due to nanosize particles possess shorter diffusion path for lithium ions and larger specific surface area relative to microsize particles, which can improve the electric conductivity of KMV and facilitate the ionic and electronic transfer in the cathode. Due to the multi-electron redox that becomes possible in the discharge-charge process by using POMs as cathode materials [1, 2], much higher discharge capacity of KMV is expected to be obtained by mixing nanosize particles with the conductive additive with higher electric conductivity in comparison with the AB conductive additive. Hence, the KB with larger specific surface area was chosen as conductive additive because it has higher electric conductivity and larger surface area than that of AB [3]. As expected, the initial discharge capacity is further improved to  $308 \text{ mAh g}^{-1}$  by mixing nanosize particles with KB (n/KB). Nevertheless, n/KB shows overcharge behavior in the following charge process and exhibits an overcharge capacity of  $37 \text{ mAh g}^{-1}$  which

should be induced by the electrolyte decomposition. We speculate here that the uniform supply of electron by addition of KB may enhance the catalytic activity of nanosize KMV in the electrolyte oxidation during the charge process, resulting in the electrolyte decomposition in the contact interface of active mass-electrolyte. Such a decomposition of the electrolyte solution in the voltage region higher than  $\sim 3.8$  V will form a thick surface film on the cathode material and this film would impede the ionic and electronic transfer between the interface of cathode and electrolyte and harm the long-term cycle stability of the cell. In order to suppress the electrolyte decomposition, we explored the composite cathode consisting of a mixture of nanosize particles and microsize particles in the weight ration of 1:1 as active material and KB as conductive additive (n/m/KB). The partial substitution of nanosize particles by microsize particles is expected to reduce the catalytic activity of KMV in the electrolyte decomposition due to the lower contact surface area between the active material and the electrolyte. Initial discharge capacity of  $300 \text{ mAh g}^{-1}$  is obtained for n/m/KB, which is comparable to that of n/KB, and the overcharge capacity is decreased to  $27 \text{ mAh g}^{-1}$ . This indicates that the partial substitution of nanosize particles by microsize particles reduces the irreversible capacity to a certain extent without losing the electrochemical property.

The cycle performance of KMV after 50 cycles at the current density of  $17 \text{ mA g}^{-1}$  is shown in Figure 3.4b. The capacity of m/AB slightly increases with cycling after the first 10 cycles and tends to be stable after the 30th cycle. After 50 cycles, almost 100% capacity retention is retained, indicating that the as-prepared microsize particles

have high capacity retention with long-term cycling. Although n/AB shows higher discharge capacity than that of m/AB, the capacity decreases drastically with the increase of cycle number. After 50 cycles, capacity of  $133 \text{ mAh g}^{-1}$  is obtained, and the capacity retention is only 53%. On the other hand, n/KB shows not only much higher discharge capacity but also better cycle performance compared to n/AB, though the capacity fade is evident after the 20th cycle. After 50 cycles, capacity of  $249 \text{ mAh g}^{-1}$  is obtained and capacity retention is 81% for n/KB, which are much higher than that of n/AB. Furthermore, n/m/KB shows much better cycle performance in comparison with n/KB, capacity of  $292 \text{ mAh g}^{-1}$  corresponding to capacity retention of 97.3% is obtained after 50 cycles.



**Figure 3.5** (a) First discharge-charge curves and (b) cycle performance of KMV at the current density of 167 mA g<sup>-1</sup>.

To investigate the rate performance of KMV as cathode material, the cells were cycled at the higher current density. Figure 3.5a shows the first discharge-charge curves of the different cathodes with the current density of  $167 \text{ mA g}^{-1}$ . Significant loss of the initial discharge capacities occurs at the high rate compared to the cathodes with the low rate, due to the increase of polarization [4]. Initial discharge capacity of only  $35 \text{ mAh g}^{-1}$  is obtained for m/AB and very large overpotential appears in the following charge process, indicating the very poor electric conductivity of the cathode consisting of large microsize particles as an active material and AB as a conductive additive. Initial discharge capacities of 108, 225 and  $199 \text{ mAh g}^{-1}$  are obtained for n/AB, n/KB and n/m/KB, respectively. It should be noted that, similar to the cathode cycled at the low current density of  $17 \text{ mA g}^{-1}$ , n/KB still shows the overcharge behavior at the voltage higher than  $\sim 3.8 \text{ V}$  with an overcharge capacity of  $15 \text{ mAh g}^{-1}$ . However, this overcharge behavior is almost eliminated by n/m/KB, and almost reversible capacity of  $200 \text{ mAh g}^{-1}$  is obtained in the charge process. Figure 3.5b shows the cycle performance of the different cathodes at the current density of  $167 \text{ mA g}^{-1}$ . After 50 cycles, very low discharge capacity of  $8 \text{ mAh g}^{-1}$  is obtained for m/AB, while n/AB retains discharge capacity of  $75 \text{ mAh g}^{-1}$  corresponding to the capacity retention of 69%, which is higher than that of n/AB cycled at the low current density of  $17 \text{ mA g}^{-1}$ . J. C. Arrebola et al. also reported the similar cycle performance of the nanosize particles of the spinel  $\text{LiNi}_{0.5}\text{Mn}_{1.5}\text{O}_4$  cathode [5], in which the capacity retention at the high rate is good, but drastically decreases at the low rate. They supposed that the poor cycle performance at the low rate is probably caused by

the dissolution of nanosize particles into the electrolyte because of the large contact surface area between nanosize particles and electrolyte. Although n/KB shows higher capacity than n/AB, the capacity loss becomes more notable than it is cycled at the low rate: capacity retention after 50 cycles for n/KB is 60%, while that for n/AB was 70%. For the case of n/m/KB, the capacity at the high rate reduces compared with that at the low rate due to the increase of polarization, but the cycle stability is still good with capacity retention of 97.5% after 50 cycles.

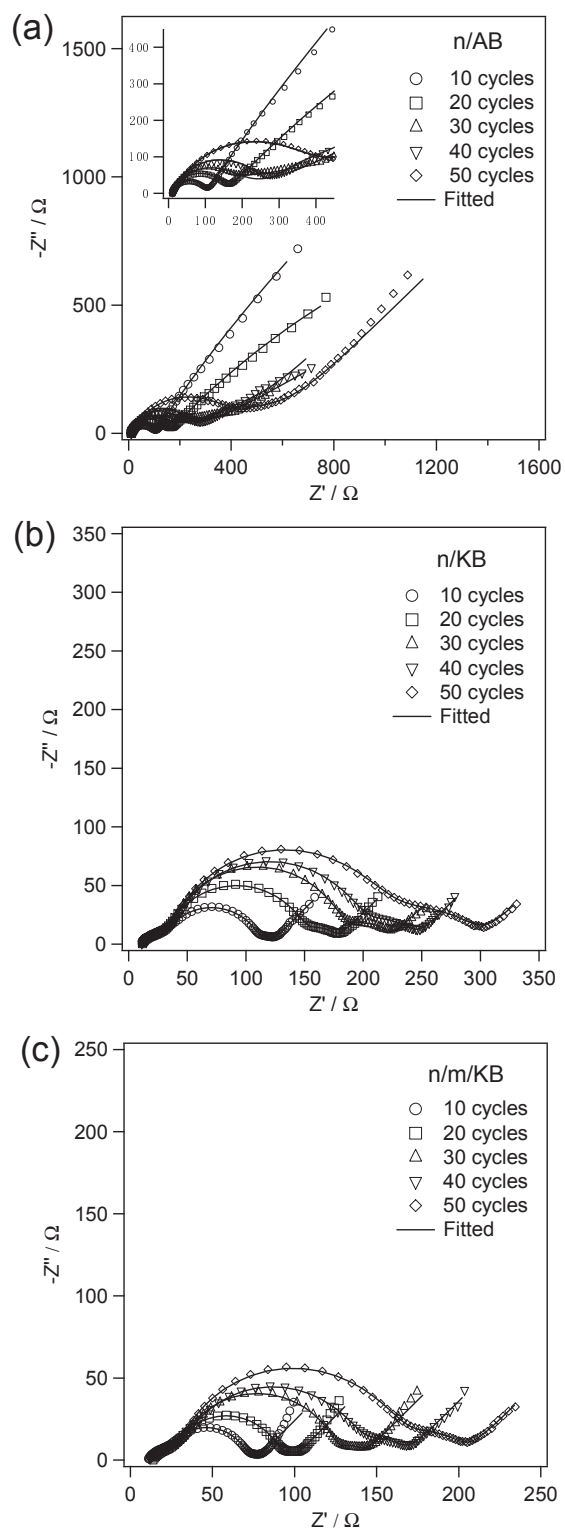


**Figure 3.6** Nyquist plots of (a)  $n/AB$  (inset: Enlargement of the semicircles), (b)  $n/KB$  and (c)  $n/m/KB$  recorded at the variable cycle number with the current density of  $17 \text{ mA g}^{-1}$ . The symbols and the lines represent experimental data and fitted data, respectively.

To analyze how nanosize particles and type of conductive additives (AB and KB) affect the cycle performance of KMV at the low rate (current density of  $17 \text{ mA g}^{-1}$ ), EIS measurements were recorded for the cells cycled after a variable cycle number. Figure 3.6 shows the Nyquist plots of the cells cycled at the low current density of  $17 \text{ mA g}^{-1}$ . It can be seen that the impedance behavior of n/AB (Figure 3.6a) is quite different from those of n/KB (Figure 3.6b) and n/m/KB (Figure 3.6c). The Nyquist plots of n/AB contain only one semicircle in high-frequency range (1000–10 kHz) and a slope line in low-frequency range (10–0.01 kHz). The Nyquist plots of n/KB and n/m/KB show similar characteristic with the increase of cycle number, consisting of three semicircles in high-frequency range (1000–10 kHz), medium-frequency range (10 kHz–10 Hz) and low-frequency range (10–0.5 Hz), respectively, and a slope lines in the lowest-frequency range (0.5–0.01 Hz). According to previously reported papers [6-12], the impedance behavior of KMV cathode should be assigned to the different processes as follows. For n/AB, the semicircles in high-frequency range should be due to the charge-transfer resistance between cathode and electrolyte, the slope lines in the low frequency range are associated to solid-state diffusion of lithium ion in the active material (Warburg-type impedance). For n/KB and n/m/KB, the semicircles in high-frequency range (1000–10 kHz) would be attributed to solid electrolyte interface (SEI) on the surface of the anode lithium metal, because its small radii are almost independent from the cycle number. The other two semicircles in medium-frequency range (10 kHz–10 Hz) and low-frequency range (10–0.5 Hz), which are strongly dependent on the cycle number, would be attributable to the

resistances for charge-transfer of cathode material and the surface film on the cathode material which originates from the decomposed species of electrolyte in the charge process, respectively [8]. The slope lines observed in the lowest-frequency range (0.5–0.01 Hz), as well as that of  $n/AB$  appearing in the low frequency of 10–0.01 Hz, are also related to the solid-state diffusion of lithium ion in the cathode.

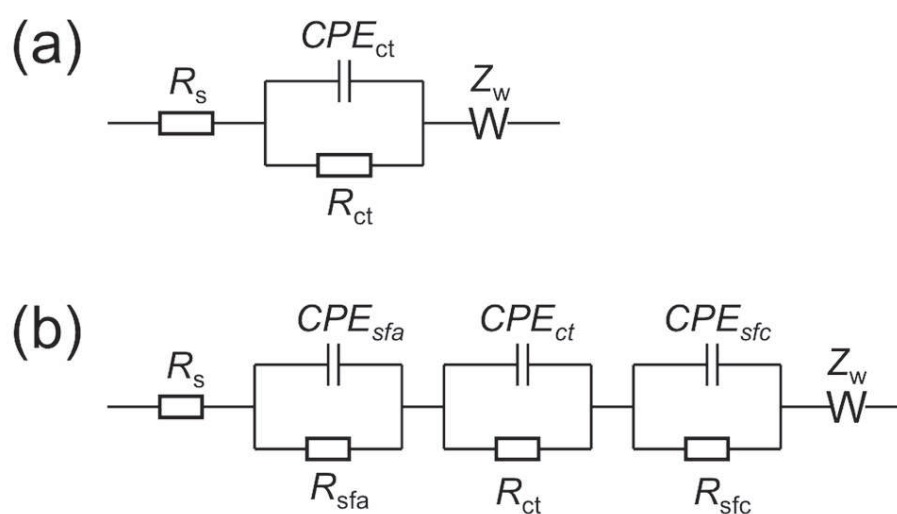


**Figure 3.7** Equivalent circuits proposed for fitting the obtained Nyquist plots.

The equivalent circuits proposed to fit the two different impedance behaviors are shown in Figure 3.7a and b, respectively.  $R_s$  is the electrolyte resistance;  $R_{sfa}$  is the resistance of the surface film on the anode;  $R_{ct}$  is the charge-transfer resistance;  $R_{sfc}$  is the resistance of the surface film on the cathode;  $CPE_{sfa}$ ,  $CPE_{ct}$  and  $CPE_{sfc}$  are the constant phase elements, and  $Z_w$  is the Warburg impedance.

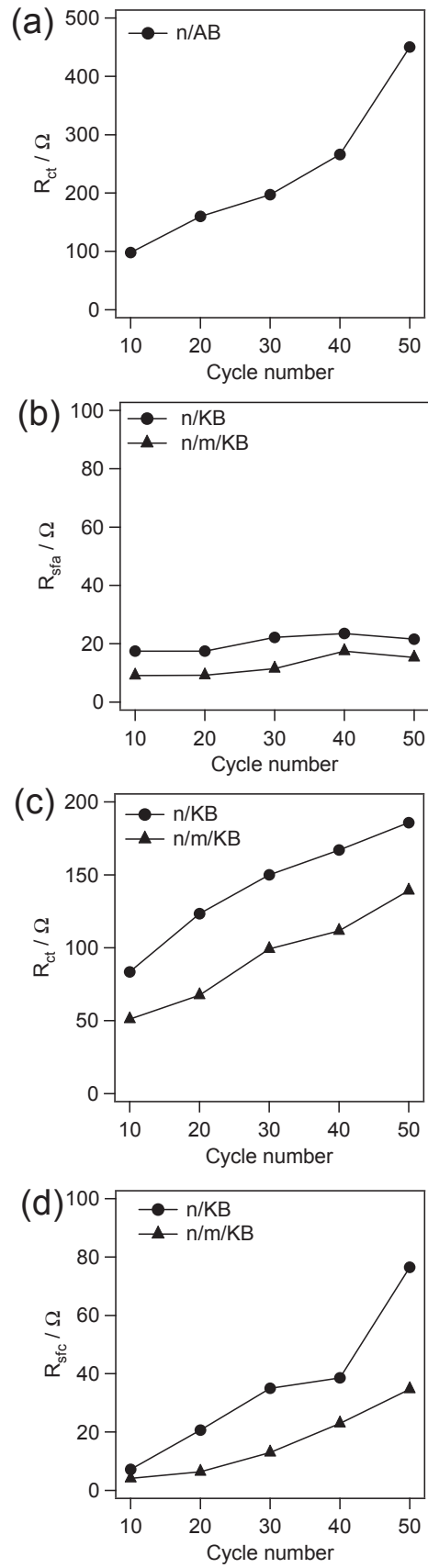


**Figure 3.8** The dependence of the fitted impedance parameters for (a)  $R_{ct}$ , (b)  $R_{sfa}$ , (c)  $R_{ct}$  and (d)

$R_{sfc}$  on the cycle number.

The fitted data for the various parameters are plotted in Figure 3.8. In light of these EIS results, the following analysis for the different cycle performance of KMV affected by particle size and type of conductive additive are given. Figure 3.8a shows that the  $R_{ct}$  of n/AB increases drastically with the increase of cycle number. It is speculated that this is likely caused by the dissolution of partial nanosize particles into the electrolyte in the reduction/oxidation state at the low current density of  $17 \text{ mA g}^{-1}$  [5,13]. Higher surface area of the active material would be exposed to the electrolyte by decreasing the particle size to nanoscale, which might increase the solubility of KMV in the organic electrolyte during the discharge-charge process, resulting in the loss of active material and increase of resistances for electrode reactions. Thus, the poor cycle performance of n/AB in the fast capacity loss (Figure 3.4b) should result mainly from the continuous loss of nanoscale active material with the increase of cycle number. However, the dissolution of nanosize particles into the electrolyte might be reduced when n/AB is cycled at the higher rate ( $167 \text{ mA g}^{-1}$ ) (Figure 3.5b) due to the shorter exposed time of the reduced/oxidized KMV towards to the electrolyte, resulting in relatively high capacity retention with long-term cycling. KB conductive additive with high electric conductivity has been reported to show better effects than AB in improving the electrochemical performance of cathode materials [3,14]. However, it should be noted that the higher capacity retention of n/KB relative to that of n/AB at the low rate should not only be due to the increased electric conductivity by addition of KB conductive additive. Some other factors, which would prevent the dissolution of nanosize particles, should also be responsible for the

relative stable cycle performance of n/KB. As expected, in light of the Nyquist plots shown in Figure 3.6b, and the *ex situ* TEM image shown in Figure 3.3c demonstrate that addition of KB conductive additive promotes the formation of surface film on the cathode, which can reduce the direct contact surface area between the electrolyte and the nanosize particles, protecting the active material from dissolving into the electrolyte during the discharge-charge process. As the overcharge behavior discussed above, the surface film should originate from the decomposed species of the electrolyte in the charge process due to the increased catalytic activity of nanosize KMV in the electrolyte by addition of KB. Therefore, the improvement in capacity and capacity retention of nanosize particles mixed with KB should be ascribed to the following two factors. One is the improved electric conductivity by addition of KB conductive additive. The other is the formation of protective surface film on nanosize particles, preventing the dissolution of active material. Nevertheless, the resistances ( $R_{ct}$  and  $R_{sfc}$ ) for charge-transfer and surface film in n/KB are much higher than those of n/m/KB, indicating that there should be thicker surface film on n/KB relative to n/m/KB. Thus, n/KB shows more and more noticeable capacity loss with long-term cycling (Figure 3.4b) due to the larger increase in electrode reaction resistances. In addition, by combination with KB conductive additive, the microsize particles might show lower catalytic activity towards the electrolyte compared to the nanosize particles, because there is lower contact surface area between the KMV active material and the electrolyte for n/m/KB. This would decrease the electrolyte decomposition, as illustrated by the reduced overcharge behavior in Figure 3.4a. Thus,

the more stable cycle performance and higher capacity retention of n/m/KB, in comparison with n/KB, should be ascribed to the formation of relative thinner surface film, which not only effectively prevent the nanosize particles dissolution, but also assure the transfer of lithium ions and electrons favorably. It should be noted that the resistance of surface film ( $R_{\text{sfa}}$ ) on anode is low and almost constant during the discharge-charge cycles in both n/KB and n/m/KB, indicating that this film does not influence the cycle stability of the cell.

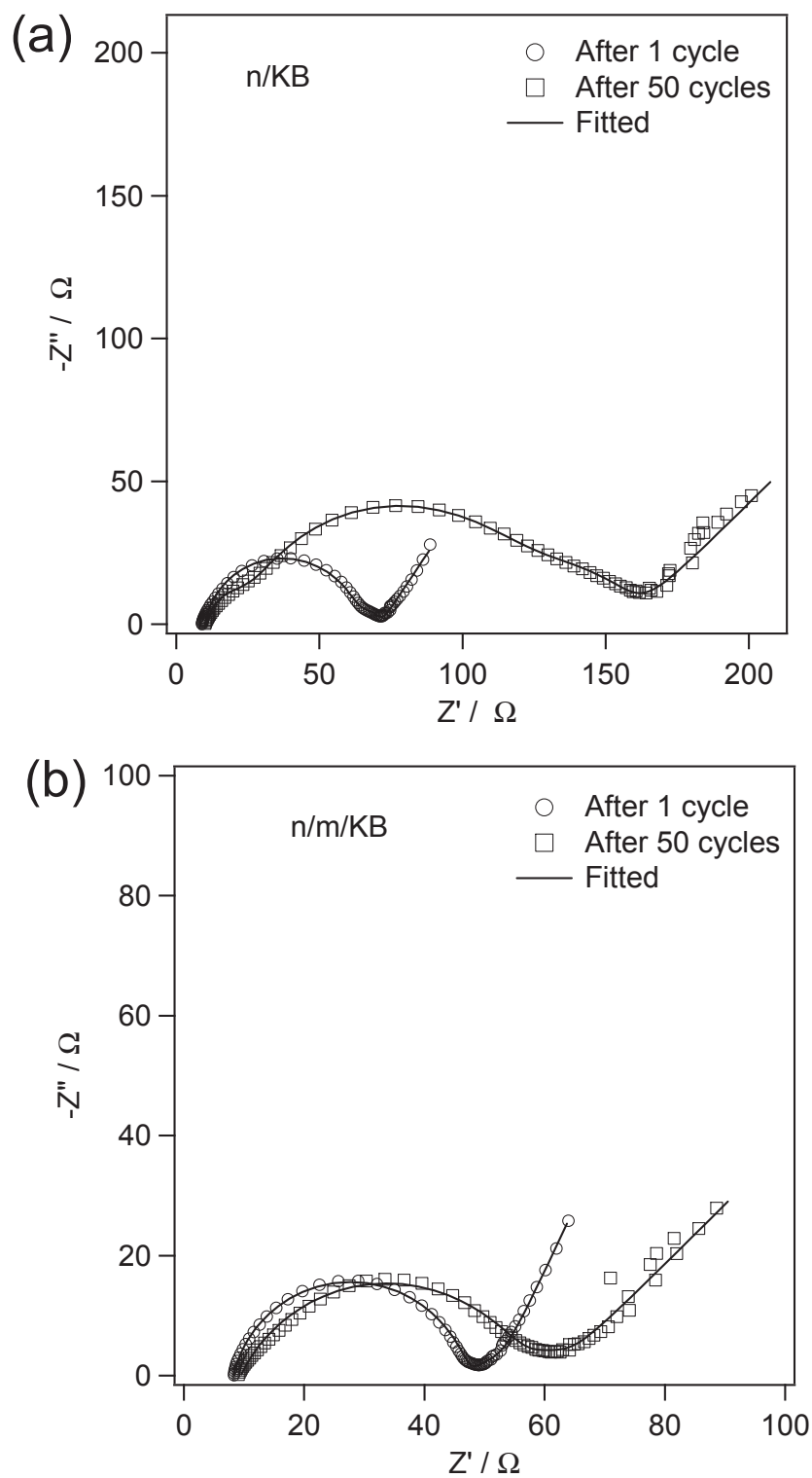


**Figure 3.9** Nyquist plots of (a)  $n/KB$  and (d)  $n/m/KB$  recorded after one cycle and 50 cycles with the current density of  $167 \text{ mA g}^{-1}$ . The symbols and the lines represent experimental data and fitted data, respectively.

To analyze the different cycle performance between n/KB and n/m/KB cycled at the high rate, Nyquist plots after 1 cycle and 50 cycles were recorded at the current density of  $167 \text{ mA g}^{-1}$ , as shown in Figure 3.9. After one cycle, both n/KB and n/m/KB show similar impedance behavior, the Nyquist plots consist of one high-frequency (1000 kHz–10 Hz) semicircle and a slope line in the low frequency (10 Hz–0.01 Hz). Nevertheless, after 50 cycles, the impedance behavior of n/KB becomes distinctly different from that of the first cycle, while the impedance behavior of n/m/KB does not change. It is noted that the Nyquist plot of n/KB after 50 cycles is very similar to that of it cycled at the low current density of  $17 \text{ mA g}^{-1}$ , consisting of three semicircles in high-frequency (1000–10 kHz), medium-frequency (10 kHz–10 Hz) and low-frequency (10–0.5 Hz), respectively, and a slope line in lowest-frequency (0.5–0.01 Hz). This indicates that when cycling at the high rate the surface film also forms on n/KB, but without forming on n/m/KB. The Nyquist plots for n/KB after one cycle and n/m/KB after one cycle and 50 cycles were fitted by the equivalent circuit shown in Figure 3.7a, while the equivalent circuit shown in Figure 3.7b was used to fit the Nyquist plot of n/KB after 50 cycles. For n/KB, the  $R_{ct}$  after one cycle is  $58 \ \Omega$ , while the  $R_{sfa}$ ,  $R_{ct}$  and  $R_{sfc}$  after 50 cycles are 13.4, 96.4 and  $37.6 \ \Omega$ , respectively. The  $R_{ct}$  of n/m/KB after one cycle is  $39 \ \Omega$ , which is close to the  $R_{ct}$  of  $47.7 \ \Omega$  after 50 cycles, indicating that the partial substitution of nanosize particles by microsize particles almost does not increase the resistance of electrode reaction. Herein, it is suggested that the formation of surface film at the high rate is particularly undesirable as the film would give rise to much more impediment for the transfer of

lithium ions and electrons [4]. As shown in Figure 3.5b, n/KB with high resistive surface film shows dramatically capacity loss with the increase of cycle number, whereas n/m/KB without formation of surface film shows very stable cycle performance with high capacity retention.

### 3.3.4 Discharge-Charge Reaction Mechanism

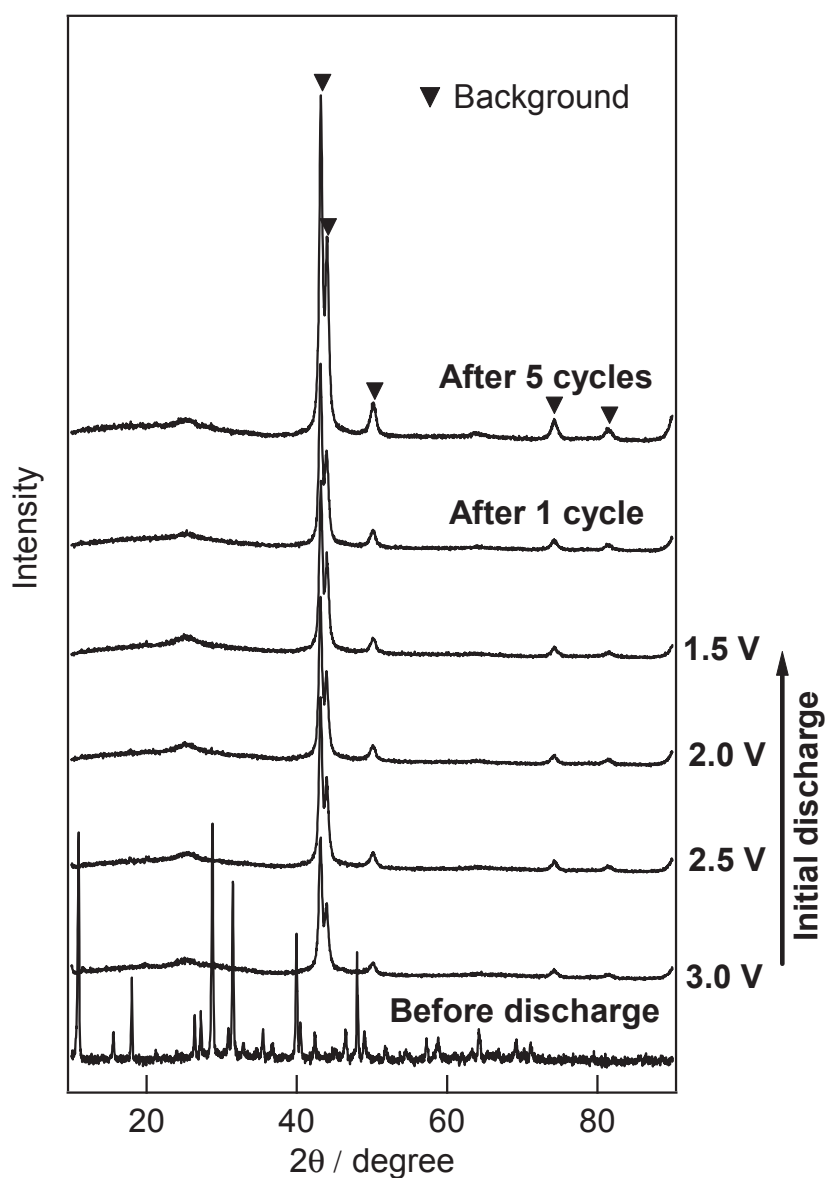


**Figure 3.10** *Ex situ* XRD patterns of KMV cathode recorded at different voltages in the first discharge process, after one cycle and after five cycles.

To investigate the discharge-charge reaction mechanism of KMV as cathode material of lithium battery, *ex situ* XRD patterns were recorded to study the change of crystal structure during discharge-charge process, as shown in Figure 3.10. The sample before drying was used as the control because the KMV is easy to become amorphous after drying treatment. It can be seen that when initially discharged to 3.0 V, all of the reflections disappear, indicating that the structure of KMV changes to amorphous with the insertion of lithium ion. The amorphous structure is maintained till the end of discharge at 1.5 V. In the following recharge process, the structure shows irreversibility and is still in the amorphous state even after 5 cycles. This demonstrates that the insertion-extraction of lithium can continuously proceed in amorphous KMV during the discharge-charge process, which is independent from the crystal structure.

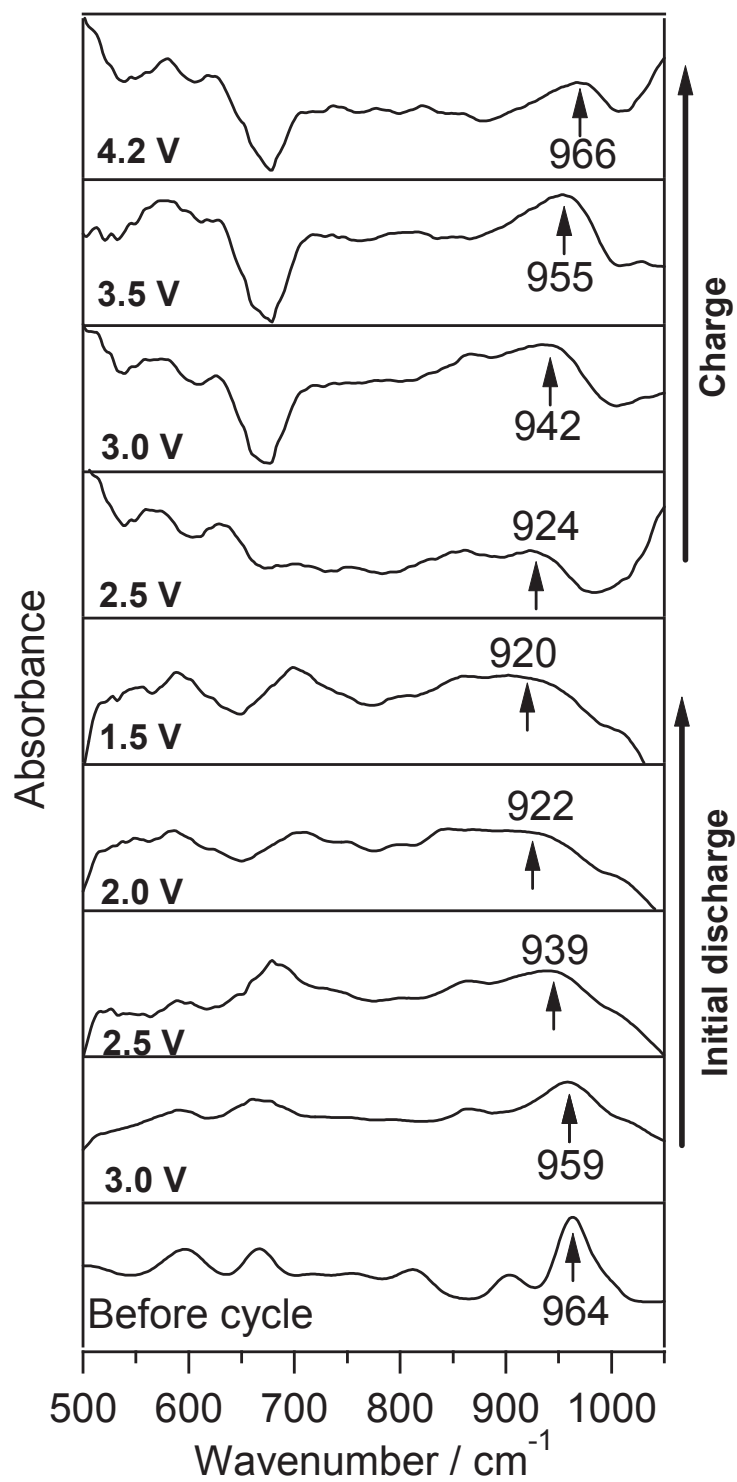


**Figure 3.11** *Ex situ* FT-IR spectra of KMV cathode recorded at different voltages in the first discharge and charge process.

The structural change of molecular cluster ion  $[\text{MnV}_{13}\text{O}_{38}]^{7-}$  during the

discharge-charge process was investigated by *ex situ* FT-IR spectra, as shown in Figure 3.11. The characteristic absorbance peak of the sample before cycle at the wavenumber of  $964\text{ cm}^{-1}$  corresponds to the stretching vibration of terminal V-O bond in molecular structure of  $[\text{MnV}_{13}\text{O}_{38}]^{7-}$  [15]. It is clearly shown that the absorbance peak shifts gradually to lower wavenumber in the first discharge process. In the following charge process, the absorbance peak shows reversibility and gradually shifts back to higher wavenumber. At the end of charge to the voltage of 4.2 V, the absorbance peak gets back to the wavenumber of  $966\text{ cm}^{-1}$ , which is almost the same as the original position of the sample before discharge. The red shift of the V-O bond vibration towards to the lower wavenumber would correspond to the reduction of vanadium ion in the discharge-charge process, because it is reasonable that V-O bond stretching energy decreases with the reduction of vanadium ion for the decrease of electrostatic interaction between vanadium ion and oxide ion. The reversible shift of the V-O bond stretching vibration indicates that the structure of the molecular cluster ion  $[\text{MnV}_{13}\text{O}_{38}]^{7-}$  is stable and reacts reversibly with lithium ion during the discharge-charge process.

The results of *ex situ* XRD and *ex situ* FT-IR demonstrate that the discharge-charge reaction mechanism of the KMV as cathode material of lithium ion battery is the same as the KNV discussed in Chapter 2. The discharge-charge process can also continuously proceed in amorphous KMV, which is independent from the recoverability of crystal structure, and the lithium ion can react reversibly with the molecular cluster ion  $[\text{MnV}_{13}\text{O}_{38}]^{7-}$ .

### 3.4 Conclusions

The polyoxovanadate KMV in nanosize particle shows much higher discharge capacity than that of the as-prepared microsize particles. KB conductive additive shows better effect than AB in improving discharge capacity and cycle stability of nanosize particles at the low current density of  $17 \text{ mA g}^{-1}$ . The cathode consisting of the mixture of nanosize particles with microsize particles in the weight ration of 1:1 as active material and KB as conductive additive shows very stable cycle performance with high capacity retention over 97 % after 50 cycles. The discharge-charge process of KMV is independent from its crystal structure and lithium ion reacts with the molecular cluster ion reversibly.

## References

- [1] N. Sonoyama, Y. Sukanuma, T. Kume, Z. Quan, *J. Power Sources*, 2011, 196, 6822–6827.
- [2] S. Uematsu, Z. Quan, Y. Sukanuma, N. Sonoyama, *J. Power Sources*, 2012, 217, 13–20.
- [3] S. Kurodaa, N. Toboria, M. Sakurabab, Y. Sato, *J. Power Sources*, 2003, 119–121, 924–928.
- [4] J. B. Goodenough, Y. Kim, *Chem. Mater.*, 2010, 22, 587–603.
- [5] J. C. Arrebola, A. Caballero, L. Hernán, J. Morales, *Electrochem. Solid-State Lett.*, 2005, 8, A641–A645.
- [6] M. D. Levi, G. Salitra, B. Markovsky, H. Teller, D. Aurbach, U. Heider, L. Heiderb, *J. Electrochem. Soc.*, 1999, 164, 1279–1289.
- [7] M. D. Levi, D. Aurbach, *J. Phys. Chem. B*, 1997, 101, 4630–4640.
- [8] D. Aurbach, *J. Power Sources*, 2000, 89, 206–218.
- [9] D. Aurbach, K. Gamolsky, B. Markovsky, G. Salitra, Y. Gofer, U. Heider, R. Oesten, M. Schmidt, *J. Electrochem. Soc.*, 2000, 147, 1322–1331.
- [10] Z. Li, F. Du, X. Bie, Dong Zhang, Y. Cai, X. Cui, C. Wang, *J. Phys. Chem. C*, 2010, 114, 22751–22757.
- [11] J. P. Zheng, D. J. Crain, D. Roy, *Solid State Ionics*, 2011, 196, 48–58.
- [12] J. P. Schmidt, T. Chrobak, M. Ender, J. Illig, D. Klotz, E. Ivers-Tiffée, *J. Power Sources*, 2010, 196, 5342–5348.
- [13] D. H. Jang, Y. J. Shin, S. M. Oh, *J. Electrochem. Soc.*, 1996, 143, 2204–2211.
- [14] Z. Bakenov, I. Taniguchi, *J. Power Sources*, 2010, 195, 7445–7451.
- [15] A. Müller, J. Döring, M. I. Kham, V. Wittneben, *Angew. Chem. Int. Ed. Engl.*, 1991, 30,

210-212.



# Chapter 4

## Synthesis and Electrochemical Properties of Polyoxomolybdate



### 4.1 Introduction

In this chapter, the polyoxomolybdate  $(\text{NH}_4)_6[\text{NiMo}_9\text{O}_{32}]$  (ANM) has been studied as cathode material of lithium battery. Figure 4.1 shows the structure of molecular cluster ion  $[\text{NiMo}_9\text{O}_{32}]^{6-}$  and crystal structure of ANM [1, 2]. The molecular cluster ion  $[\text{NiMo}_9\text{O}_{32}]^{6-}$  consists of three levels octahedra groups. As shown in Figure 4.1a and b, the upper-level and low-level are groups of three  $\text{MoO}_6$  octahedra, each octahedron in the group shares two adjacent edges with the others two octahedra. In the middle-level, each of the three  $\text{MoO}_6$  octahedra shares one of their edges with three non-adjacent edges of the central  $\text{NiO}_6$  octahedron. This molecular structure formed by edge-sharing of the ten octahedra is expected to show good stability due to the strong covalent binding. Therefore, ANM could be a promising candidate of POMs as cathode material of lithium battery because of its potential stable structure for molecular cluster ion  $[\text{NiMo}_9\text{O}_{32}]^{6-}$ .

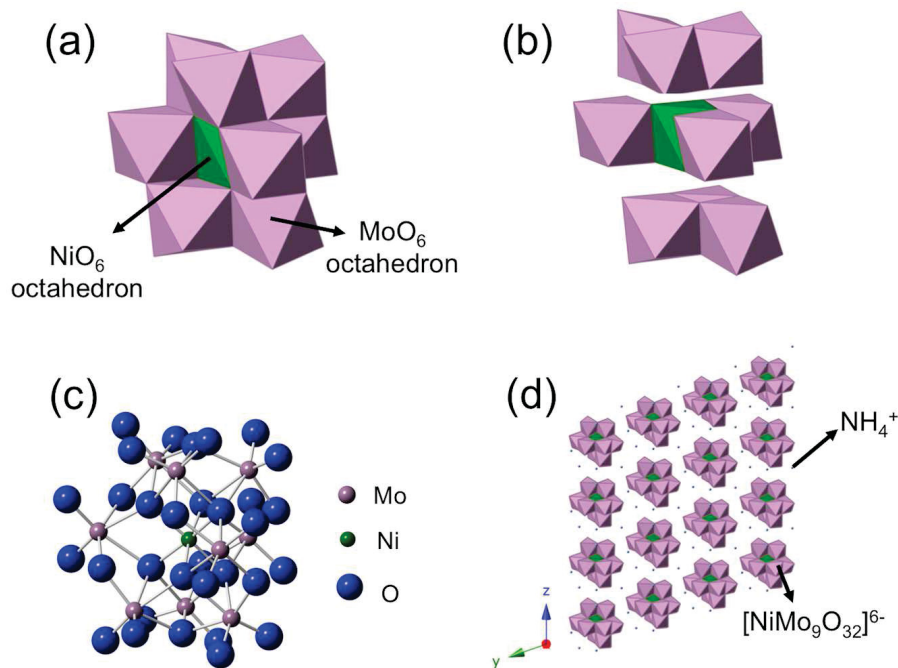


**Figure 4.1** Polyhedral representation for the structure of molecular cluster ion  $[\text{NiMo}_9\text{O}_{32}]^{6-}$ : (a) the structure as a whole and (b) an exploded view of the structure; (c) ball-and-stick representation for structure of molecular cluster ion  $[\text{NiMo}_9\text{O}_{32}]^{6-}$ ; (d) crystal structure of ANM.

## 4.2 Experimental

### 4.2.1 Synthesis of Materials

#### (1) Synthesis of ANM

The synthesis of ANM was carried out by a modification of the reported method [3]. The detailed synthesis procedures are as follows. 4.37 g  $(\text{NH}_4)_6\text{Mo}_7\text{O}_{24}\cdot 4\text{H}_2\text{O}$  (Wako, GR) dissolved in 25 ml distilled water and heated to 95 °C, then a 25 ml solution containing 0.66 g  $\text{NiSO}_4\cdot 6\text{H}_2\text{O}$  (Wako, GR) and 0.8 g  $(\text{NH}_4)_2\text{S}_2\text{O}_8$  (Kishida, GR) was added to the hot solution. The mixture was boiled and stirred for 5 min, then filtered the hot solution quickly. Black product precipitated out after cooling the filtrate with stirring for 1h. The precipitate was filtered and washed with 50 ml 1:1 v/v

acetone-distilled water. To remove the water contained in the products, all of the as-prepared samples were dried at 120 °C under air for 1h.

### *(2) Synthesis of Nanosize Particles*

To synthesis the nanosize ANM particles, 0.15 g as-prepared ANM powders were dissolved in 10 ml distilled water. The re-precipitated ANM particles were immediately obtained by adding 50 ml ethanol to the solution, followed with centrifugation and washed with acetone.

### *(3) Synthesis of Nanocomposite ANM/KB*

For the preparation of nanocomposite ANM/KB (ANM *in situ* re-crystallized in the micropores or mesopores of KB matrix), 0.6 g KB powders were added to the 20 ml solution containing 0.318 g (to obtain the weight ratio of ANM /KB=2/1 for electrode fabrication, the water loss of 5.5% for ANM after drying treatment is calculated) dissolved as-prepared ANM powders, followed with ultrasonic dispersion for 30 min, then added 100 ml ethanol to the mixture, and filtered and washed the product with acetone.

## **4.2.2 Characterization**

Raman spectra were recorded with a Laser Raman Spectrometer (JASCO NRS-3300) in the energy range 250–1050  $\text{cm}^{-1}$  with the probe light of Raman scattering, DPSS laser at a wavelength of 532 nm was used. A JEM-z2500 instrument

operating at 200 kV accelerating voltage was used for transmission electron microscopy (TEM) analysis, and elemental mappings were obtained by scanning transmission electron microscopy (STEM) equipped with energy dispersive X-ray analysis (EDX) analyzer.

#### **4.2.3 Electrochemical Measurements**

Unless otherwise noted, the cathode consisted of ANM active material, AB or KB conductive additive and PTFE binder in the weight ratio of 32:64:4. The electrochemical properties of ANM electrode were tested at 25 °C by using CR-2032 coin cells, which were assembled in an argon filled glovebox using metallic lithium (Honjyo metal) as anode, and 1 M LiPF<sub>6</sub> in mixture of ethylene carbonate (EC) and diethyl carbonate (DEC) (3:7, v/v: Kishida battery grade) as the electrolyte solution. The discharge-charge properties of the cells were recorded on a battery tester (Interface model OZO-A19) between 1.5 and 4.2 V (vs. Li/Li<sup>+</sup>) at the current densities from 17 to 500 mA g<sup>-1</sup>. Solartron analytic instruments consisting of a frequency-response analyzer (Solartron 1255) and a potentiostat (Solartron 1280) were used to acquire electrochemical impedance spectroscopy (EIS) in the frequency range 10<sup>6</sup>–10<sup>-2</sup> Hz with an amplitude of 10 mV.

## 4.3 Results and Discussion

### 4.3.1 Crystal and Molecular Structures

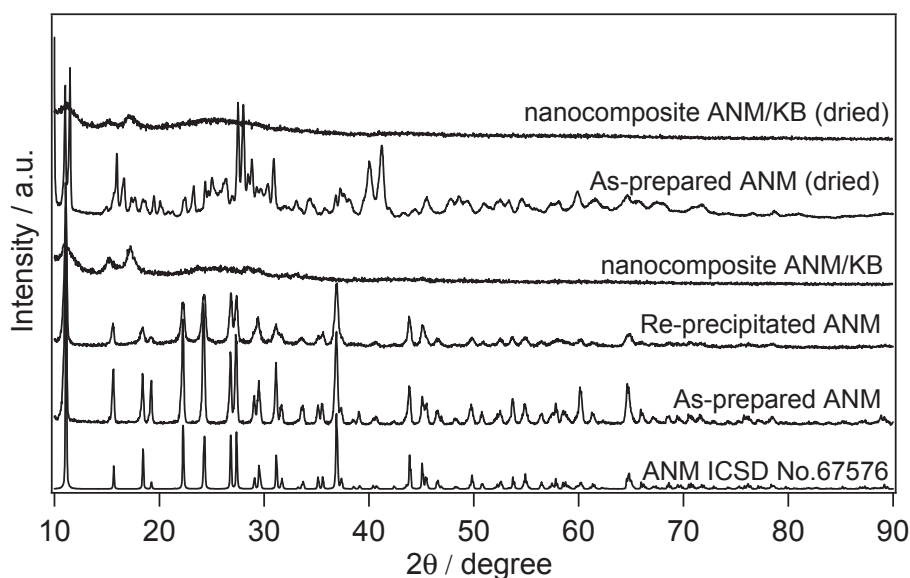


**Figure 4.2** XRD patterns of as-prepared, re-precipitated and nanocomposite samples before and after drying treatment.

Figure 4.2 shows the XRD patterns of as-prepared ANM, re-precipitated ANM, nanocomposite ANM/KB and dried ANM. All of the reflections for as-prepared ANM agree well with those of ANM in ICSD No.67576. The XRD pattern of re-precipitated ANM is consistent with that of as-prepared ANM, confirming the re-appearance of ANM crystal structure by re-precipitation. It is noted that the reflections of re-precipitated ANM become weak and broad compared to those of as-prepared ANM, indicating that the crystal size should be decreased by re-precipitation. Almost all of the reflections (except the three broad peaks at  $2\theta=11.03^\circ$ ,  $15.11^\circ$  and  $17.24^\circ$ , respectively) for nanocomposite ANM/KB disappeared, indicating that the crystal

structure of ANM tends to be amorphous after *in situ* re-precipitation in KB matrix. After drying treatment, the XRD pattern of ANM is different from that of ANM before drying, which should be caused by the removal of crystal water in ANM, while the XRD pattern of nanocomposite ANM/KB does not change but the three main diffractions become weaker and broader compared to the sample before drying.

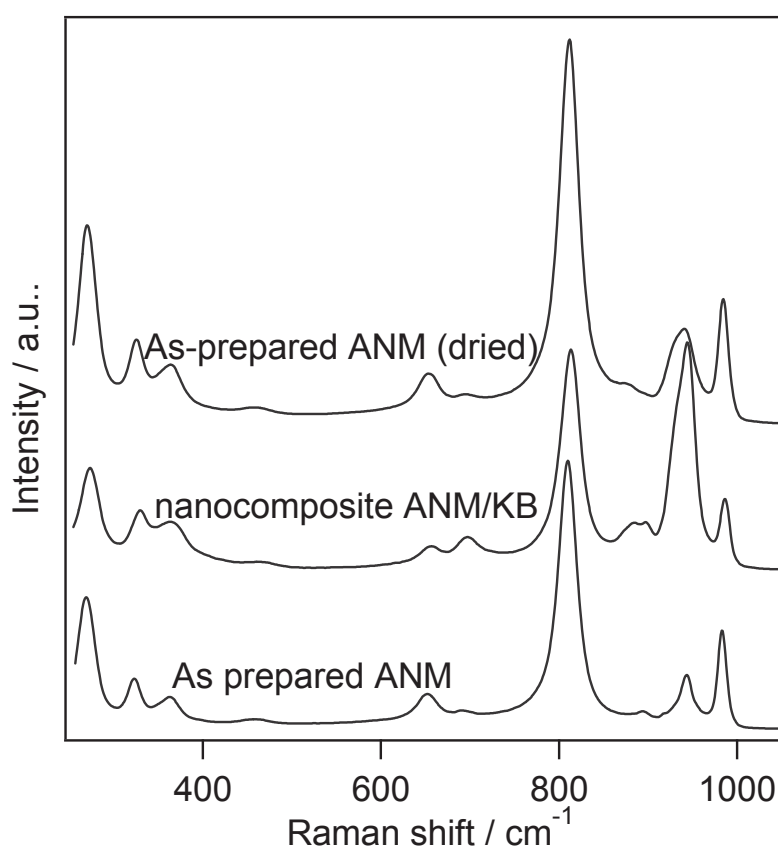


**Figure 4.3** Raman spectra of as-prepared ANM and nanocomposite ANM/KB before drying treatment and as-prepared ANM after drying treatment.

To confirm the structural stability of molecular cluster ion  $[\text{NiMo}_9\text{O}_{32}]^{6-}$  after *in situ* re-precipitating in KB matrix and drying treatment, the Raman spectra were measured, as shown in Figure 4.3. The characteristic peaks for nanocomposite ANM/KB and

dried ANM agree well with those of samples before drying, indicating that the structure of the molecular cluster ion  $[\text{NiMo}_9\text{O}_{32}]^{6-}$  is maintained even the crystal structure is changed by *in situ* re-precipitating ANM in KB matrix or by drying treatment.

### 4.3.2 Thermal Stability

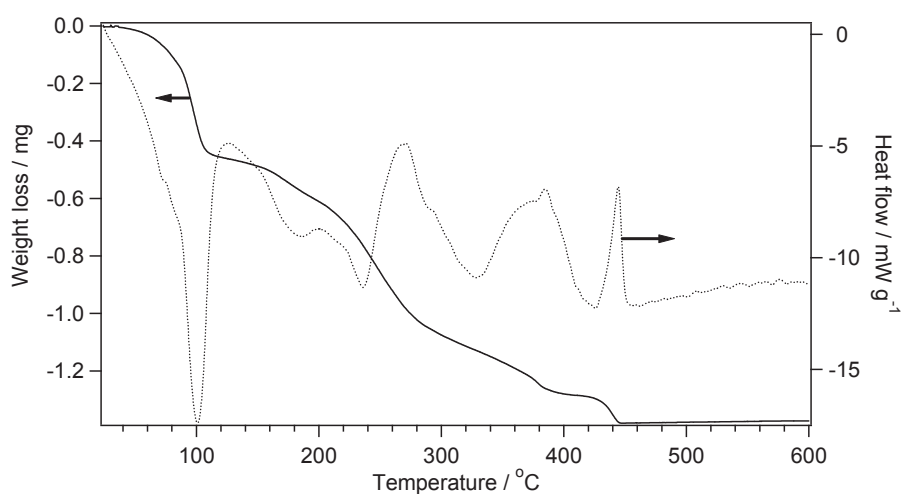


**Figure 4.4** TG-DTA curves of  $(\text{NH}_4)_6[\text{NiMo}_9\text{O}_{32}]$ .

Figure 4.4 shows TG-DTA analysis of the synthesized ANM. The significant water loss associated with endothermic peak exhibited around 100 °C. The exothermic peaks appeared at 200 and 270 °C indicate the decomposition of ANM.

### 4.3.3 Crystal Morphology

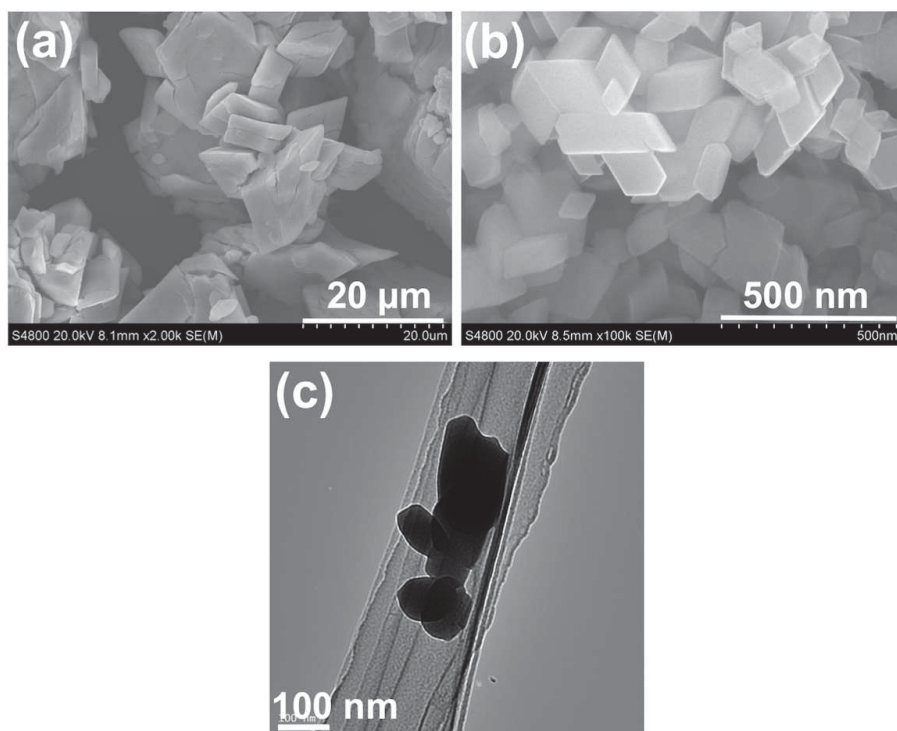


**Figure 4.5** SEM images of (a) as-prepared ANM and (b) re-precipitated ANM; (c) TEM image of re-precipitated ANM.

The morphologies of as-prepared and re-precipitated ANM are shown in Figure 4.5a and b, respectively. The as-prepared crystals are in bulk microsize, while the re-precipitated crystals are in nanosize. TEM image in Figure 4.5c shows that particle size of re-precipitated ANM is in ~100 nm.

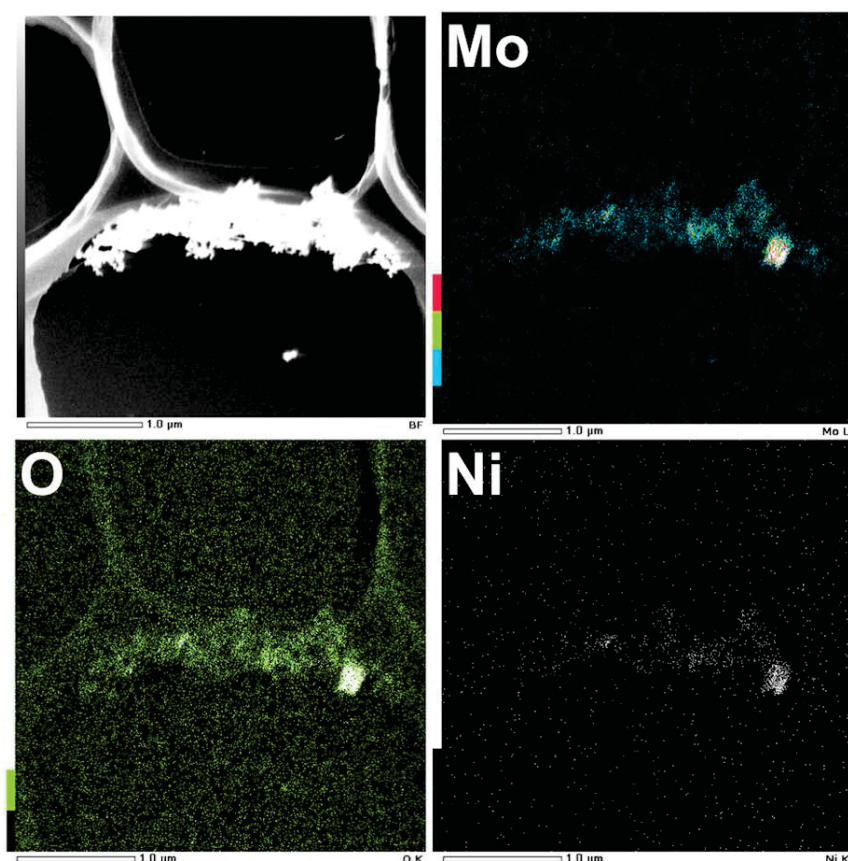


**Figure 4.6** STEM image of nanocomposite ANM/KB and element mappings of Mo, O and Ni.

Figure 4.6 shows the STEM image and element mappings of Ni, Mo and O in KB matrix, confirming that ANM *in situ* re-precipitated successfully in the micropores or mesopores of KB matrix. It is confirmed that all of the dissolved as-prepared ANM *in situ* re-precipitated in the KB matrix, because no any solid product was observed after drying the filtrate. Therefore, the weight ratio for ANM/KB in the composite is equal to 1/2.

### 4.3.4 Electrochemical Properties

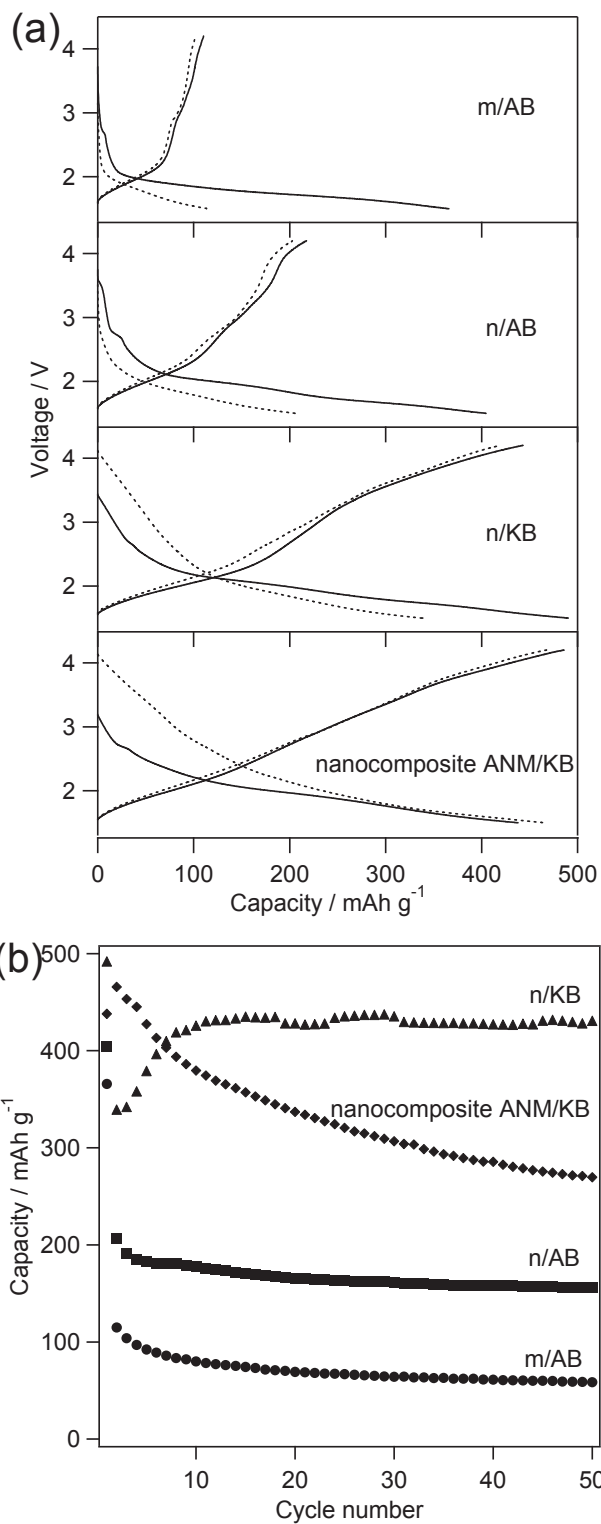


**Figure 4.7** (a) First discharge-charge curves (solid line: first cycle; dash line: second cycle) and (b) cycle performance of ANM at the current density of 17 mA g<sup>-1</sup>.

Figure 4.7a shows the first two discharge-charge curves of microsize ANM particles hand-ground with AB (m/AB), nanosize ANM particles hand-ground with AB (n/AB), nanosize ANM particles hand-ground with KB (n/KB) and nanocomposite ANM/KB at the current density of  $17 \text{ mA g}^{-1}$ . Although large initial discharge capacity of  $366 \text{ mAh g}^{-1}$  is obtained for m/AB, high polarization appears in the following charge process, which causes very large irreversible charge capacity of  $256 \text{ mAh g}^{-1}$ . By decreasing the particles size to nanoscale, the initial discharge capacity is improved to  $405 \text{ mAh g}^{-1}$  for n/AB, and the polarization in the following charge process is decreased; however, there is also a large irreversible charge capacity of  $187 \text{ mAh g}^{-1}$ . After the second discharge, both m/AB and n/AB show large capacity loss, but almost reversible capacities are obtained in the second charge process compared to the first cycle. Due to the multi-electron redox that becomes available in the discharge-charge process by using POMs as cathode materials of lithium battery [4-6], much higher discharge capacity is expected to be obtained by mixing ANM with conductive additive with higher electric conductivity in comparison with AB conductive additive. With this perspective, AB was changed to KB as the conductive additive, because KB has higher electric conductivity and larger specific surface area than that of AB [7]. As expected, the initial discharge capacity of ANM is further improved to  $490 \text{ mAh g}^{-1}$  by mixing nanosize particles with KB. The polarization is greatly decreased and the irreversible capacity is reduced to  $47 \text{ mAh g}^{-1}$  in the following charge process for n/KB. It should be noted that the average discharge-charge voltage of n/KB is slightly improved in the second cycle, while

those of m/AB and n/AB decrease relative to the first cycle. Unfortunately, in comparison with n/KB, higher discharge capacity is not obtained from nanocomposite ANM/KB, even though the particle size of ANM is further decreased by *in situ* re-precipitating in the micropores or mesopores of KB matrix. The nanocomposite ANM/KB shows initial discharge capacity of 438 mAh g<sup>-1</sup>, which is lower than that of n/KB. In addition, in the following charge process, the nanocomposite ANM/KB shows overcharge behavior at the voltage higher than 4.0 V, resulting in irreversible charge capacity of 48 mAh g<sup>-1</sup>, which seems to be induced from the electrolyte decomposition. It is speculated that the catalytic activity of ANM might be enhanced by encapsulating the particles in the micropores or mesopores of KB matrix, which would possess higher contact surface area between the ANM and KB. This would induce the oxidative decomposition of electrolyte in the higher voltage region. Originally, catalytic activity of POMs has been reported in many reaction systems [8], the expanded contact surface area between nanosize ANM and KB would raise its reactivity toward the electrolyte decomposition. In the second cycle, nanocomposite ANM/KB shows almost reversible discharge and charge capacities over 465 mAh g<sup>-1</sup>. In comparison with n/KB, nanocomposite ANM/KB shows higher improvement in the average discharge-charge voltage during the second cycle. Figure 4.7b shows the cycle performance of ANM after 50 cycles at the current density of 17 mA g<sup>-1</sup>. Both m/AB and n/AB show gradual capacity fading with the increase of cycle number. After 50 cycles, discharge capacities of 59 and 156 mAh g<sup>-1</sup>, corresponding to capacity retentions of 16.1% and 38.5%, are obtained for m/AB and n/AB,

respectively. n/KB shows very stable cycle performance after the first 10 cycles, and discharge capacity of  $429 \text{ mAh g}^{-1}$  corresponding to capacity retention of 87.6% is obtained after 50 cycles, whereas nanocomposite ANM/KB shows fast capacity fading with the increase of cycle number after the second cycle, and retains capacity retention of 61.6% after 50 cycles. This means that the further decrease in particle size by encapsulating ANM in the micropores or mesopores of KB matrix is unavailable to achieve the higher discharge capacity at the low current density, compared to the nanosize particles obtained from re-precipitating in the solution.

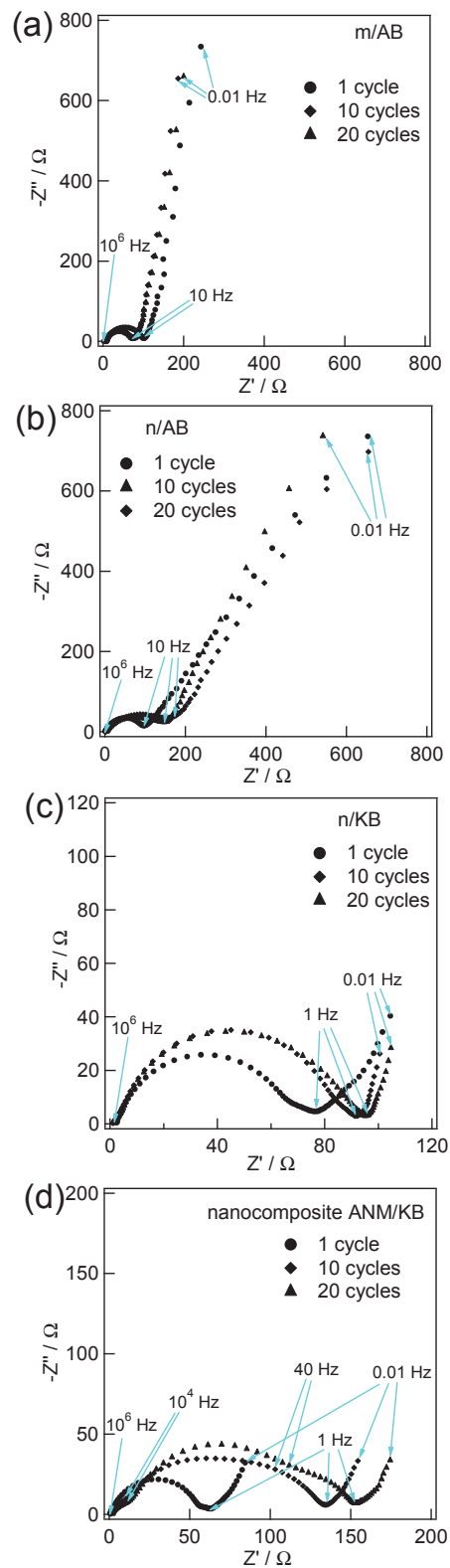
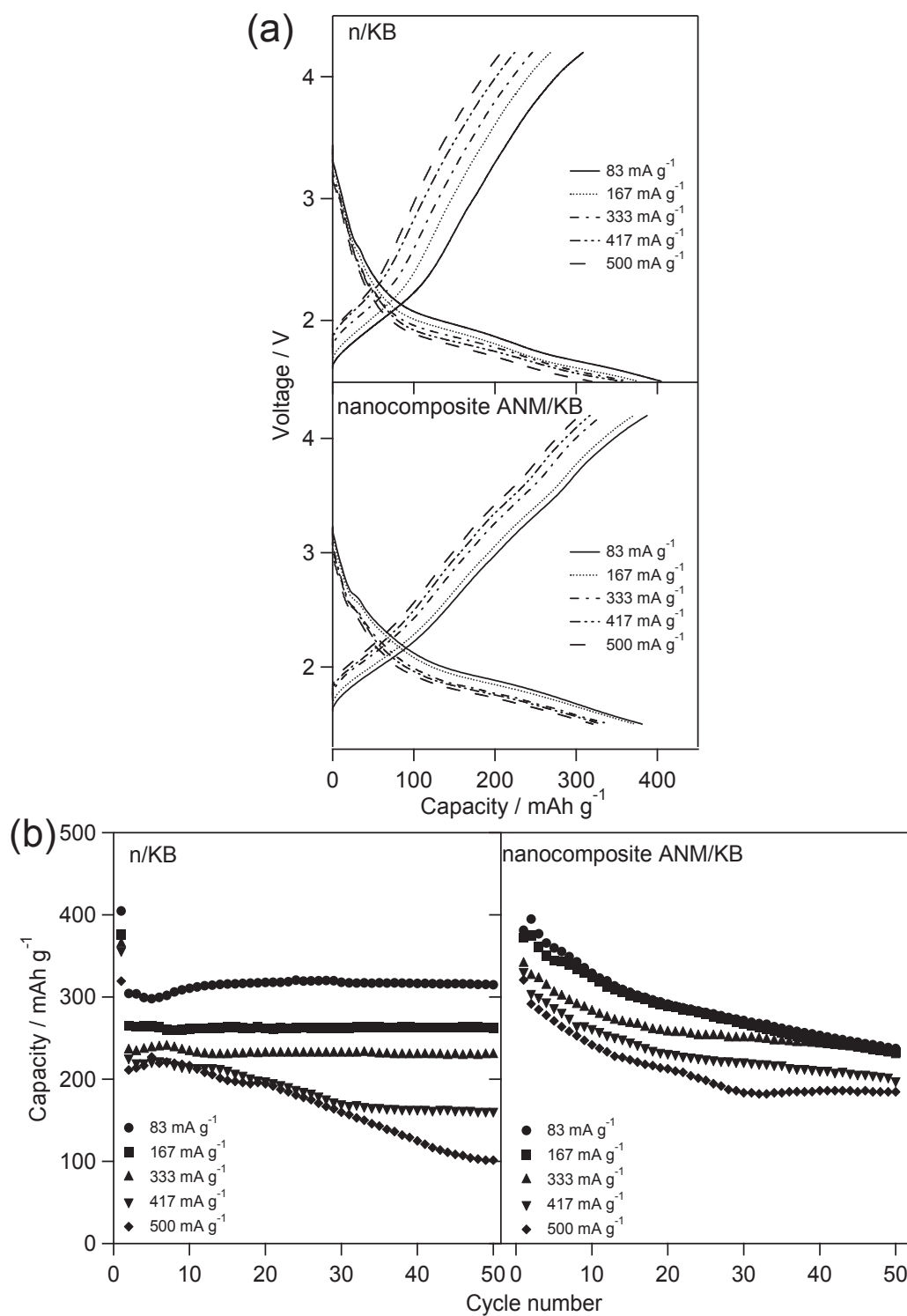


**Figure 4.8** Nyquist plots of (a) m/AB, (b) n/AB, (c) n/KB and (d) nanocomposite ANM/KB

recorded after one cycle, 10 cycles and 20 cycles at the current density of  $17 \text{ mA g}^{-1}$ .

To analyze the difference in the cycle performance for the four different systems, EIS were recorded after different numbers of cycles. Figure 4.8 shows the Nyquist plots of the cells cycled at the current density of  $17 \text{ mA g}^{-1}$ . The linear part of the Nyquist plot after one cycle in low-frequency range  $10\text{--}0.01 \text{ Hz}$  for m/AB is almost vertical to the  $Z'$ -axis (Figure 4.8a). This steep sloping line reflects the capacitive effect instead of the solid-state diffusion of lithium ions (Warburg diffusion) in the bulk cathode material [9, 10]. This means that the lithium is difficult to be extracted in the first charge process, which should be responsible for the large irreversible charge capacity (Figure 4.7a). With the increase of cycle number, this capacitive effect does not change too much. Therefore, the low capacity of m/AB with the increase of cycle number should be caused by this capacitive effect, which is detrimental to the extraction of lithium from the cathode. By decreasing the particle size to nanoscale or adding KB as conductive additive, the capacitive effect is converted to the Warburg diffusion, because the steep sloping line in the low frequency range is changed to the slope line, which approximates to  $45^\circ$  with the  $Z'$ -axis (Figure 4.8b-d), in the frequency ranges of  $10\text{--}0.01 \text{ Hz}$  for n/AB and  $1\text{--}0.01 \text{ Hz}$  for n/KB and nanocomposite ANM/KB. Therefore, the irreversible capacity is decreased due to the appearance of Warburg diffusion in the first charge process for the systems containing nanosize particles or KB conductive additive. However, with the increase of cycle number, the charge-transfer resistance of n/AB in the high frequency range ( $10^6\text{--}10 \text{ Hz}$ ) increases significantly, while that of n/KB in the high frequency range ( $10^6\text{--}1 \text{ Hz}$ ) is not only lower than that of n/AB but also does not increase too much. This indicates

that the inherent low electric conductivity of AB compared to KB is inconspicuous to improve the discharge capacity and cycle stability of nanosize particles (Figure 4.7b). After 10 cycles, the impedance behavior of nanocomposite ANM/KB is different from that of the first cycle. The semicircle in the high frequency range ( $10^6$ –1 Hz) of the Nyquist plot after the first cycle separates into three semicircles, which appear in the high-frequency range ( $10^6$ – $10^4$  Hz), medium-frequency range ( $10^4$ –40 Hz) and low-frequency range (40–1 Hz), respectively. The semicircle in the high-frequency range would be attributed to the solid electrolyte interface on the surface of the anode lithium metal, because its small radius almost does not enlarge from 10th cycle to 20th cycle. The semicircles in the medium-frequency range and the low-frequency range would be attributed to the resistances for the charge-transfer of the cathode material and the surface film on the cathode material which originates from the decomposed species of electrolyte in the charge process, respectively. This result suggests that the formation of surface film on the cathode would be detrimental to the electron and lithium conduction between the cathode and the electrolyte, which should be responsible for the fast capacity loss of nanocomposite ANM/KB with long-term cycling (Figure 4.7b).



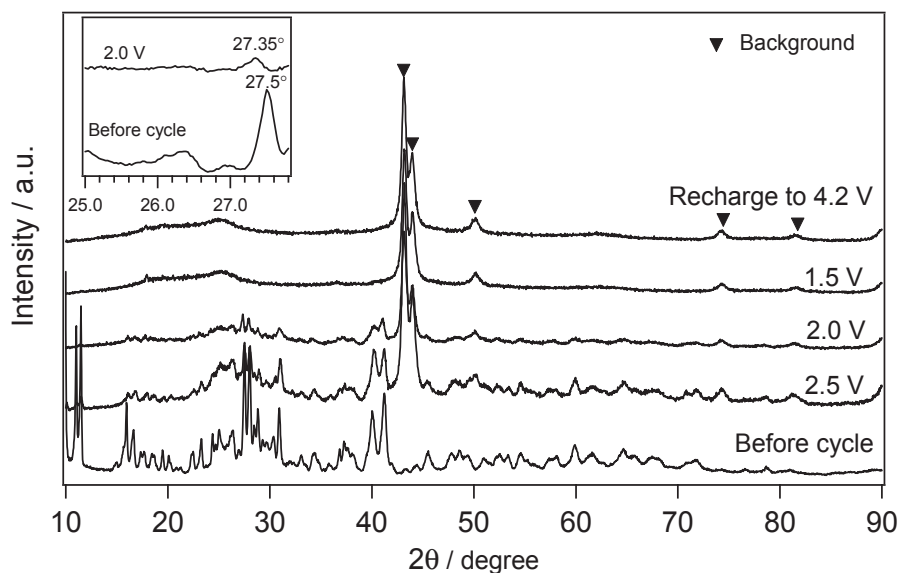
**Figure 4.9** (a) First discharge-charge curves and (b) cycle performance of ANM at the higher various current densities of 83, 167, 333, 417 and 500 mA g<sup>-1</sup>.

Figure 4.9a shows the first discharge-charge curves of n/KB and nanocomposite

ANM/KB at the higher current densities from 83 to 500 mA g<sup>-1</sup>. Although significant capacity drop exhibits, in comparison with that of the cathodes cycling at the low current density of 17 mA g<sup>-1</sup>, high initial discharge capacity over 300 mAh g<sup>-1</sup> is obtained for the two systems at the various higher current densities. With the increase of current density from 83 to 417 mA g<sup>-1</sup>, n/KB shows higher initial discharge capacities than nanocomposite ANM/KB. However, n/KB shows large irreversible capacities in the following charge processes, whereas almost reversible charge capacities are obtained for nanocomposite ANM/KB. At the current density of 500 mA g<sup>-1</sup>, both n/KB and nanocomposite ANM/KB show almost the same initial discharge capacity, but there is larger irreversible capacity loss for n/KB than nanocomposite ANM/KB in the following charge process. The cycle performance of the two systems at the higher various current densities is shown in Figure 4.9b. After the first cycle, in comparison with the cycle performance of the two cathodes at the low current density of 17 mA g<sup>-1</sup> (Figure 4.7b), significant capacity drop is obtained for n/KB with the increase of the current density, while nanocomposite ANM/KB shows less capacity drop. However, after the first cycle, n/KB shows stable cycle performance at the current densities from 83 to 333 mA g<sup>-1</sup>, while nanocomposite ANM/KB shows gradual capacity fading with the increase of cycle number. But, the discharge capacities of nanocomposite ANM/KB are higher than those of n/KB during the 2–10, 2–30 and 2–50 cycles at the current densities of 83, 167 and 333 mA g<sup>-1</sup>, respectively. With the current density further increasing from 417 to 500 mA g<sup>-1</sup>, the discharge capacities of n/KB become lower than those of nanocomposite ANM/KB

from 2th to 50th cycle. Particularly, at the current density of  $500 \text{ mA g}^{-1}$ , n/KB shows fast capacity loss from the 20th cycle, while the cycle performance of nanocomposite ANM/KB tends to be stable after the 30th cycle. The gradual capacity loss of nanocomposite ANM/KB at the low current densities might be caused by the formation of surface film that as a result of electrolyte decomposition on the cathode due to the increased catalytic activity of ANM composited with KB, which leads to the increase in the interfacial impedance of the cathode, as illustrated in Figure 4.8d. The longer exposed time of the cathode material, in the electrochemically state, to the electrolyte at the lower rates would be easier to promote the reactivity of nanocomposite ANM/KB to the electrolyte.

#### 4.3.5 Discharge-Charge Reaction Mechanism



**Figure 4.10** *Ex situ* XRD patterns of ANM recorded at voltages of 2.5, 2.0 and 1.5 V in the first discharge and after one cycle.

To investigate the discharge-charge reaction mechanism, the structural change of ANM during the first discharge-charge process was recorded by *ex situ* XRD measurement, as shown in Figure 4.10. The XRD pattern almost does not change when initially discharged to 2.5 V, but the diffractions become weak and broad. Upon further discharging to 2.0 V, most of the reflections disappear and the residual diffractions become much weaker in the intensities, and some reflections shift to lower angle (as illustrated in the inset of Figure 4.10), indicating that the crystal structure of ANM tends to be amorphous and its lattice expands by the insertion of lithium. All of the reflections disappear when discharged to 1.5 V and do not reappear in the following charge process, indicating the crystal structure becomes amorphous after the first discharge and shows irreversibility in the charge process. This result demonstrates the insertion-extraction of lithium during the discharge-charge process is independent from the crystal structure of ANM, which enables the deep discharge-charge process and high reversible capacity.

#### 4.4 Conclusions

Polyoxomolybdate  $(\text{NH}_4)_6[\text{NiMo}_9\text{O}_{32}]$  (ANM) as cathode material of lithium battery shows high initial discharge capacity. Discharge capacity and capacity retention with long-term cycling are improved by decreasing the particle size to nanoscale, particularly, when adding KB with high electric conductivity as the conductive additive. ANM *in situ* re-precipitated in KB matrix shows higher discharge capacity and capacity retention than nanosize ANM particles mixed with KB at the

high rate. The insertion-extraction of lithium during the discharge-charge can continuously proceed in amorphous ANM, which is independent from the crystal structure.

## References

- [1] J. L. T. Waugh, D. P. Shoemaker, L. Pauling, *Acta Cryst.*, 1954, 7, 438–441.
- [2] S. J. Dunne, R. C. Burns, G. A. Lawrance, *Aust. J. Chem.*, 1992, 45, 1943–1952.
- [3] L. C. W. Baker, T. J. R. Weakley, *J. Inorg. Nucl. Chem.*, 1966, 28, 447–454.
- [4] N. Sonoyama, Y. Suganuma, T. Kume, Z. Quan, *J. Power Sources*, 2011, 196, 6822–6827.
- [5] S. Uematsu, Z. Quan, Y. Suganuma, N. Sonoyama, *J. Power Sources*, 2012, 217, 13–20.
- [6] E. Ni, S. Uematsu, Z. Quan, N. Sonoyama, *J. Nanoparticle Research*, 2013, 15, 1723.
- [7] S. Kurodaa, N. Toboria, M. Sakurabab, Y. Sato, *J. Power Sources*, 2003, 119–121, 924–928.
- [8] M. T. Pope, Y. Jeannin, M. Fournier, *Heteropoly and Isopoly Oxometalates*. Springer-Verlag: Berlin Heidelberg New York Tokyo, 1983.
- [9] M. D. Levi, G. Salitra, B. Markovsky, H. Teller, D. Aurbach, U. Heider, L. Heiderb, *J. Electrochem. Soc.*, 1999, 164, 1279–1289.
- [10] J. Y. Song, H. H. Lee, Y. Y. Wang, C. C. Wan, *J. Power Sources*, 2002, 111, 255–267.

# Chapter 5

## Synthesis and Electrochemical Properties of Polyoxomolybdate



### 5.1 Introduction

In this chapter, polyoxomolybdate  $(\text{NH}_4)_6[\text{MnMo}_9\text{O}_{32}]$  (AMM) was studied as cathode material of lithium ion battery. The crystal structure of AMM is isomorphous to ANM (Chapter 4), and the molecular cluster ion is similar to ANM by substituting the central heteroatom Ni to Mn. To improve the electric conductivity of AMM, the particle size was also decreased to nanoscale by re-precipitating.

### 5.2 Experimental

#### 5.2.1 Synthesis of Materials

##### *(1) Synthesis of AMM*

The synthesis was carried out as for the ANM shown in Chapter 4, substituting  $\text{MnSO}_4 \cdot 6\text{H}_2\text{O}$  for  $\text{NiSO}_4 \cdot 6\text{H}_2\text{O}$ . 4.37 g  $(\text{NH}_4)_6\text{Mo}_7\text{O}_{24} \cdot 4\text{H}_2\text{O}$  (Wako, GR) dissolved in 25 ml distilled water and heated to 95 °C, then a 25 ml solution containing 0.603 g  $\text{MnSO}_4 \cdot 5\text{H}_2\text{O}$  (Wako, GR) and 0.571 g  $(\text{NH}_4)_2\text{S}_2\text{O}_8$  (Kishida, GR) was added to the hot solution. The mixture was boiled and stirred for 5 min, then filtered the hot solution quickly. Yellow product precipitated out after cooling the filtrate with stirring

for 1h. The precipitate was filtered and washed with 50 ml 1:1 v/v acetone-distilled water. To remove the water contained in the products, all of the as-prepared samples were dried at 120 °C under air for 1h.

### *(2) Synthesis of Nanosize Particles*

To synthesis the nanosize AMM particles, 0.15 g as-prepared AMM powders were dissolved in 10 ml distilled water. The re-crystallized AMM particles were immediately obtained by adding 50 ml ethanol to the solution, followed with centrifugation and washed with acetone.

### *(3) Synthesis of Nanocomposite AMM/KB*

For the preparation of nanocomposite AMM/KB (AMM *in situ* re-precipitated in the micropores or mesopores of KB matrix), 0.6 g KB powders were added to the 20 ml solution containing 0.318 g (to obtain the weight ratio of AMM/KB=2/1 for electrode fabrication, the water loss of 5.5% for AMM after drying treatment is calculated) dissolved as-prepared AMM powders, followed with ultrasonic dispersion for 30 min, then added 100 ml ethanol to the mixture, and filtered and washed the product with acetone.

## **5.2.2 Electrochemical Measurements**

Unless otherwise noted, the cathode consisted of AMM active material, AB or KB conductive additive and PTFE binder in the weight ratio of 32:64:4. The

electrochemical properties of AMM electrode were tested at 25 °C by using CR-2032 coin cells, which were assembled in an argon filled glovebox using metallic lithium (Honjyo metal) as anode, and 1 M LiPF<sub>6</sub> in mixture of ethylene carbonate (EC) and diethyl carbonate (DEC) (3:7, v/v: Kishida battery grade) as the electrolyte solution. The discharge-charge properties of the cells were recorded on a battery tester (Interface model OZO-A19) between 1.5 and 4.2 V (vs. Li/Li<sup>+</sup>) at the current densities from 17 to 417 mA g<sup>-1</sup>.

## 5.3 Results and Discussion

### 5.3.1 Crystal and Molecular Structures

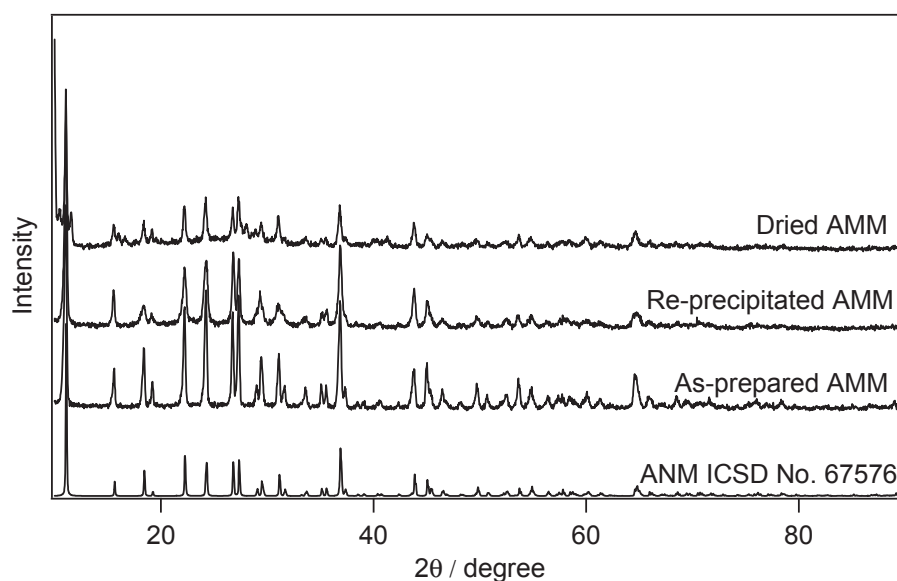


**Figure 5.1** XRD patterns of as-prepared, re-precipitated and dried AMM samples.

Figure 5.1 shows the XRD patterns of as-prepared AMM, re-precipitated AMM, and dried AMM. All of the reflections for as-prepared AMM agree well with those of ANM in ICSD No.67576. The XRD pattern of re-precipitated AMM is consistent with that of as-prepared AMM, confirming the re-appearance of AMM crystal structure by

re-precipitation. It is noted that the reflections of re-precipitated AMM become weak and broad compared to those of as-prepared AMM, indicating that the crystal size should be decreased by re-precipitation. After drying treatment, the XRD pattern of AMM is different from that of AMM before drying, which should be caused by the removal of crystal water in AMM.

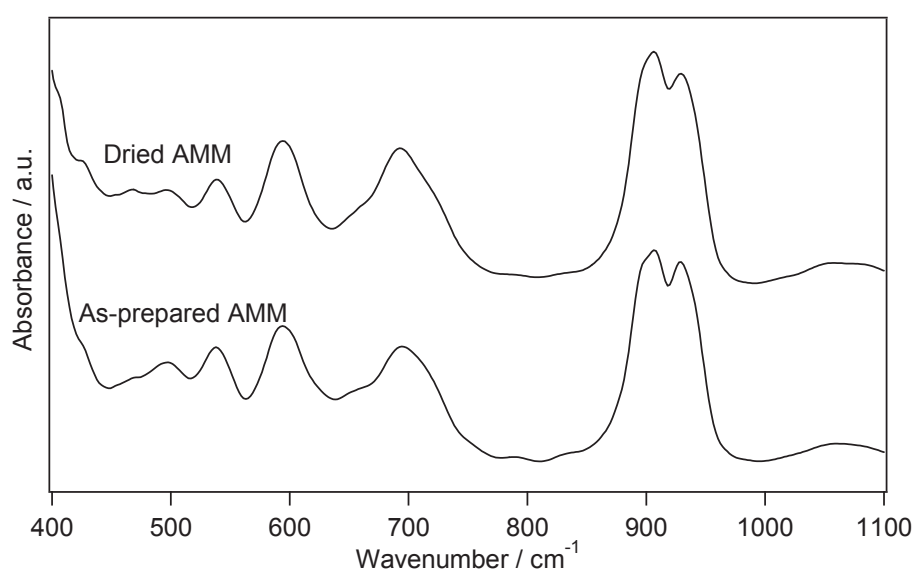


**Figure 5.2** FT-IR spectra of AMM before and after drying treatment.

To confirm the stability of molecular structure of the  $[\text{MnMo}_9\text{O}_{32}]^{6-}$  anion as redox active unit after drying, FT-IR spectra were measured, as shown in Figure 5.2. It is clear that the FT-IR spectra of the dried sample are consistent with the sample before drying. The similar characteristic absorption bands of the hetero-polyanion at 400-1100  $\text{cm}^{-1}$  were observed for the samples with and without drying, demonstrating that the structure of molecular cluster ion  $[\text{MnMo}_9\text{O}_{32}]^{6-}$  was still maintained after drying treatment.

### 5.3.2 Thermal Stability

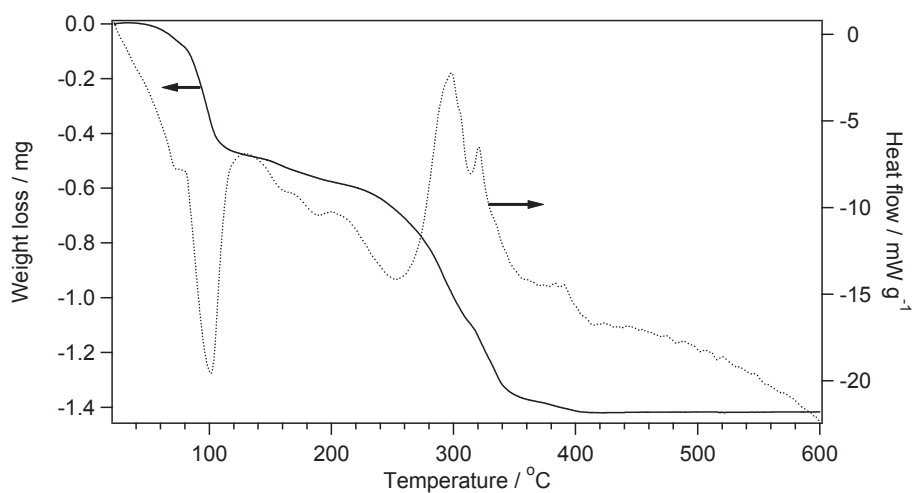


**Figure 5.3** TG-DTA curves of  $(\text{NH}_4)_6[\text{MnMo}_9\text{O}_{32}]$ .

Figure 5.3 shows TG-DTA analysis of the synthesized AMM. The significant water loss associated with endothermic peak exhibited around 100 °C. The exothermic peaks appeared at 200 and 300 °C indicate the decomposition of AMM.

### 5.3.3 Crystal Morphology

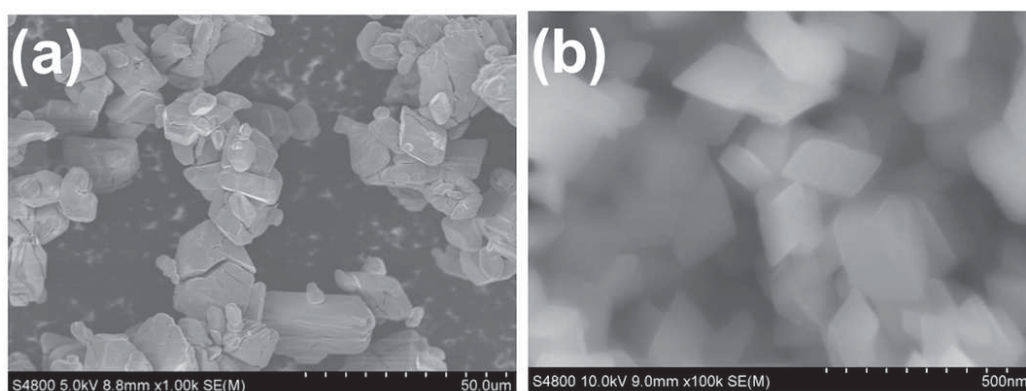


**Figure 5.4** SEM images of (a) as-prepared AMM and (b) re-precipitated AMM.

The morphologies of as-prepared and re-precipitated AMM are shown in Figure 5.4a and b, respectively. The as-prepared crystals are in bulk microsize, while the re-precipitated crystals are in nanosize.

### 5.3.4 Electrochemical Properties

#### (1) AB Conductive Additive on the Discharge-Charge Performance of AMM

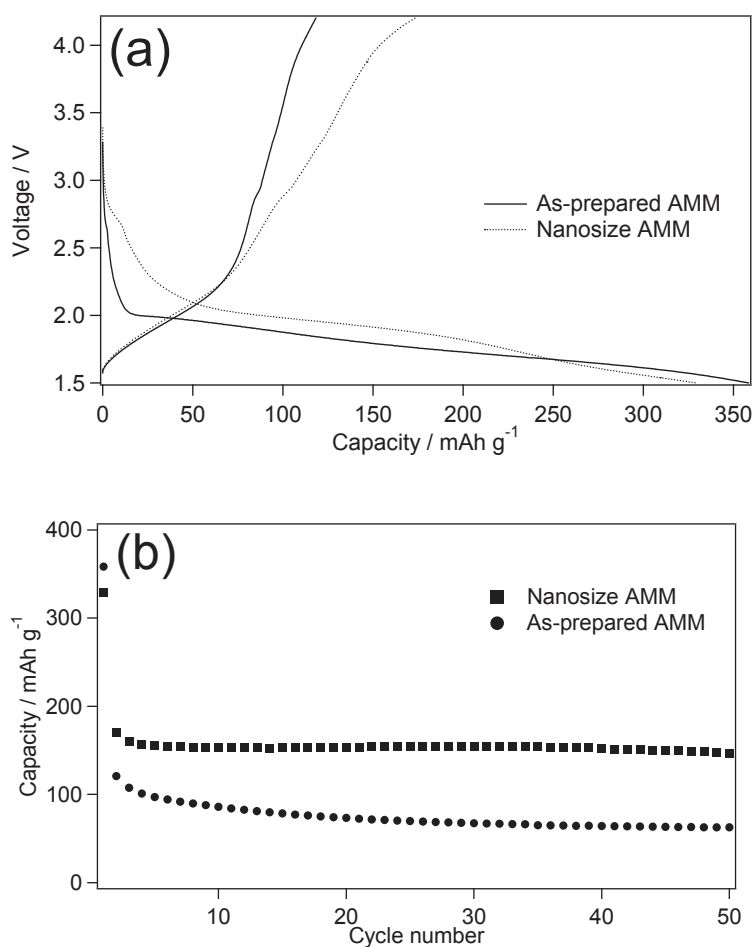


**Figure 5.5** (a) First discharge-charge curves and (b) cycle performance for as-prepared and nanosize AMM.

Figure 5.5a shows the initial discharge-charge curves of as-prepared and nanosize AMM. The initial discharge capacity is not improved by decreasing the particle size

to nanoscale. Both as-prepared and nanosize AMM show large polarization in the following charge process. It is noted that the average discharge voltage is improved by decreasing the particle size to nanoscale. With long-term cycling, nanosize AMM shows higher capacity than that of as-prepared AMM (Figure 5.5b). The low discharge capacity of AMM in nanosize particles should be caused by low electric conductivity of AB conductive.

(2) KB Conductive Additive on the Discharge-Charge performance of AMM

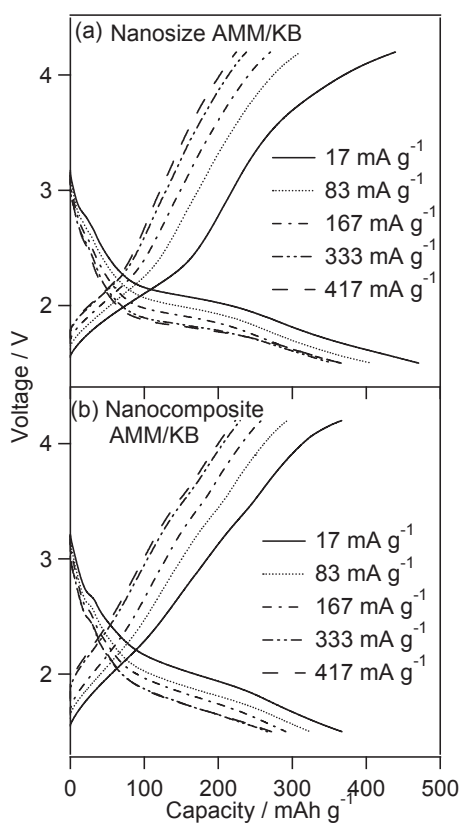


**Figure 5.6** First discharge-charge curves of (a) nanosize AMM mixed with KB (nanosize AMM/KB) and (b) AMM *in situ* re-precipitated in KB matrix (nanocomposite AMM/KB) at various current densities.

Figure 5.6 shows the initial discharge-charge curves of AMM at various current densities. Nanosize AMM/KB (Figure 5.6a) shows initial discharge capacities of 471, 407, 367, 355, and 367  $\text{mAh g}^{-1}$  at the current densities of 17, 83, 167, 33, and 417  $\text{mA g}^{-1}$ , respectively, while nanocomposite AMM/KB (Figure 5.6a) shows initial discharge capacities of 367, 325, 291, 267, and 271  $\text{mAh g}^{-1}$  at that of current densities. Although the particle size is further decreased by *in situ* re-precipitated in KB matrix, AMM shows lower capacity that of nanosize AMM. This would be caused by the dissolution of nanosize AMM into the electrolyte, reducing the loss of active material.

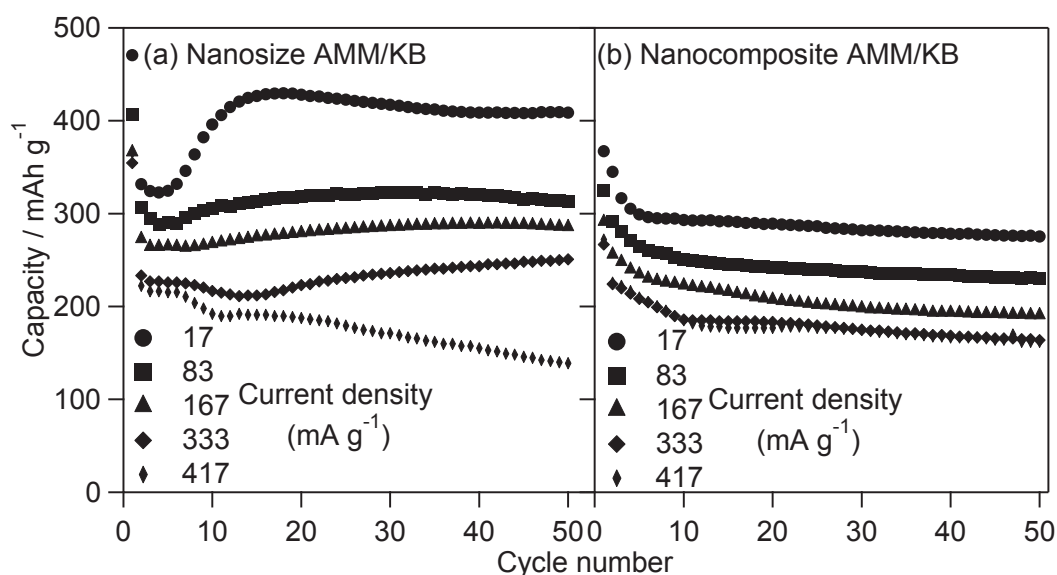


**Figure 5.7** Cycle performance of (a) nanosize AMM mixed with KB (nanosize AMM/KB) and (b) AMM *in situ* re-precipitated in KB matrix (nanocomposite AMM/KB) at various current densities.

The cycle performance of AMM is show in Figure 5.7. It can be seen that nanosize AMM/KB (Figure 5.7a) shows stale cycle performance after the first capacity drop at

the current densities from 17 to 333 mA g<sup>-1</sup>. With the increase of current density to 417 mA g<sup>-1</sup>, nanosize AMM/KB shows dramatically capacity loss. Although nanocomposite AMM/KB (Figure 5.7b) shows lower capacity at the current densities from 17 to 333 mA g<sup>-1</sup>, higher capacity is obtained at the high current density of 417 mA g<sup>-1</sup>. This result demonstrates that nanocomposite AMM/KB can compensate the low electric conductivity of nanosize AMM at the high current density.

## 5.4 Conclusions

Polyoxomolybdate AMM shows high initial discharge capacity. The nanosize AMM mixed with KB conductive additive shows much higher discharge capacity than that of AMM mixed with AB conductive additive. AMM *in situ* re-precipitated in KB matrix, which possesses smaller particle size shows higher discharge capacity than that of nanosize AMM re-precipitated from the water-organic solution at the high rate.



# Chapter 6

## Synthesis and Electrochemical Properties of Anderson Type

### Polyoxomolybdate $\text{Na}_3[\text{AlMo}_6\text{O}_{24}\text{H}_6]$

#### 6.1 Introduction

In this chapter, an Anderson type polyoxomolybdate,  $\text{Na}_3[\text{AlMo}_6\text{O}_{24}\text{H}_6]$  (NAM) was utilized as cathode material of lithium battery with high capacity and stability. Figure 6.1 shows the structure of Anderson type polyoxomolybdate and the crystal structure of NAM. In the Anderson type structure, all  $\text{MoO}_6$  octahedra are directly connecting with central  $\text{Al}^{3+}$  ion by the covalent bonding, and all the metal atoms are in a common plane. This structure is expected to be stable during the redox owing to the strong covalent binding. The crystal structure of NAM has three-dimensional framework in which lithium ions can diffuse.

To improve the low electric conductivity of NAM, NAM was mixed with acetylene black (AB) or KB by hand-grinding and ball-milling, and the electrochemical properties of NAM were compared. The crystal structure changes of NAM and the structural stability of molecular cluster ion  $[\text{AlMo}_6\text{O}_{24}\text{H}_6]^{3-}$  during the discharge-charge process were investigated by *ex situ* XRD and *ex situ* Raman measurement.

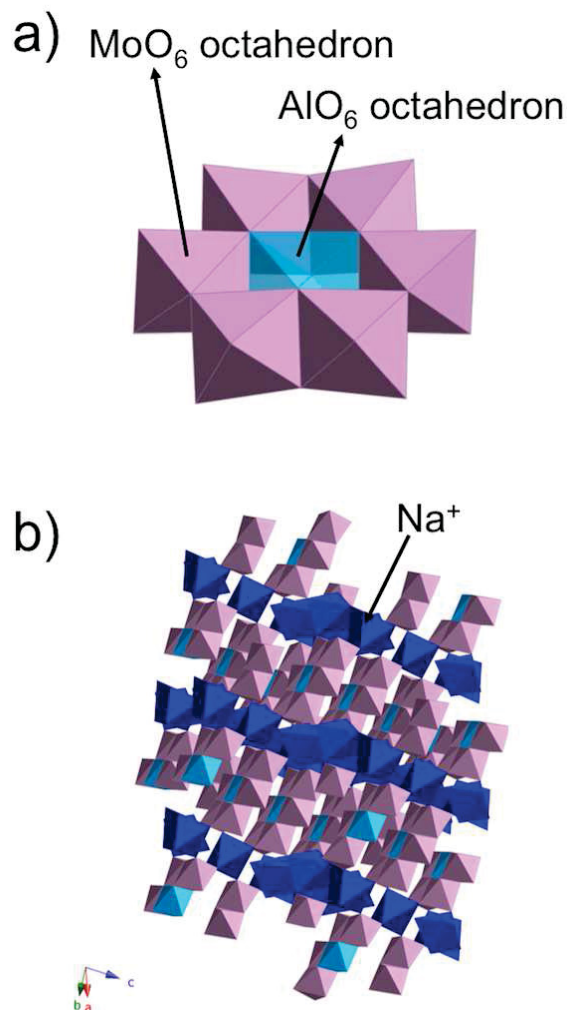


**Figure 6.1** a) Structure of Anderson type polyoxomolybdate; b) crystal structure of  $\text{Na}_3[\text{AlMo}_6\text{O}_{24}\text{H}_6]$ .

## 6.2 Experimental

### 6.2.1 Synthesis of Materials

The reported synthesis method of NAM was modified [1]. The synthesis procedure is summarized as follows [2]. 3.5 g  $\text{Na}_2\text{MoO}_4 \cdot 2\text{H}_2\text{O}$  (Kishida, GR) was added to a solution of 0.829 g  $\text{AlCl}_3$  (Kishida, GR) in 25 ml of distilled water with stirring. The pH of the solution was adjusted to 1.8 by dropwise addition of 35% hydrochloric acid (Kishida, GR). Thereafter the clear solution was evaporated slowly at 40 °C with

stirring. The white crystal precipitate was filtered, washed with 2:1 v/v acetone-distilled water followed with acetone. To remove the water in crystal, the obtained powders were dried at 80 °C for 12 h.

### 6.2.2 Characterization

The crystal structure of NAM powder was identified by XRD measurement using a powder X-ray diffractometer (Rigaku RAD-C) with Cu K $\alpha$  (40 kV, 40 mA) radiation. The diffraction data were collected from 10 to 90° in  $2\theta$ . Morphology of NAM particles was obtained by a scanning electron microscope (HITACHI S-4800). FT-IR spectra were collected with a JASCO-410 spectrometer in the range of 500–1200 cm<sup>-1</sup>. Pellets for FT-IR measurement were prepared by grinding and pressing samples with dried KBr powder (Kishida infrared spectra grade).

The structural change of NAM during discharge-charge process was investigated by *ex situ* XRD under Ar atmosphere. After discharge and charge of the cells, the cathode materials were removed from separable cells (Hosen HS cell) in Ar atmosphere glovebox. After rinsing with dimethyl carbonate (Kishida battery grade) and drying in glovebox, *ex situ* XRD measurements were performed by enclosing the cathode sample in lab made cell equipped with Mylar film window. *Ex situ* Raman spectra were recorded by covering the cathode sample closely with a glass sheet with thickness of 0.15 mm and sealing the edges of glasses with resin.

### 6.2.3 Electrochemical Measurements

The electrochemical properties of NAM electrodes were tested at 25 °C by using CR-2032 coin cells, which were assembled in an argon filled glovebox using metallic lithium (Honjyo metal) as anode, and 1 M LiPF<sub>6</sub> in mixture of ethylene carbonate (EC) and diethyl carbonate (DEC) (3:7, v/v: Kishida battery grade) as the electrolyte solution. The cathodes were prepared either by hand-grinding NAM with AB or KB, or dry mechanical milling NAM with AB or KB with planetary ball mill (Fritsch P-7) under air. The following conditions were used for the ball-milling. NAM weight: 50 mg, 100 mg, 200 mg or 300 mg; AB or KB weight: 100 mg; milling media: three balls with 10.5 mm in diameter each and sixteen smaller balls with 5 mm in diameter each; volume of milling vessel: 45 ml; milling media and vessel material: zirconium dioxide; milling speed: 500 rpm; milling time: 1 hour. Unless specifically noted otherwise, all of the cathodes consisted of NAM active material, AB or KB conductive additives and PTFE binder in the weight ratio of 32:64:4. The discharge-charge properties of the cells were recorded on a battery tester (Interface model OZO-A19) between 1.5 and 4.2 V (vs. Li/Li<sup>+</sup>) at the current density of 17 mA g<sup>-1</sup>. Solartron analytic instruments consisting of a frequency-response analyzer (Solartron 1255) and a potentiostat (Solartron 1280) were used to acquire electrochemical impedance spectroscopy (EIS) in the frequency range 10<sup>6</sup>–10<sup>-2</sup> Hz with an amplitude of 10 mV.

## 6.3 Results and Discussion

### 6.3.1 Crystal and Molecular Structures

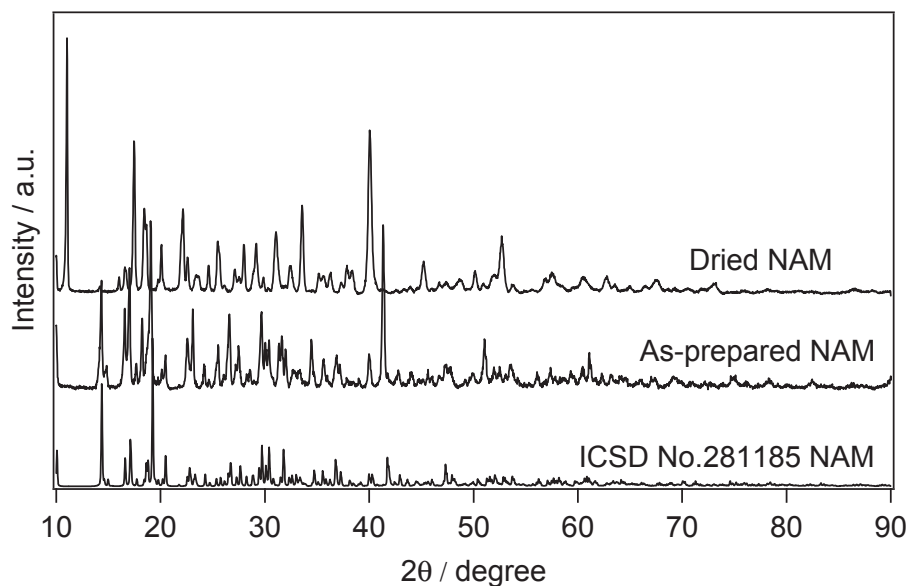


**Figure 6.2** XRD patterns of ICSD No. 281185, as-prepared and dried NAM.

The XRD pattern of as-prepared NAM is shown in Figure 6.2. All of the reflections are consistent with those of NAM in ICSD No. 281185. The crystal structure was refined by the Rietveld analysis using the model with the space group  $P-1$ . The Rietveld refined lattice parameters for as-prepared NAM in this study are  $a=12.13339$  Å,  $b=13.14839$  Å,  $c=14.25429$  Å,  $\alpha=80.7819^\circ$ ,  $\beta=74.6745^\circ$ ,  $\gamma=68.6884^\circ$ , those are a little different from those of the reported NAM [3]. It is noted that the intensity ratios of the as-prepared NAM around  $2\theta = 10-20^\circ$  do not match well the ICSD pattern. This would be caused by the difference in the orientation of powders. The conditions for the crystal growth in our work are different from that of the reported one in ICSD, because the planar ion would be oriented easily. The XRD pattern of NAM after

drying treatment was different from NAM before drying, which would be caused by the removal of crystal water in NAM.

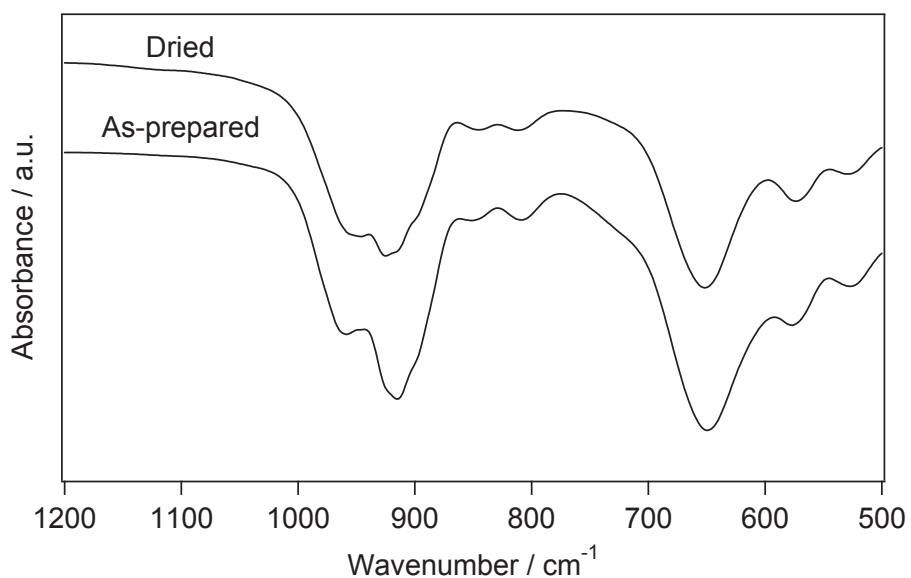


**Figure 6.3** FT-IR spectra of as-prepared and dried NAM.

To confirm the structural stability of molecular cluster ion  $[\text{AlMo}_6\text{O}_{24}\text{H}_6]^{3-}$  after drying treatment, the FT-IR spectra were measured. As can be seen in Figure 6.3, the characteristic peaks of dried NAM in the wavenumber range of  $500\text{--}1200\text{ cm}^{-1}$  were agreed with those of as-prepared NAM before drying, indicating that the structure of the molecular cluster ion was maintained even after the crystal structure change of NAM by drying treatment.

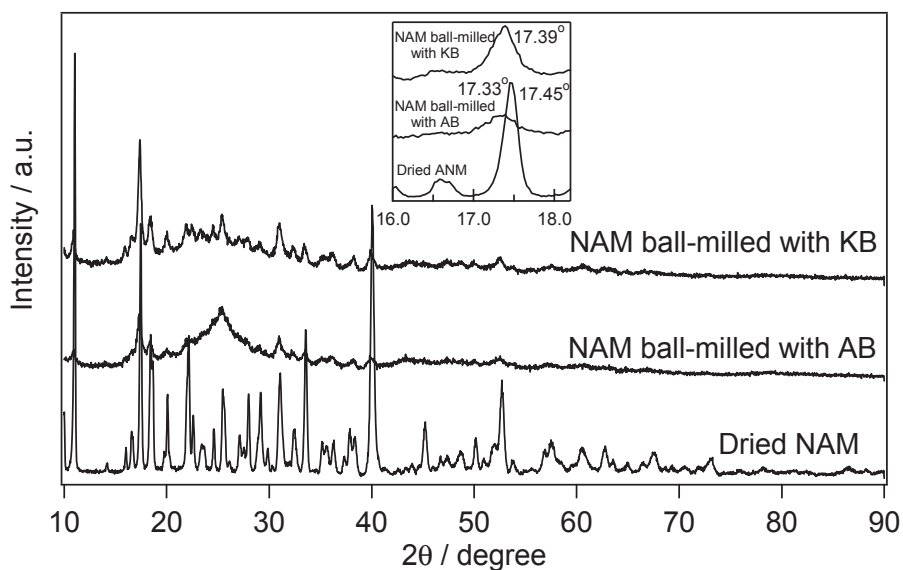


**Figure 6.4** XRD patterns of NAM after ball-milling with AB or KB.

Figure 6.4 shows the XRD patterns of NAM after ball-milling with AB or KB. Most of the reflections in the  $41^\circ < 2\theta < 90^\circ$  almost disappeared for the ball-milled samples, while the reflections in the  $10^\circ < 2\theta < 41^\circ$  became weaker and broader compared with the sample without ball-milling, demonstrating that the crystallinity of the ball-milled samples decreased. In addition, the positions of reflections for the ball-milled samples shifted to the lower angles (as illustrated in the inset of Figure 6.4). This indicates that a slight expansion of lattice by ball-milling with the conductive additives. This result is consistent with the variability of the NAM crystal by drying.

### 6.3.2 Crystal Morphology

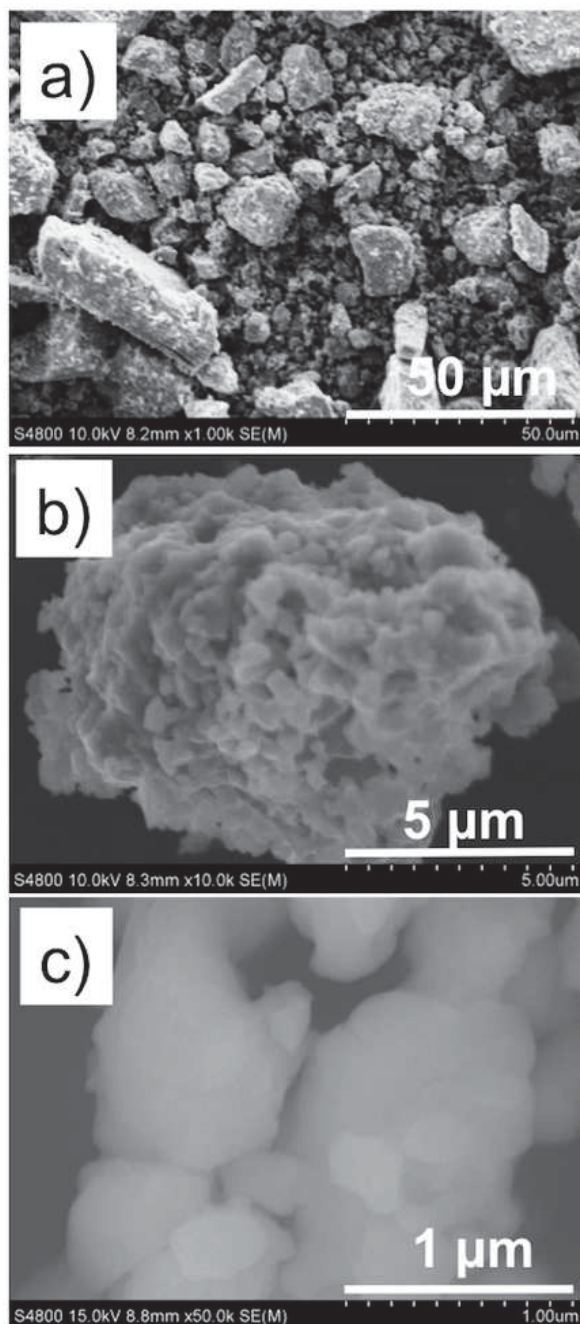
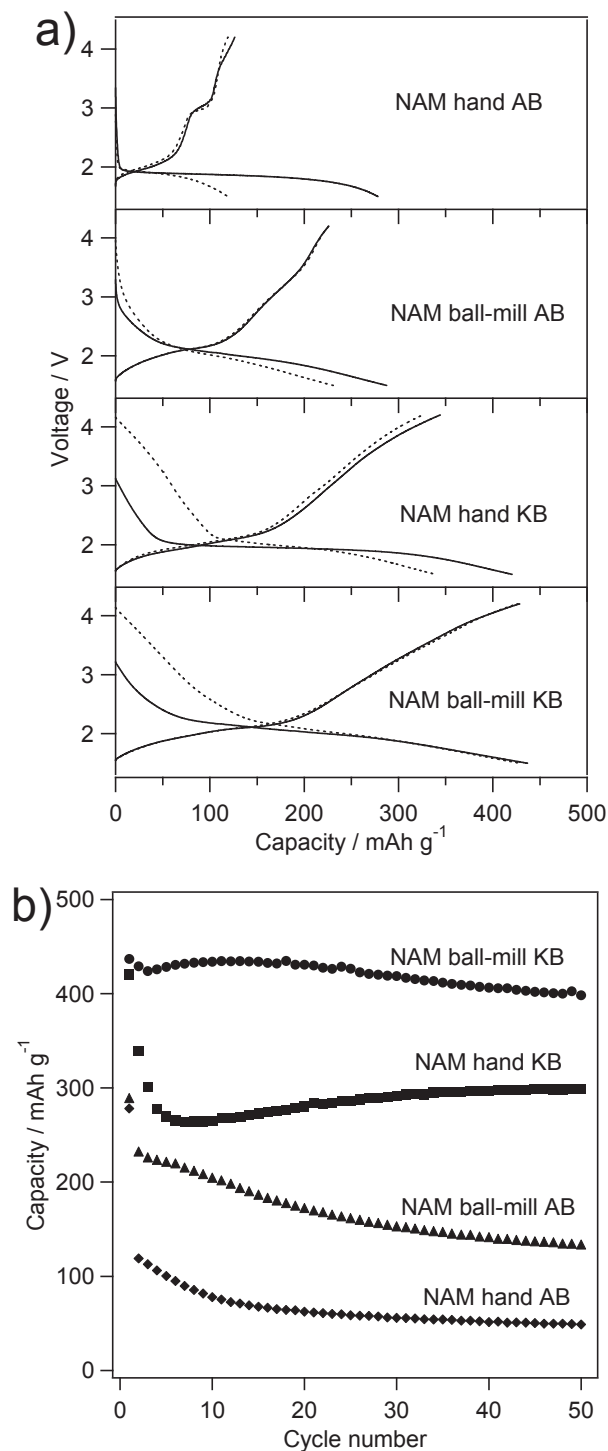


**Figure 6.5** The morphology of as-prepared NAM observed at different magnifications: a)  $\times 1k$ ; b)  $\times 10k$ ; c)  $\times 50k$

Figure 6.5 shows the morphology of as-prepared NAM observed by SEM at different magnifications, the surface images revealed that the powders of NAM were

aggregates of shapeless particulates from nanosize to microsize.

### 6.3.3 Electrochemical Properties



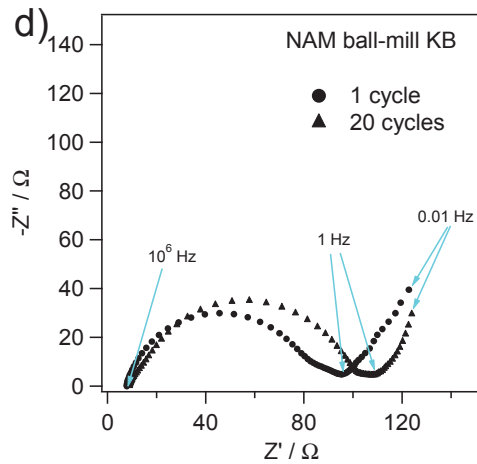
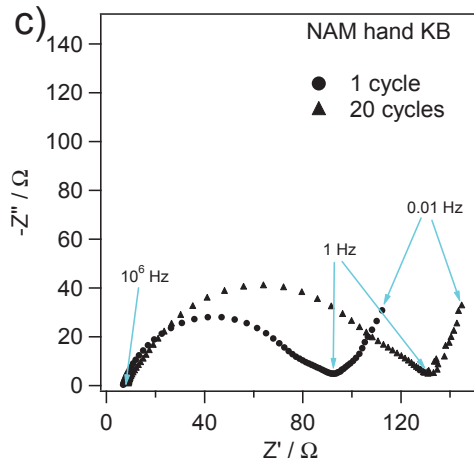
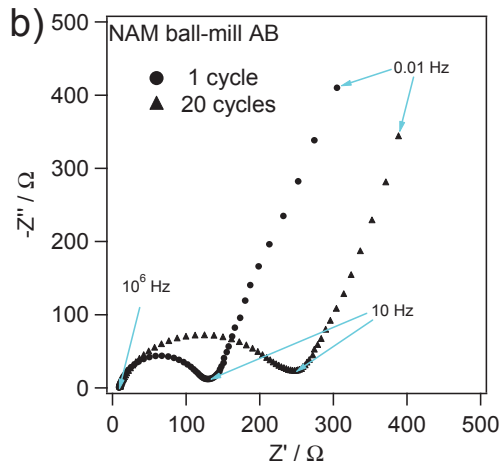
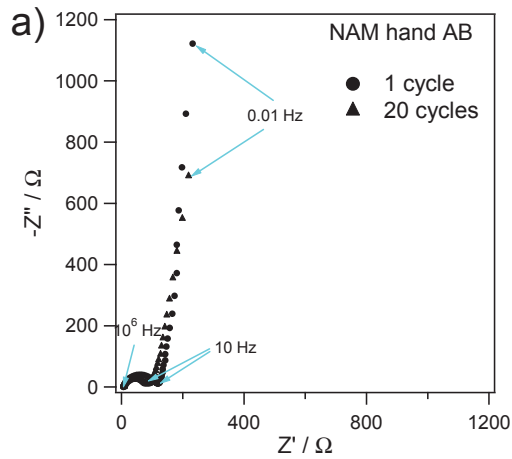
**Figure 6.6** a) The first two discharge-charge cycle curves (solid lines: 1st cycle, dash lines: 2nd cycle) and b) cycle performance of the different systems.

Figure 6.6a shows discharge-charge curves in the first and second cycles of NAM mixed with AB by hand-grind (NAM hand AB), with AB by ball-mill (NAM ball-mill AB), with KB by hand-grind (NAM hand KB), with KB by ball-mill (NAM ball-mill KB), respectively. The NAM hand AB showed large flat discharge voltage plateau between 1.8 and 2.0 V and its initial discharge capacity reached 278 mAh g<sup>-1</sup>. In the subsequent charge process, this system showed steep polarization when recharged up to the voltage higher than 2.0 V, and a very small voltage plateau was obtained around 3.0 V. This polarization would be due to the difficulty in extracting the lithium ions from NAM, and caused a very large irreversible capacity loss of 152 mAh g<sup>-1</sup> after the first charge. Interestingly, this polarization was decreased significantly by ball-milling NAM with AB. Initial discharge capacity of 287 mAh g<sup>-1</sup> was obtained by NAM ball-mill AB, which is higher than that of NAM hand AB, and the irreversible capacity loss after the first charge was decreased to 61 mAh g<sup>-1</sup>, which is much lower than that of NAM hand AB. It is noted that the average discharge voltage of NAM ball-mill AB was also improved to 2.11 V compared with that of 1.92 V for NAM hand AB. These results suggest that, as was expected, low electric conductivity caused high polarization to the NAM hand AB system. It is expected that by mixing NAM with conductive additive with higher electric conductivity in comparison with AB conductive additive, much higher discharge capacity will be obtained, due to the multi-electron redox, that reported to occur in the discharge-charge process of POMs [4, 5]. Herein, KB was chosen as the conductive additive because it has higher electric conductivity and larger specific surface area than that of AB [6]. As was above

expected, much higher initial discharge capacity of  $421 \text{ mAh g}^{-1}$  was obtained by hand-grinding NAM with KB. The polarization in the charge process for NAM hand KB was further decreased in comparison with that of NAM hand AB and NAM ball-mill AB. However, a large irreversible charge capacity of  $77 \text{ mAh g}^{-1}$  was still obtained after the first cycle. As mentioned above, the mechanical ball-milling has shown effectiveness in improving the reversible capacity after the first charge for the system of NAM ball-mill AB. In order to reduce the irreversible charge capacity for NAM mixed with KB, the mechanical ball-milling NAM with KB was carried out. In comparison with NAM hand KB, the initial discharge capacity was improved to  $437 \text{ mAh g}^{-1}$ , and almost reversible charge capacity of  $429 \text{ mAh g}^{-1}$  was obtained after the first cycle for NAM ball-mill KB. It is noteworthy that all of the systems showed almost reversible discharge and charge capacities in the second cycle.

Figure 6.6b shows the cycle performance of NAM in various mixing systems after 50 cycles. The NAM hand AB showed steep capacity loss after the first cycle until the 10th cycle. Thereafter capacity faded continuously and discharge capacity of only  $49 \text{ mAh g}^{-1}$  was obtained after 50 cycles. On the other hand, NAM ball-mill AB showed higher discharge capacity than NAM hand AB, though the capacity continued decreasing gradually with cycling. After 50 cycles, capacity of  $132 \text{ mAh g}^{-1}$  was retained for NAM ball-mill AB. Similarly to NAM hand AB, NAM hand KB also showed notable capacity loss from the first cycle to the 6th cycle, but the capacity increased slightly with increase of cycle number to the 20th cycle, thereafter cycle performance tended to be stable. After 50 cycles, capacity of  $299 \text{ mAh g}^{-1}$  was

obtained for NAM hand KB. It should be noted that NAM ball-mill KB showed very stable cycle performance with long-term cycling, capacity of 399 mAh g<sup>-1</sup> corresponding to the capacity retention of 91.2% was obtained after 50 cycles.



**Figure 6.7** Nyquist plots of a) NAM mixed with AB by hand-grinding, b) NAM mixed with AB by ball-milling, c) NAM mixed with KB by hand-grinding and d) NAM mixed with KB by ball-milling recorded after 1 cycle and after 20 cycles.

To analyze the effect of the mechanical ball-milling and the type of conductive additive on the cycle performance of NAM, EIS measurements were carried out for the various mixing systems after 1 cycle and 20 cycles, the respective Nyquist plots are shown in Figure 6.7. It can be seen that all of the Nyquist plots consist of one semicircle in the high-frequency range and a linear part in the low-frequency range. Nevertheless, the lines in the spectra of NAM hand AB are almost vertical to the  $Z'$ -axis (Figure 6.7a), which correspond to the capacitive reactance instead of the solid-state diffusion of lithium ions (Warburg diffusion) in the cathode bulk material [7]. The vertical lines changed to the slope lines by mechanical ball-milling NAM with AB (Figure 6.7b), indicating that the capacitive effect was substituted for the diffusion of lithium ions in the cathode. Therefore, as illustrated in Figure 6.6a, the NAM hand AB showed the very large irreversible capacity in the first charge process, while the lower irreversible capacity was obtained for NAM ball-mill AB.

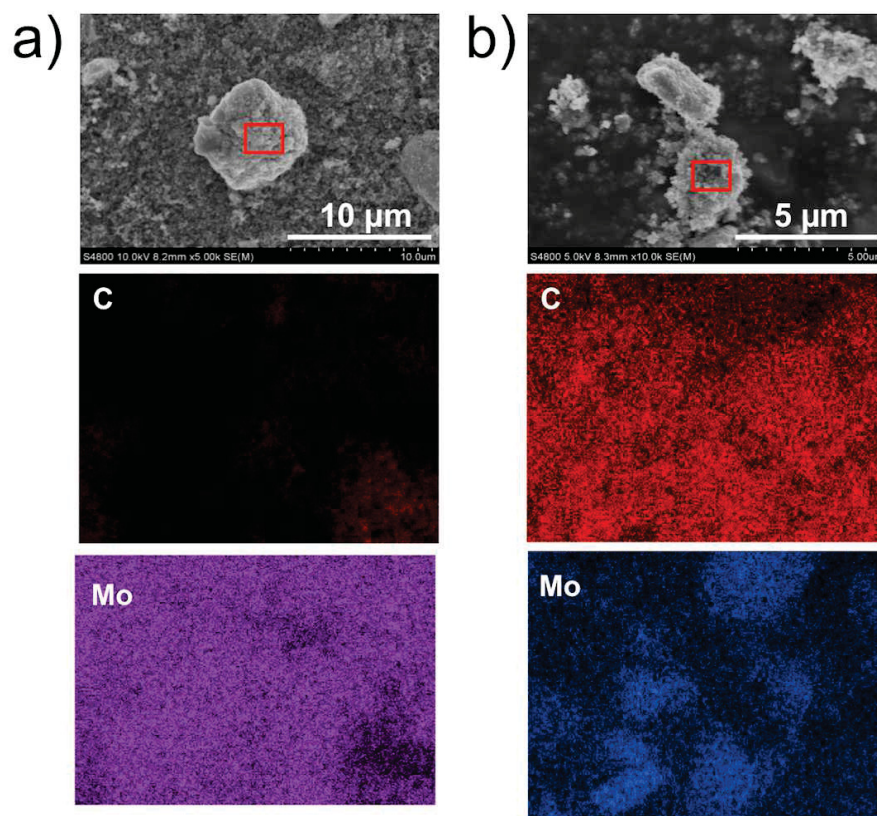


**Figure 6.8** SEM images and elemental distribution maps by EDS for a) NAM mixed with AB by hand-grinding and b) NAM mixed with AB by ball-milling (Red rectangles in the SEM images represent the selected areas for the EDS).

Figure 6.8a and b show the SEM images and the elemental distribution maps by EDS of NAM hand AB and NAM ball-mill AB, respectively. It can be seen that ground NAM particles and AB were mixed homogeneously in the cathode active material by ball-milling (Figure 6.8b), whereas micrometer size NAM blocks presented in NAM hand AB active material (Figure 6.8a). This result further indicates that the improved electrochemical property for NAM with ball-mill treatment should be ascribed to the higher contact surface area between conductive additives and NAM particles, which improved the electric conductivity, facilitating the lithium diffusion

in the electrode. This result is consistent with the reduced charge transfer resistance by the mechanical ball-milling (Figure 6.7).

Although the electric conductivity of NAM was improved by mechanical ball-milling NAM with AB, due to the intrinsic low electric conductivity of AB, there was still large resistance for the charge-transfer during the discharge-charge process. As illustrated in Figure 6.7b, after 20 cycles, the charge-transfer resistance of NAM ball-mill AB increased largely, which should be responsible for the gradual capacity loss with the increase of cycle number. On the other hand, by changing the conductive additive from AB to KB, NAM hand KB showed lower charge-transfer resistance (Figure 6.7c) than NAM ball-mill AB (Figure 6.7b), indicating that the electric conductivity of NAM could be further improved by mixing with KB conductive additive. Nevertheless, NAM hand KB also showed increase in the charge-transfer resistance after 20 cycles (Figure 6.7c), which should be caused by the inhomogenous mixing of NAM and KB by hand-grinding, as shown in Figure 6.8a. The charge-transfer resistance of NAM ball-mill KB hardly changed after 20 cycles (Figure 6.7d) compared to NAM hand KB (Figure 6.7c), indicating the electric conductivity of NAM was greatly improved by ball-milling NAM with KB. This would be the reason that NAM ball-mill KB not only showed the highest discharge capacity but also the most stable cycle performance with long-term cycling compared to the others systems.

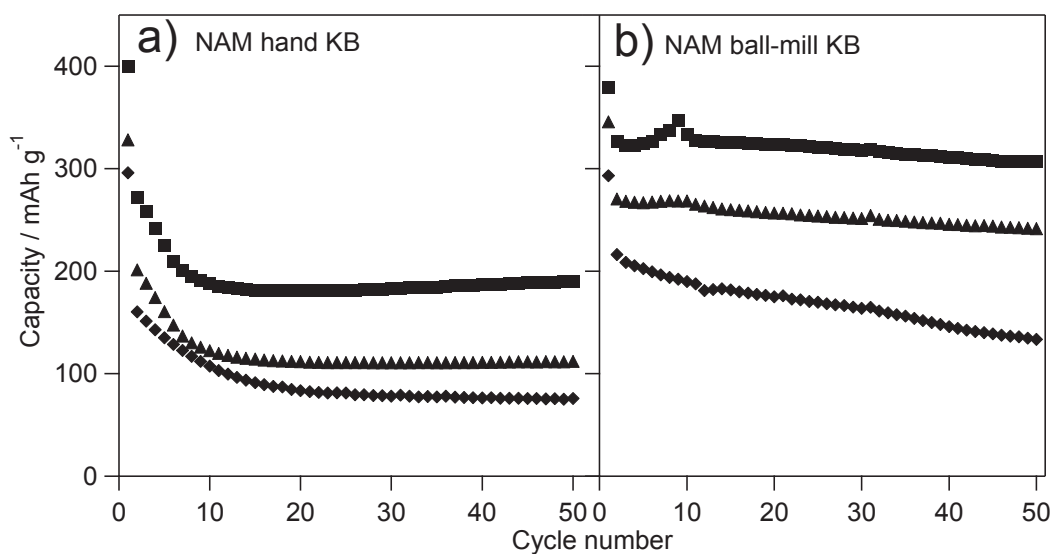


**Figure 6.9** Effect of the cathodes consisting of different weight ratios of NAM:KB:PTFE on the cycle performance of a) NAM mixed with KB by hand-grinding and b) NAM mixed with KB by ball-milling (■: NAM:KB:PTFE = 48:48:4; ▲: NAM:KB:PTFE = 64:32:4; ◆: NAM:KB:PTFE = 72:24:4).

The high carbon loading of the cathode decreases the energy density of the cell. The relationship between the loading KB weight, that effectively improved the electrochemical property of NAM, and the cycle performance of NAM was investigated. The cycle performance of the cathodes consisting different weight ratios of NAM:KB:PTFE by hand-grinding or ball-milling NAM with KB is shown in Figure 6.9. The discharge capacity of NAM decreased as the KB loading was decreased. However, in comparison with NAM hand KB, NAM ball-mill KB still showed relatively stable cycle performance after the first cycle and much higher discharge capacity was retained after 50 cycles. For NAM ball-mill KB, the system NAM:KB:PTFE = 64:32:4 showed similar cycle stability to NAM:KB:PTFE =

48:48:4 system and held about 240 mAh g<sup>-1</sup> after 50 cycles. For the system of NAM:KB:PTFE = 72:24:4, the capacity steeply decreased with the increase of cycle number and capacity faded to 134 mAh g<sup>-1</sup> after 50 cycles. This result indicates that low amount of the conductive additive was still insufficient to cover the surface of all NAM particles, leading to the low discharge capacity and poor cycle performance.

## 6.4 Discharge-Charge Reaction Mechanism

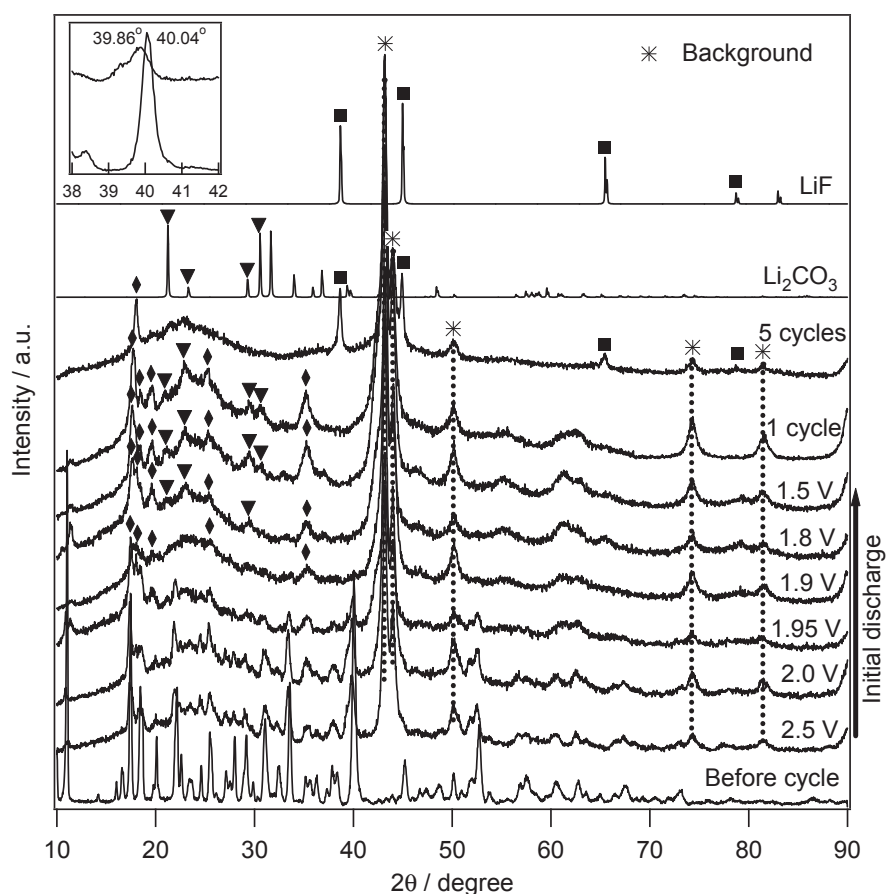


**Figure 6.10** *Ex situ* XRD patterns of NAM recorded at different voltages during the first discharge, after 1 cycle and after 5 cycles (peaks marked with \* at  $2\theta = 43.12^\circ, 43.96^\circ, 49.99^\circ, 74.2^\circ$  and  $81.44^\circ$  are the backgrounds originated from the metal substrate; ◆: reflections of NAM; ▼: reflections of  $\text{Li}_2\text{CO}_3$ ; ■: reflections of LiF).

In the investigation of POMs as the cathode materials of lithium battery, the reaction mechanism during discharge-charge process is very important, because POMs have intermediate property of the intercalation materials and molecular materials [4, 5], and its properties will depend on the reaction mechanism. To investigate the discharge-charge reaction mechanism, the change in the crystal structure of NAM during the electrochemical reaction was probed by the *ex situ* XRD measurements. Figure 6.10 shows the *ex situ* XRD patterns recorded at different voltages in the initial discharge process, after the first cycle and after 5 cycles. The XRD pattern of NAM before discharge was also plotted for comparison. It is clearly seen that the XRD pattern after discharging to 2.5 V was almost consistent with that of NAM before discharge, but the intensities of the reflections became weaker, and the positions of reflections shifted to the lower angle (as illustrated in the inset of Figure 6.10). This indicates that the crystal structure of NAM was maintained and its lattice expanded with the insertion of lithium ions. The XRD pattern did not show drastic changes when discharged to 2.0 V, indicating the crystal structure of NAM should be still maintained by the further insertion of lithium ions. Upon further discharging to 1.95 V, the reflections became much weaker and broader, and some reflections disappeared. Almost all of the reflections disappeared (except the several reflections marked with  $\blacklozenge$ ) when discharged to 1.9 V, indicating the crystal of NAM began to become amorphous. Upon further discharging from 1.8 V to the end of discharge at 1.5 V, the residual reflections of NAM did not change so much, but some new reflections (the positions marked with  $\blacktriangledown$ ) corresponding to the phase of  $\text{Li}_2\text{CO}_3$

appeared.  $\text{Li}_2\text{CO}_3$  should be arisen from the decomposition of electrolyte due to the deep discharge of NAM with the catalysis of POMs. In the following recharge process (after one cycle),  $\text{Li}_2\text{CO}_3$  was still included in the cathode, while other reflections of NAM except the marked residual peaks did not appear again, indicating that the crystal structure of NAM was irreversible during the first discharge-charge process. After 5 cycles, all of the reflections of NAM except the main peak around  $18^\circ$  disappeared, indicating that the crystal structure changed to amorphous, and the decomposed product ( $\text{Li}_2\text{CO}_3$ ) of electrolyte finally converted to LiF (reflections marked with ■).

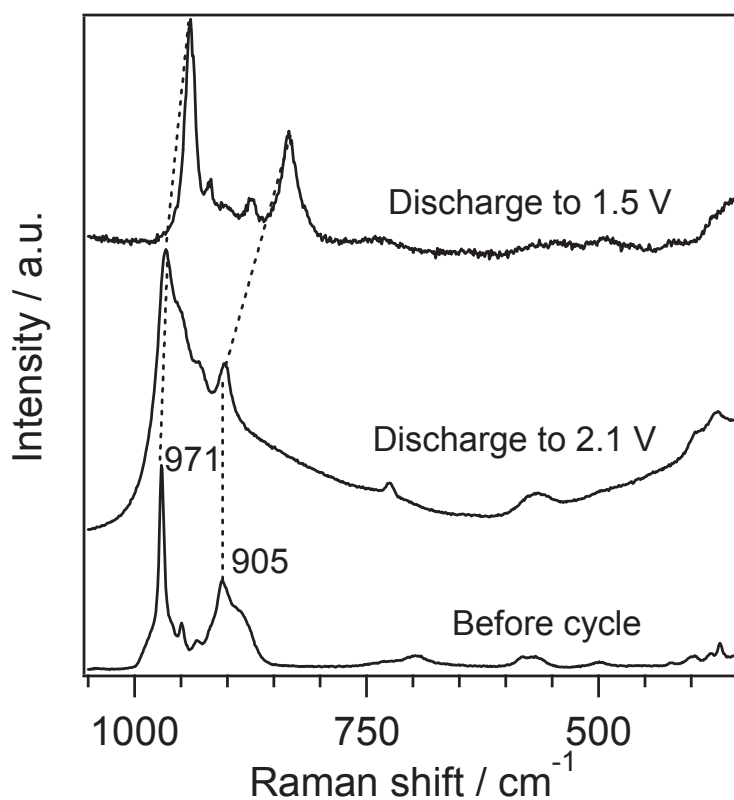


**Figure 6.11** *Ex situ* Raman spectra of NAM recorded at different voltages during the first discharge.

To confirm the structural stability of the molecular cluster ion  $[\text{AlMo}_6\text{O}_{24}\text{H}_6]^{3-}$  during the discharge-charge process, *ex situ* Raman spectra of NAM initially discharged to different voltages are plotted in Figure 6.11. For NAM sample before cycle, the peaks at  $971\text{ cm}^{-1}$  and  $905\text{ cm}^{-1}$  were obtained, those are assigned to the vibrations of Mo-O bonds [3, 8-10]. They shifted to lower wavenumbers with the insertion of lithium into the structure. The shift of Mo-O vibration to lower wavenumber corresponds to the decrease in electrostatic interaction with the reduction of molybdenum ion. The results of *ex situ* Raman spectra indicate that the structure of cluster ion unit  $[\text{AlMo}_6\text{O}_{24}\text{H}_6]^{3-}$  is stable during the discharge process, even though the crystal structure of NAM becomes amorphous irreversibly.

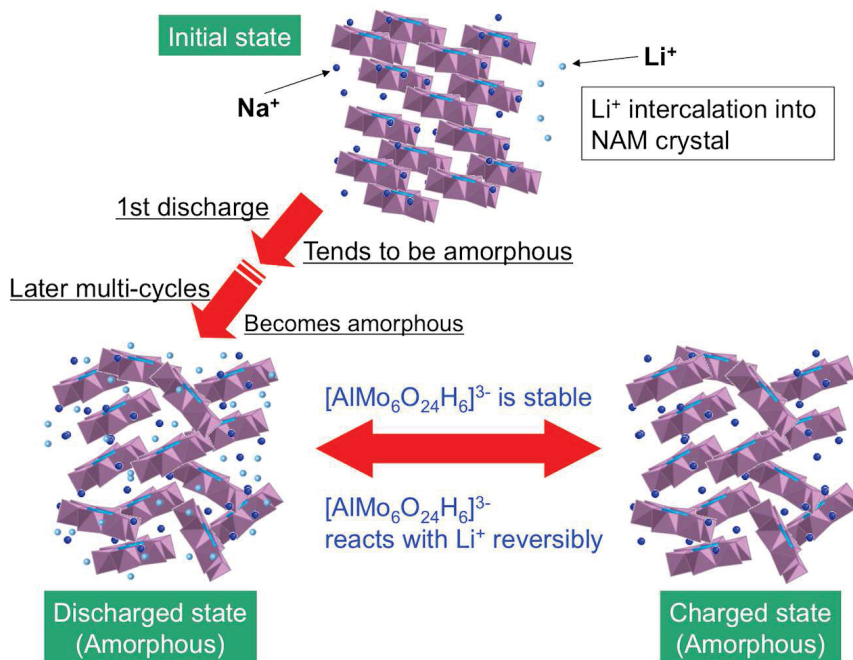


**Figure 6.12** The schematic image of reaction mechanism for NAM during the discharge-charge process.

On the basis of obtained data shown above, the schematic image of speculated discharge-charge mechanism for NAM is shown in Figure 6.12. As reported previously,  $(\text{KH})_9[\text{PV}_{14}\text{O}_{42}]$  (KPV) becomes amorphous after the first discharge and shows irreversibility of crystal structure change in the following charge process, but the molecular cluster ion unit  $[\text{PV}_{14}\text{O}_{42}]^{9-}$  is still stable and continues to react with lithium reversibly [5]. NAM also shows the similar crystal structure change during the discharge-charge process. NAM crystal begins to become amorphous gradually during the initial discharge process. However, the molecular cluster ion  $[\text{AlMo}_6\text{O}_{24}\text{H}_6]^{3-}$  is stable as was confirmed by the *ex situ* Raman spectra. In the following discharge-charge cycles, NAM changes to amorphous state completely, and the  $[\text{AlMo}_6\text{O}_{24}\text{H}_6]^{3-}$  reacts with lithium ion reversibly as molecular cluster ion. Different from the conventional lithium intercalation materials in which the amount of lithium usable for extraction-insertion mainly depends on the recoverability of crystal structure, the insertion-extraction of lithium in NAM can continuously proceed in the amorphous structure upon the discharge-charge cycling. The high reversible discharge-charge capacity and good cycle stability of NAM would be ascribed to the reversible reaction of stable cluster ion unit  $[\text{AlMo}_6\text{O}_{24}\text{H}_6]^{3-}$  with lithium ion in the deep discharge-charge process.

## 6.5 Conclusions

Anderson type polyoxomolybdate NAM showed very high capacity and stable cycle performance. Discharge capacity and cycle performance of NAM cathode

largely depended on the mixing method of active material with conductive additive and the type of conductive additive. The electrochemical properties of NAM were improved in the order of ball-milling with ketjen black (KB) conductive additive, hand-grinding with KB, and ball-milling with acetylene black (AB) conductive additive. NAM ball-milled with KB showed very high initial discharge capacity of 437 mAh g<sup>-1</sup> and the most stable cycle performance with high capacity retention of 91.2% after 50 cycles. The changes of crystal structure during the discharge-charge process were investigated by *ex situ* XRD measurements, and the structural stability of molecular cluster ion [AlMo<sub>6</sub>O<sub>24</sub>H<sub>6</sub>]<sup>3-</sup> was probed by *ex situ* Raman spectra. The results of *ex situ* XRD showed that the crystal structure of NAM was irreversible during the first discharge-charge process. The structure of NAM began to become amorphous in the first discharge and changed to amorphous state completely after 5 cycles. The results of *ex situ* Raman spectra showed the structure of molecular cluster ion [AlMo<sub>6</sub>O<sub>24</sub>H<sub>6</sub>]<sup>3-</sup> is stable during the discharge process. These data have demonstrated that the high discharge capacity and stable cycle performance of NAM originate in the improvement of the electric conductivity and the stable [AlMo<sub>6</sub>O<sub>24</sub>H<sub>6</sub>]<sup>3-</sup> molecular cluster ion that is independent from the recoverability of its crystal structure.

## References

- [1] S. Manikumari, V. Shivaiah, S. K. Das, *Inorg. Chem.*, 2002, 41, 6953–6955.
- [2] S. Uematsu, *Lithium Intercalation Into Polyoxometalates and Its Reaction Mechanism*, Master Thesis, 2012, Nagoya Institute of Technology.
- [3] S. Manikumari, V. Shivaiah, S. K. Das, *Inorg. Chem.*, 2002, 41, 6953–6955.
- [4] N. Sonoyama, Y. Suganuma, T. Kume, Z. Quan, *J. Power Sources*, 2011, 196, 6822–6827.
- [5] S. Uematsu, Z. Quan, Y. Suganuma, N. Sonoyama, *J. Power Sources*, 2012, 217, 13–20.
- [6] S. Kurodaa, N. Taboria, M. Sakurabab, Y. Sato, *J. Power Sources*, 2003, 119–121, 924–928.
- [7] J. Y. Song, H. H. Lee, Y. Y. Wang, C. C. Wan, *J. Power Sources*, 2002, 111, 255–267.
- [8] C. Martin, C. Lamonier, *Inorg. Chem.*, 2004, 43, 4336–4644.
- [9] V. Balraj, K. Vidyasagar, *Inorg. Chem.*, 1999, 38, 1394–1400.
- [10] R. Ratheesh, G. Suresh, V. U. Nayar, *J. Solid State Chem.*, 1995, 118, 341–356.

# Chapter 7

## Synthesis and Electrochemical Properties of Keggin Type

### Polyoxomolybdate $K_4[SiMo_{12}O_{40}]$

#### 7.1 Introduction

In this work, to improve the cycle performance of Keggin type POMs, silicon-centered polyoxomolybdate  $K_4[SiMo_{12}O_{40}]$  (KSM), which resembles to  $K_3[PMo_{12}O_{40}]$  (KPM) in the light of molecular structure and electronic structure, has been studied as the cathode material of lithium battery. The effect of annealing temperature on the electrochemical properties of KSM was investigated in detail.

#### 7.2 Experimental

##### 7.2.1 Synthesis of Materials

The synthetic method used to prepare KSM is similar to KPM [1]. However, it is found that the purification of KSM crystal was very difficult due to its high solubility in water. In this work, the following procedure was used to prepare the pure KSM crystal. 3 g of silicomolybdic acid  $H_4SiMo_{12}O_{40}$  (Nippon Inorganic Colour & Chemical Co., Ltd.) was dissolved in 20 ml distilled water and then, this solution was added to a saturated KCl (Kishida, GR) solution (15 ml distilled water containing 20 g KCl) with vigorously stirring for 10 min, the yellow precipitate KSM appeared

quickly. In order to purify KSM solid, the solution containing the yellow precipitate stood for 15 min, followed by decanting the supernatant solution slowly. Then, the remaining solid was dried at 60°C for several hours to remove water. The precipitation was washed with acetone to dissolve the yellow precipitate KSM, with the aim of filtering out the insoluble KCl solid. Subsequently, the yellow filter solution (total volume: 40 ml) volatilized to dryness at room temperature to yield the pure yellow KSM crystal. The synthesized KSM powder was annealed at 120, 200, 300, 400, 500 and 600°C for 6 h under air, respectively.

### **7.2.2 Characterization**

The crystal structure of KSM was indentified by X-ray diffraction (XRD) measurement using a powder X-ray diffractometer (Rigaku RAD-C) with Cu K $\alpha$  (40 kV, 40 mA) radiation. The diffraction data were collected for 3 s at each 0.03° step width from 10 to 90° in  $2\theta$ . The crystal structure parameters for the samples annealed at different temperatures were refined by Rietveld analysis using the RIETAN-2000 program [2, 3]. Thermal stability study of KSM was carried out by thermogravimetic analysis (TG) and differential thermal analysis (DTA) (Rigaku TG8101D). The TG/DTA experiment was performed at a heating rate of 10°C/min up to 700°C under air. Raman spectra were collected with a NRS-3300 (JASCO Corporation) in the wavenumber range 250–1150 cm<sup>-1</sup>, using a 532 nm laser as a probe light focused onto the surface of the samples with a  $\times 100$  objective microscope lens.

### 7.2.3 Electrochemical Measurements

The cathode electrode consisted of 30 wt.% active material, 65 wt.% acetylene black and 5 wt.% PTFE binder. The electrolyte solution was mixture of ethylene carbonate (EC) and diethyl carbonate (DEC) in a 3:7 (v/v) ratio with a supporting electrolyte of 1 M LiPF<sub>6</sub> (Kishida battery grade). The electrochemical properties of the cathodes were tested at 25°C by using CR-2032 coin cells with lithium metal as an anode. The discharge-charge characteristics of the cells were recorded on a battery tester (Interface model OZO-A19) in the potential range 2.0–3.5 V under a constant current of 0.05 mA. Solartron analytic instruments consists of a frequency-response analyzer (Solartron 1255) and a potentiostat (Solartron 1280) were used to acquire the cyclic voltammogram (CV) and electrochemical impedance spectroscopy (EIS). CV curves were recorded with scan rate of 0.05 mV s<sup>-1</sup>. The EIS spectra of the cells were recorded in the frequency range 10<sup>6</sup>–10<sup>-2</sup> Hz with an amplitude of 10 mV.

## 7.3 Results and Discussion

### 7.3.1 Crystal Structure

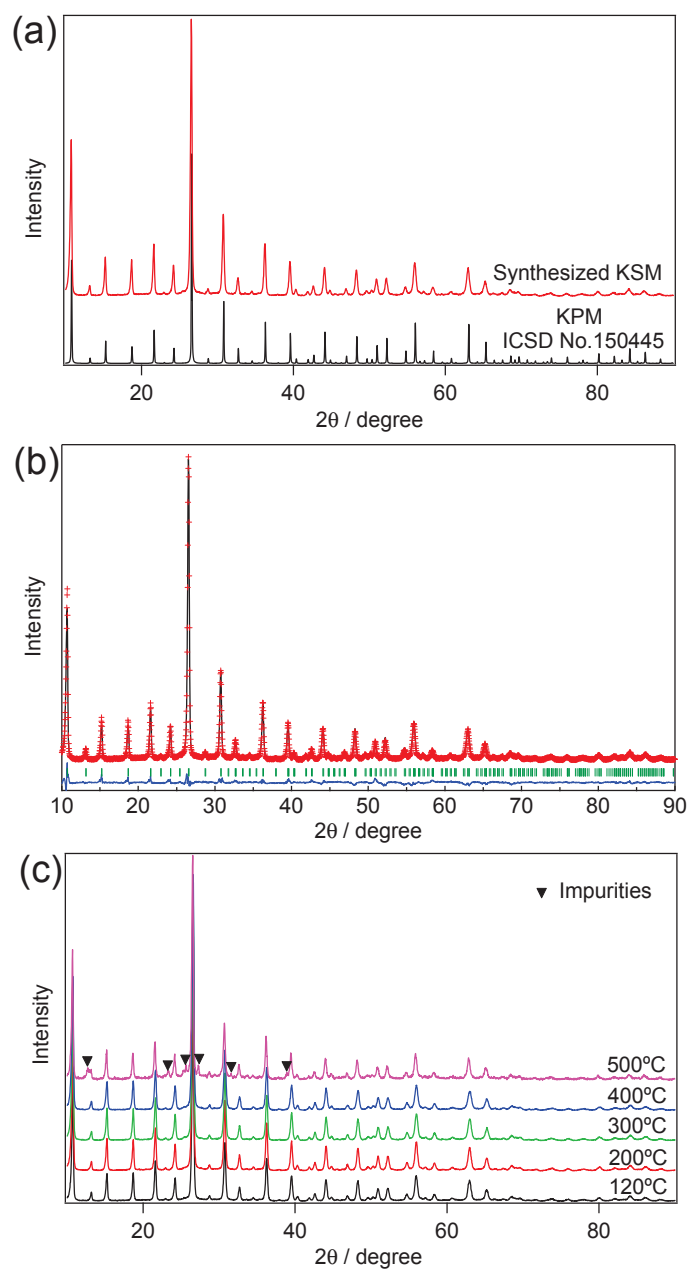


**Figure 7.1** (a) XRD pattern of the synthesized KSM, (b) Rietveld refinement patterns of the synthesized KSM (red: observed data; black: calculated Rietveld model; blue: difference line; green: the position of Bragg-reflection markers), (c) XRD patterns of KSM annealed at different temperatures.

Figure 7.1a shows the XRD pattern of synthesized KSM in this work. The reflections of as-prepared KSM match well with those of KPM, indicating that the synthesized KSM are pure phase in the cubic phase with the space group of  $Pn\bar{3}m$  [4]. The Rietveld refinement of the structure of KSM was carried out using the model of  $Pn\bar{3}m$  symmetry. The structure model is described as a cubic centered arrangement of discrete  $[\text{SiMo}_{12}\text{O}_{40}]^{4-}$  anionic species counterbalanced by  $\text{K}^+$  cations in octahedral sites. The result of the refinement is shown in Figure 7.1b and obtained parameters are summarized in Table 7.1. A fine refinement was obtained.

**Table 7.1** Rietveld refinement results for synthesized KSM.

Atom	Site	$g$	$x$	$y$	$z$
Mo	$24k$	1.0	0.46465	0.46465	0.26008
O(1)	$24k$	1.0	0.65538	0.65538	0.00158
O(2)	$24k$	1.0	0.05676	0.05676	0.76588
O(3)	$24k$	1.0	-0.87721	-0.87721	0.53441
O(4)	$8e$	1.0	0.32854	0.32854	0.32854
Si	$2a$	1.0	0.25000	0.25000	0.25000
K	$6d$	1.0	0.25000	0.75000	0.75000

Space group  $Pn\bar{3}m$ ,  $a=11.51180$  Å, unit cell volume  $1525.5613$  Å<sup>3</sup>,  $R_{\text{wp}} = 10.14$ ,  $R_p = 7.82$ ,  $R_R = 11.11$ ,  $R_e = 4.96$ ,  $S = 2.04$ .

### 7.3.2 Thermal Stability

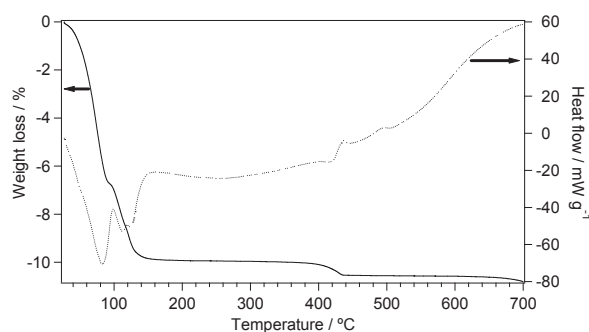


**Figure 7.2** TG-DTA curves of KSM.

The TG and DTA curves of KSM are shown in Figure 7.2. The endothermic peaks around 80°C and 120°C correspond to the loss of crystal water, leading to the anhydrous KSM compound [5]. There is no further weight change from 200 to 400°C. Thereafter two exothermic peaks are detected at 436 and 500°C, respectively. The results of thermogravimetric analysis are further confirmed by the XRD patterns of KSM annealed at different temperatures. As shown in Fig. 1c, there are no diffraction peaks of any impurity phases for the samples annealed below 400°C, while impurity phases are observed in the sample annealed at 500°C, which should be caused by the decomposition of KSM [5]. Furthermore, the color of KSM sample changes from yellow to white after annealing at 600°C, indicating the complete decomposition of KSM. This thermal behavior over 500°C is quite different from that of KPM. It is known that the thermal stability of Keggin type POMs is largely dependent on the center heteroion and the POMs containing phosphate ion are most stable [6]. Actually, a pure KPM phase was obtained even after annealing at 600°C [1].

### **7.3.3 Electrochemical Performance**

#### *(1) CV Curves*

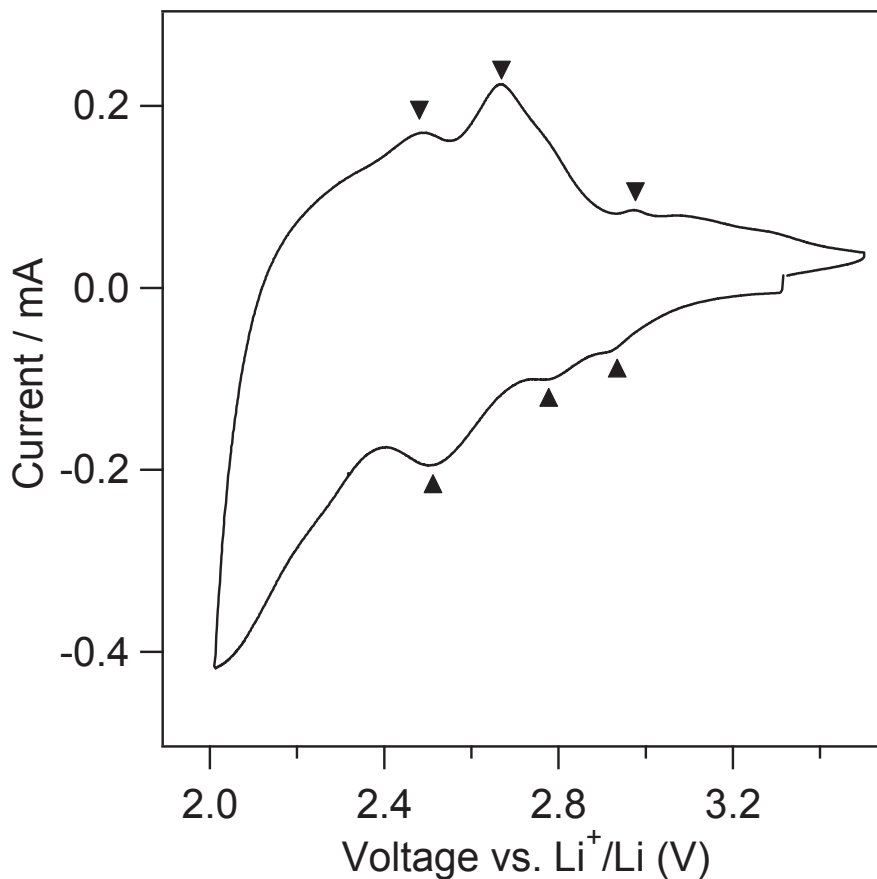


**Figure 7.3** CV curves of KSM at the scan rate of  $0.05 \text{ mV s}^{-1}$ .

The reversibility of oxidation-reduction for KSM was verified by CV measurement, as shown in Figure 7.3. KSM shows three anodic current peaks at 2.48, 2.67, 2.98 V and corresponding cathodic current peaks at 2.51, 2.79, 2.93 V, respectively. Although there are somewhat differences in the redox potential, the CV characteristic peaks of KSM are consistent with those of KPM reported previously [1], three pairs of redox peaks are also observed from KPM. This suggests the reversible multi-electron redox reactions are available for KSM as the high capacity cathode material like KPM [1].

## *(2) Discharge-Charge Performance*

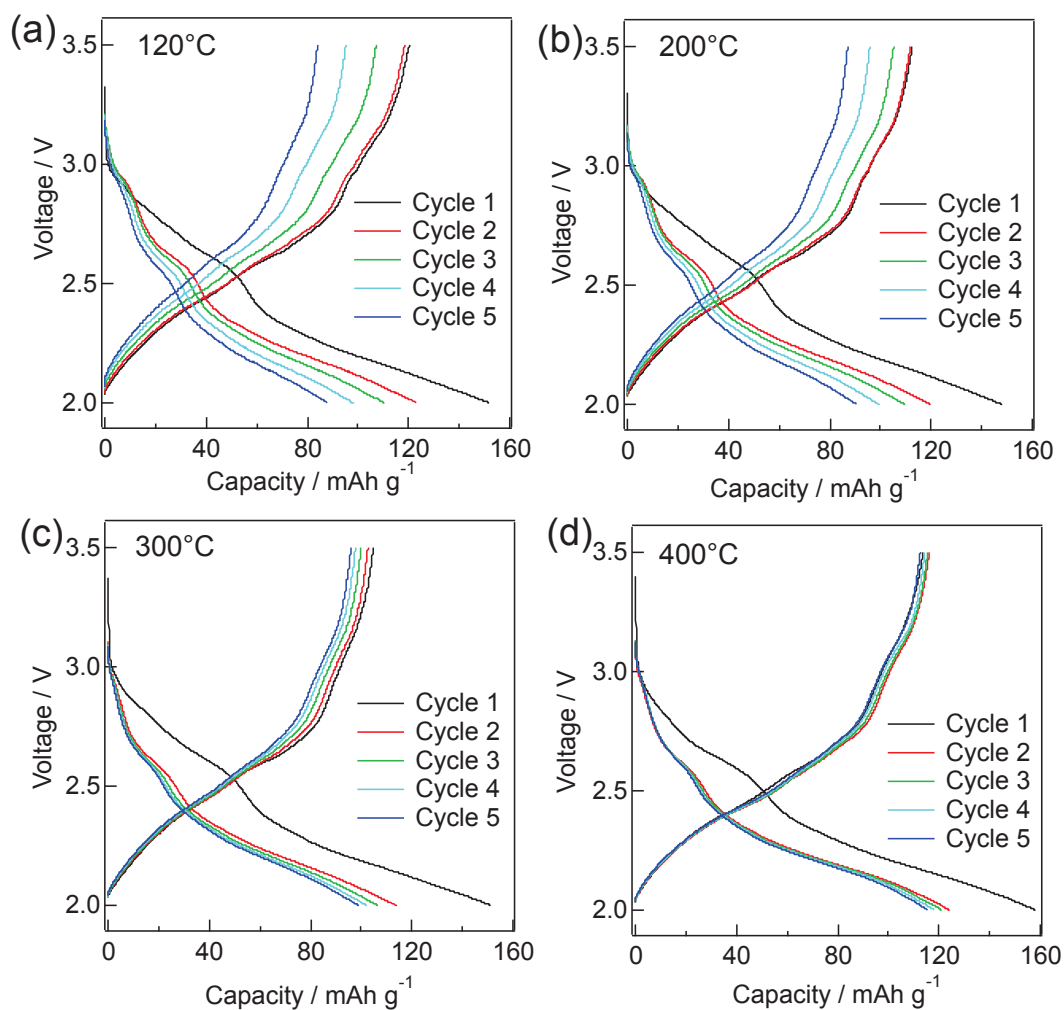


**Figure 7.4** The first five discharge-charge cycles of KSM annealed at (a) 120°C, (b) 200°C, (c) 300°C and (d) 400°C, respectively.

Figure 7.4 shows the discharge-charge curves in the voltage range of 3.5–2.0 V during the first five cycles for KSM annealed at 120, 200, 300 and 400°C, respectively. Three discharge plateaus were observed in the first discharge process for the annealed sample, those are consistent with the positions of the reduction peaks in the CV curves. Initial discharge capacity around 150 mAh g<sup>-1</sup> is obtained for the annealed sample, which is close to the theoretical capacity (163 mAh g<sup>-1</sup>) of KSM with single step reduction of Mo from VI to V state and is higher than the capacity of KPM (about

100 mAh g<sup>-1</sup>) in the same voltage range. In addition, the shape of the discharge curves for the annealed samples is almost the same even though there is an evident irreversible capacity in the second discharge process. It should be noted that all the samples show almost the same capacity loss (about 30 mAh g<sup>-1</sup>) after the first discharge. Herein, it is reasonable to believe that the capacity loss of KSM is not a result of the crystal structure change, because, as was confirmed previously, the crystal structure of KPM is well maintained after the first cycle, and the same behavior of capacity loss is exhibited as well.<sup>[1]</sup> We speculate that the capacity loss after the first cycle is probably attributed to a formation of solid electrolyte interface (SEI) via the decomposition of the electrolyte solution, that would be induced by a high catalytic activity of POM [7]. The formed SEI layer would disturb the decomposition of electrolyte solution. This would be the reason over discharge was not observed in the following cycles. As for the samples annealed at 200°C (Figure 7.4b), it shows the similar capacity retention in the first five cycles to the sample annealed at 120°C (Figure 7.4a). On the other hand, the capacity retention is improved significantly with the increase in the annealing temperature to 300 and 400°C (Figure 7.4c and d).

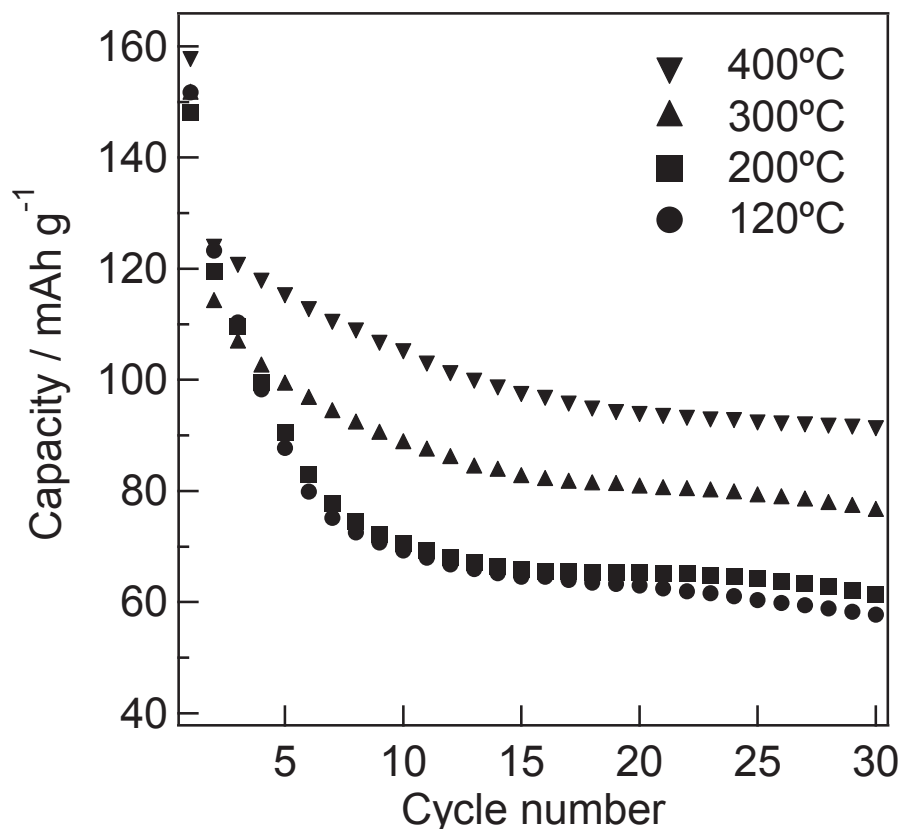


**Figure 7.5** Cycle performance of KSM annealed at different temperatures.

Cycling performance of KSM annealed at different temperatures is shown in Figure 7.5. As it can be seen that the capacity of the sample annealed at 200°C is only slightly higher than that of the sample annealed at 120°C, while significant improvement in the capacity retention is obtained after increasing the annealing temperature to 300 and 400°C. Capacity retention of 58% after 30 cycles is maintained for KSM annealed at 400°C, which is higher than those of the samples annealed at other temperatures. It is noted that the cycle performance of KSM is different from KPM. As for KPM annealed at 300 and 400°C, dramatic discharge capacity loss owing to the reduction of slight amount of Mo<sup>6+</sup> to Mo<sup>5+</sup> is observed [1]. After 30 cycles, capacity of only ~10 mAh g<sup>-1</sup> is obtained for KPM annealed at 300 and 400°C. Although the capacity of

KPM is improved by annealing at higher temperatures (500 and 600 °C), the cycle performance is still poor and capacity of less than 60 mAh g<sup>-1</sup> is obtained after 30 cycles. On the other hand, KSM after annealing treatment shows not only the higher discharge capacity but also the more stable cycle performance in comparison with that of KPM. After 30 cycles, KSM annealed at 300 and 400 °C shows capacities of 76 and 92 mAh g<sup>-1</sup>, respectively, which are much higher than that of KPM.

(3) EIS

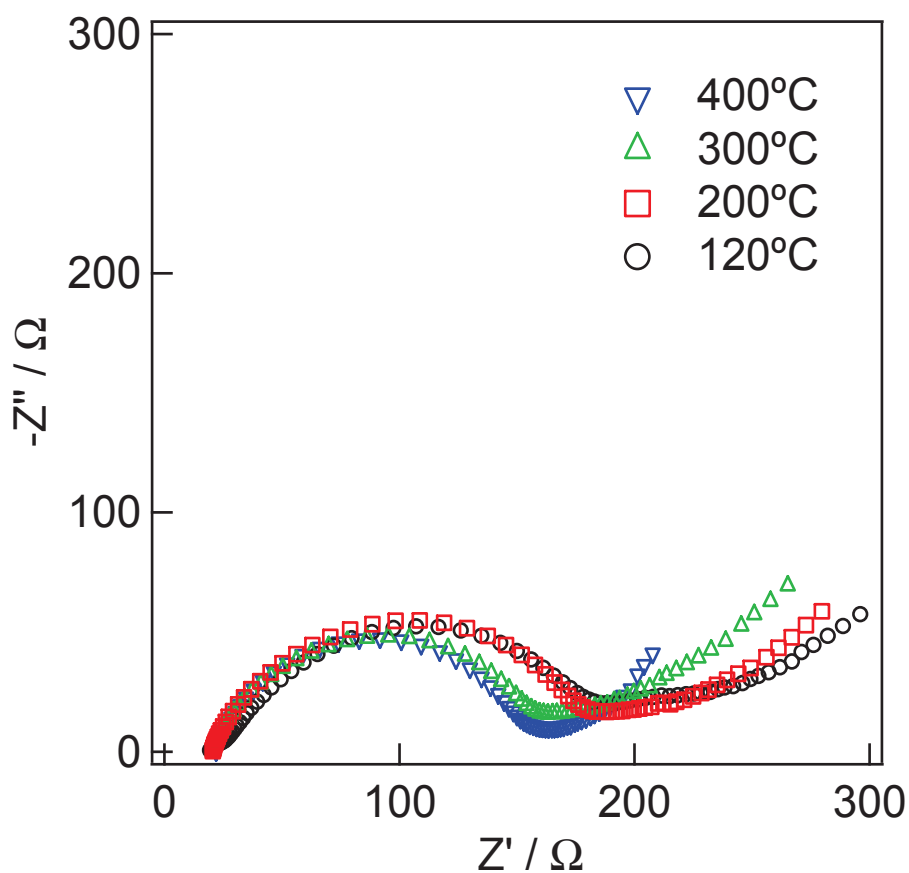


**Figure 7.6** The Nyquist plots of KSM annealed at different temperatures.

Figure 7.6 shows the EIS results of the cells after the 5th discharge. The Nyquist plots exhibit a single semicircle in the high frequency region, and a linear part

following at low frequency region. The semicircle is attributed to the resistance of the charge transfer process, while the linear part is due to the diffusion of lithium ions in the electrode. The diameter of the semicircle is equal to the charge transfer resistance ( $R_{ct}$ ). It can be confirmed that the  $R_{ct}$  decreases with the increase of annealing temperature. This low electric conductivity, which related to the high charge transfer resistance, in the samples annealed at lower temperature may be the one of the reasons for the low cycle stability.

### 7.3.4 Analysis for the Influence of Annealing Treatment on the Electrochemical Properties

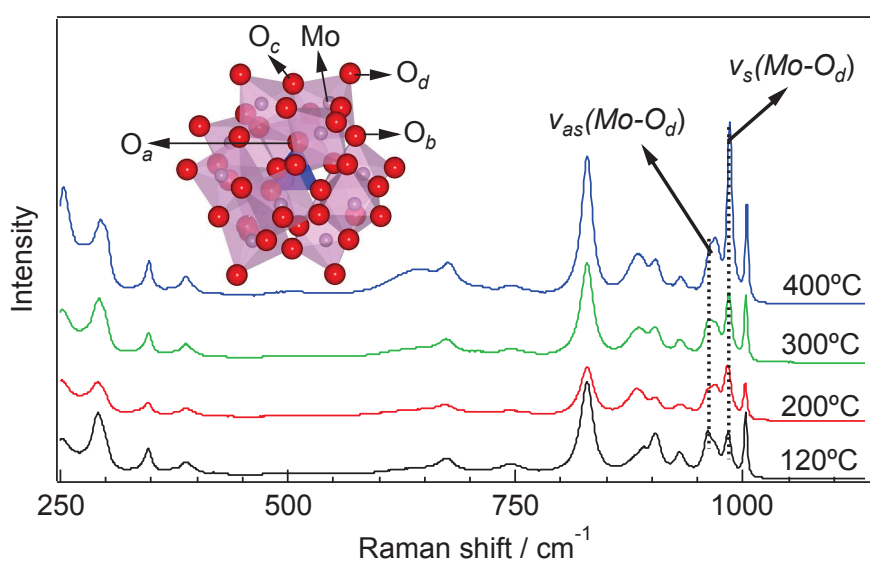


**Figure 7.7** Raman spectra of KSM annealed at different temperatures (inset: molecular structure of  $[\text{SiMo}_{12}\text{O}_{40}]^{4-}$ ).

Furthermore, in order to investigate the influence of annealing treatment on the molecular structure of cluster ion  $[\text{SiMo}_{12}\text{O}_{40}]^{4-}$  (redox active unit), the Raman spectra of the annealed samples were recorded, as shown in Figure 7.7. The inset of Figure

7.7 shows the polyhedral representation of the Keggin type cluster ion  $[\text{SiMo}_{12}\text{O}_{40}]^{4-}$  structure with one internal oxygen atom ( $\text{O}_a$ ) and three different external oxygen atoms ( $\text{O}_b$ ,  $\text{O}_c$ ,  $\text{O}_d$ ). The two peaks in spectra region of  $960\text{--}1000\text{ cm}^{-1}$  correspond to the asymmetric stretching of Mo- $\text{O}_d$  bond ( $\nu_{as}(\text{Mo-O}_d)$ ) and the symmetric stretching of Mo- $\text{O}_d$  bond ( $\nu_s(\text{Mo-O}_d)$ ), respectively [8]. The existence of anion-anion interaction in the form of electrostatic type is confirmed for the Keggin type POMs [8]. The anion-anion interaction arises from the electrostatic forces occurring between the external oxygen atoms ( $\text{O}_b$ ,  $\text{O}_c$ ,  $\text{O}_d$ ) of the adjacent anions. The electrostatic interaction of adjacent anions  $[\text{SiMo}_{12}\text{O}_{40}]^{4-}$  in the crystal structure will influence on the Raman stretching frequency of the Mo- $\text{O}_d$  bond. The stronger the electrostatic interaction will shift the stretching vibration of Mo- $\text{O}_d$  bond to higher wavenumber. Among Mo-O bonds, the Mo- $\text{O}_d$  bond stretching is considered to accept highest influence from the surrounding environment of  $[\text{SiMo}_{12}\text{O}_{40}]^{4-}$  ion, because  $\text{O}_d$  locates in outer site and is not shielded by anything. The symmetric stretching of Mo- $\text{O}_d$  bond shifts from  $982.5$  to  $986\text{ cm}^{-1}$  and the asymmetric stretching of Mo- $\text{O}_d$  bond shifts from  $961.5$  to  $970\text{ cm}^{-1}$  upon the increase of annealing temperature. This result suggests increase in the electrostatic interaction among  $[\text{SiMo}_{12}\text{O}_{40}]^{4-}$  anion. This means slight increase in valence number of Mo ion in  $[\text{SiMo}_{12}\text{O}_{40}]^{4-}$  with the increase in the annealing temperature with the re-oxidization of  $\text{Mo}^{5+}$  ion to  $\text{Mo}^{6+}$  ion.

**Table 7.2** The refined parameters of KSM annealed at different temperatures.

Temperature (°C)	$a$ (Å)	Unit cell volume (Å <sup>3</sup> )	Reliability factors
120	11.5119	1525.6011	$R_{wp} = 10.00$
			$R_p = 7.8$
			$R_R = 10.65$
			$R_e = 5.13$
			$S = 1.95$
200	11.5126	1525.8796	$R_{wp} = 9.85$
			$R_p = 7.73$
			$R_R = 10.54$
			$R_e = 4.90$
			$S = 2.01$
300	11.5144	1526.5951	$R_{wp} = 10.06$
			$R_p = 7.77$
			$R_R = 10.44$
			$R_e = 4.90$
			$S = 2.05$
400	11.5167	1527.5101	$R_{wp} = 9.75$
			$R_p = 7.48$
			$R_R = 10.11$
			$R_e = 4.91$
			$S = 1.98$

In order to confirm the slight change in valence number, the parameters of crystal structure for the samples annealed at different temperatures were refined by Rietveld analysis. The obtained lattice parameters are summarized in Table 7.2. It can be seen that the lattice parameter and unit cell volume expand with the increase in the annealing temperature. The lattice expansion of POMs by heat treatment was also reported by A. Kremenović et al [9] for the Keggin type dodecatungstophosphoric acid hexahydrate ( $H_3PW_{12}O_{40} \cdot 6H_2O$ ). For the case of KSM, the dependence of lattice size on the annealing temperature would be caused by re-oxidation of the partial reduced of  $Mo^{6+}$  in the initial state. In the previous paper [1], it has been reported that slight amount of  $Mo^{6+}$  reduction is occurring in the synthesis process of POM and this

harms the cycle stability of the Keggin type KPM. By increasing annealing temperature, reduced Mo ion is re-oxidized to Mo<sup>6+</sup>. The Mo<sup>6+</sup> in KSM can keep the cluster ion [SiMo<sub>12</sub>O<sub>40</sub>]<sup>4-</sup> in the  $\alpha$ -Keggin type structure. Contrary to the unstable  $\beta$ -Keggin type structure caused by the reduced Mo in the cluster ion, the  $\alpha$ -Keggin type structure is stable in the electrochemically reduced state. This would make the cluster ion [SiMo<sub>12</sub>O<sub>40</sub>]<sup>4-</sup> as redox unit reacts with lithium ion reversibly during the discharge-charge process, stabilizing the cycle performance of KSM. This result indicates that the cycle stability of Keggin type POMs would be improved by synthesizing them without reducing Mo<sup>6+</sup> ion.

#### 7.4. Conclusions

In this chapter, Keggin type silicon-centered polyoxomolybdate KSM was prepared. The increase of annealing treatment is beneficial to improve the discharge capacity and cycle stability. The improvement of electrochemical performance can be attributed to re-oxidization of Mo ion and stabilization of [SiMo<sub>12</sub>O<sub>40</sub>]<sup>4-</sup> unit. The annealed KSM as cathode material shows better cycle performance with comparison of the reported KPM. Hence, KSM as the cathode material with high capacity and stable cycle performance after annealing treatment is more attainable for rechargeable lithium battery with careful preparation without Mo<sup>6+</sup> ion reduction.

## References

- [1] N. Sonoyama, Y. Sugauma, T. Kume, Z. Quan, *J. Power Sources*, 2011, 196, 6822–6827.
- [2] Izumi, F., *The Rietveld Method*. Oxford University: Oxford, 1993.
- [3] F. Izumi, T. Ikeda, *Mater. Sci. Forum*, 2000, 198, 321–324.
- [4] J. C. A. Boeyens, G. J. McDougal, J. V. R. Smit, *J. Solid State Chemistry*, 1976, 18, 191–199.
- [5] G. A. Tsigdinos, *Ind. Eng. Chem. Prod. Res. Dev.*, 1974, 13, 267–274.
- [6] A. Aoshima, T. Yamaguchi, *Nippon Kagaku Kaishi*, 1985, 2237–2245.
- [7] M. T. Pope, Y. Jeannin, M. Fournier, *Heteropoly and Isopoly Oxometalates*, Springer-Verlag: Berlin Heidelberg New York Tokyo, 1983.
- [8] C. Rocchiccioli-Deltcheff, M. Fournier, R. Franck, R. Thouvenot, *Inorg. Chem.*, 1983, 22, 207–216.
- [9] A. Kremenović, A. Spasojević-de Biré, R. Dimitrijević, P. Sciau, U. B. Mioč, and P. Colomban, *Solid State Ionics*, 2000, 132, 39–53.

# Chapter 8

## Summary

This study has explored several promising polyoxometalates (POMs) as cathode materials of lithium battery. These POMs show much higher capacity than those of the conventional lithium intercalation materials. In Chapter 2, nanosize  $\text{K}_7[\text{NiV}_{13}\text{O}_{38}]$  (KNV) particles were prepared by a simple re-precipitation method, which show significant improvement in initial discharge capacity and capacity retention compared to the as-prepared microsize particles. In Chapter 3, to suppress the overcharge behavior at high voltage region ( $> 3.8 \text{ V vs Li}^+/\text{Li}$ ), which is caused by increased catalytic activity of nanosize POMs in electrolyte decomposition, the  $\text{K}_7[\text{MnV}_{13}\text{O}_{38}]$  (KMV) cathode consisting of the mixture of nanosize particles with microsize particles in the weight ratio of 1:1 as active material and ketjen black (KB) as conductive additive was fabricated. By using this electrode, the overcharge behavior was reduced and very stable cycle performance was obtained with high capacity retention over 97 % after 50 cycles. In Chapters 4 and 5, nanosize polyoxomolybdates  $(\text{NH}_4)_6[\text{NiMo}_9\text{O}_{32}]$  (ANM) and  $(\text{NH}_4)_6[\text{MnMo}_9\text{O}_{32}]$  (AMM) hand-ground with KB show high initial discharge capacity over  $470 \text{ mAh g}^{-1}$  at the current density of  $17 \text{ mA g}^{-1}$ . The POMs *in situ* re-precipitated in the micropores or mesopores of KB show improved discharge capacity at the high rates. In Chapter 6, the electrochemical properties of  $\text{Na}_3[\text{AlMo}_6\text{O}_{24}\text{H}_6]$  (NAM) were improved by ball-milling with acetylene black (AB) or KB conductive additive. NAM ball-milled with KB showed very high

initial discharge capacity of 437 mAh g<sup>-1</sup> and stable cycle performance with high capacity retention of 91.2% after 50 cycles. In Chapter 7, K<sub>4</sub>[SiMo<sub>12</sub>O<sub>40</sub>] (KSM) shows better electrochemical properties than that of the reported K<sub>3</sub>[PMo<sub>12</sub>O<sub>40</sub>] (KPM), which would be due to the re-oxidation of Mo<sup>5+</sup> ion in KSM reduced during the preparation process.

The discharge-charge process of almost of POMs continuously proceed in amorphous state, which is independent from the recoverability of the crystal structure, and the lithium ion can react reversibly with the stable molecular cluster ion.

**Table 8.1** Comparison of POMs with several cathode materials in available voltage, capacity, and energy density [1-3].

Cathode material	Average operating voltage (V)	Capacity (mAh g <sup>-1</sup> )	Energy density (mWh g <sup>-1</sup> )
Layered LiCoO <sub>2</sub>	4	140	560
Spinel LiMn <sub>2</sub> O <sub>4</sub>	4	120	480
Olivine LiFePO <sub>4</sub>	3.5	160	560
POMs	2.5	420	1050
Sulfur	2.1	600	1260

In Table 8.1, the comparison of POMs with several cathode materials in available voltage, capacity, and energy density was summarized. Although POMs shows lower voltage than those of the conventional lithium interaction materials, it can be compensated by its high capacity and its energy density is about two times of conventional materials. It is worthy to be noted that the energy density of POMs is

very close to the sulfur material, this means that POMs should be the very attractive cathode materials of next generation lithium battery for electric vehicles and temporary electric power storage system.

## References

- [1] A. Manthiram, *J. Phys. Chem. Lett.*, 2011, 2, 176–184.
- [2] K. E. Aifantis, S. A. Hackney, R.V. Kumar, *High Energy Density Lithium Batteries: Materials, Engineering, Applications*, Wiley-VCH: Federal Republic of Germany, 2010.
- [3] Y. Fu, A. Manthiram, *RSC Adv.*, 2012, 2, 5927–5929.

## List of Publications

1. Erfu Ni, Tomohiro Kume, Shinya Uematsu, Zhen Quan, Noriyuki Sonoyama. “Effect of annealing treatment on the electrochemical properties of polyoxomolybdate  $K_4[SiMo_{12}O_{40}]$  as cathode material of lithium battery”, *Electrochemistry*, 2014, 82, 14-18.
2. Erfu Ni, Shinya Uematsu, Zhen Quan, Noriyuki Sonoyama. “Improved electrochemical property of nanoparticle polyoxovanadate  $K_7NiV_{13}O_{38}$  as cathode material for lithium battery”, *Journal of Nanoparticle Research*, 2013, 15, 1732.
3. Zhen Quan, Erfu Ni, Shingo Hayashi, Noriyuki Sonoyama. “Structure and electrochemical properties of multiple metal oxide nanoparticles as cathodes of lithium batteries”, *Journal of Materials Chemistry A*, 2013, 1, 8848–8856.
4. Erfu Ni, Shinya Uematsu, Noriyuki Sonoyama. “Lithium intercalation into the polyoxovanadate  $K_7MnV_{13}O_{38}$  as cathode material of lithium ion battery”, *Solid State Ionics*, 2013, submitted
5. Erfu Ni, Shinya Uematsu, Noriyuki Sonoyama. “Intercalation reaction of lithium into the Anderson type polyoxomolybdate”, 2013, submitted
6. Zhen Quan, Erfu Ni, Yoshitaka Ogasawara, Noriyuki Sonoyama. “Electrochemical properties of nano size multiple metal oxides as anode electrode materials synthesized from layered

- double hydroxides”, 2013, submitted.
7. Zhen Quan, Erfu Ni, Yoshitaka Ogasawara, Noriyuki Sonoyama. “Nano size multiple metal oxide anode electrodes synthesized from layered double hydroxides – electrochemical reaction mechanism and surface morphology change during reaction with lithium ion”, 2013, submitted.
  8. Masaki Ikeda, Erfu Ni, Hiroshi Tanimura, Atsushi Hirano, Nobuyuki Imanishi, Yasuo Takeda, Osamu Yamamoto, Noriyuki Sonoyama. “Relationship between the structure and electrical property of various metal ion co-doped scandia stabilized zirconia”, 2013, submitted.
  9. Erfu Ni, Shinya Uematsu, Noriyuki Sonoyama. “Effects of conductive additive and particle size on the cycle performance of polyoxovanadate  $K_7MnV_{13}O_{38}$  as cathode material of lithium battery”, 2013, to be submitted
  10. Erfu Ni, Shinya Uematsu, Noriyuki Sonoyama. “Lithium intercalation into polyoxomolybdate  $(NH_4)_6[NiMo_9O_{32}]$  as cathode material of lithium battery” 2013, to be submitted.
  11. Erfu Ni, Syota Goto, Zhen Quan, Noriyuki Sonoyama. “Electrochemical property for the metal-doped vanadium bronze  $K_2V_8O_{21}$  as a cathode material of lithium battery”, 2013, to be submitted.

## **Acknowledgements**

The author would like to express his ultimate gratitude to supervisor, Associate Professor Noriyuki Sonoyama, Nagoya Institute of Technology, for earnest guidance, warmhearted encouragement and valuable discussions during doctoral course. The author is very grateful to Professor Nobuyuki Imanishi at Mie University for the SEM measurements. The author wishes to appreciate to all of former and present students in the same laboratory for their continuous encouragement and support.

Erfu Ni

January, 2014